DIPARTIMENTO DI FISICA
UNIVERSITÀ DEGLI STUDI DI FIRENZE
Facoltà di Scienze Matematiche, Fisiche e Naturali

DOTTORATO IN FISICA - XXI CICLO

Dissertation in Physics

TO OBTAIN THE DEGREE OF

Dottore di Ricerca
in Fisica

TITLE:

Dilution, finite size effects, and out-of-equilibrium dynamics in mean field models

PRESENTED BY

Antonia Ciani

Supervisor	PROF. DUCCIO FANELLI
Coordinator	PROF. ALESSANDRO CUCCOLI
Referees	DR. PAOLO POLITI
	DR. THIERRY DAUXOIS

Giugno 2009

SETTORE SCIENTIFICO-DISCIPLINARE:
Scienze Fisiche FIS/03

Contents

Introduction

The importance of long-range systems is known far back. Long range interactions play in fact a crucial role in many different fields including astrophysics [1, 2], plasma physics [3], hydrodynamics [4, 5], atomic [6] and nuclear [7] physics. Despite such a general interest, and the ubiquity of applications, long-range studies constitute a relatively new field of investigation. Fascinating phenomena, both associated to equilibrium and non-equilibrium dynamics, remain to be fully elucidated and point to the need for a comprehesive theoretical picture.

When long-range forces are at play, each constitutive unit is directly coupled to every other entity belonging to the system under scrutiny. This fact translates in an enhanced degree of complexity in the behaviour of long-range systems when compared to short range ones, where elements are solely sensitive to their immediate neighbourhood. Consequently, and because to the intrinsic difficulties in facing the study of long-range systems via the paradigm of traditional equilibrium thermodynamic, short-range problems have been preferentially analyzed. Moreover, for all fundamental interactions in nature, screening mechanism manifests, resulting in effective short-range smoothing, with exception of gravity. It is for this reasons that studies on long-range systems were initially bound to the specific domains of astrophysics and cosmology. The interest is nowadays revived thanks to novel laboratory experiments which enables one to resolve genuine long-range effects. Among others, we here quote the case of unscreened Coulomb interaction, vortices in two dimensional fluid mechanics, wave-particle system relevant to plasma physics and Free-Electron Lasers (FELs).

When aiming at developing a consistent interpretative framework, it is rather useful to resort to dedicated toy models, suitable for theoretical analysis. *Mean field* models are in particular very important. Despite their simplicity, they allow to capture key aspects of the intriguing long-range dynamics, and often return a sound, though effective description of the complex experimental realizations.

Following these lines of reasoning, and adopting a purely theoretical per-

spective, we have in this thesis chosen to first focus on a Ising like model, where the discrete spin evolves under mutual couplings. In particular we shall here inspect the role of an imposed dilution mechanism, acting on the network of underlying of connections. Introducing a dilution like effect has several implications. Dilution represents in fact an interesting concept, recently being re-discovered in the rapidly expanding field of network theory [8]. We shall be mainly concerned, with discussing the modification on the equilibrium solution, following the introduction of dilution. Finite size effects will prove fundamental, as revealed by our quantitative analysis.

The peculiar character of long-range system is also appreciated, when focusing on the out-of-equilibrium dynamics. For short-range systems, after a short transient, the system converges (typically in an exponential fashion) to the deputed thermal equilibrium. At odd with this vision, interesting and unexpected dynamical behaviours can develop, when considering long-range couplings. Simulations in the microcanonical ensemble can for instance reveal that the system is not ergodic, implying that only a limited portion of the accessible phase space is visited during the dynamical evolution. More importantly, when starting far from equilibrium, after a early fast evolution (that is called "violent relaxation"), long-range systems typically get trapped in the so-called Quasi Stationary States (QSSs). These are intermediate regimes which persist for a long-time before the system finds its way to equilibrium.
The QSS lifetime actually diverges with the number of degree of freedom (i.e. the number of particles composing the system). In this respect, QSSs assume a particular important conceptual role. They might in fact represent the only experimentally accessible configuration for all those applications where a large ensemble made of interacting particles is driving the dynamics.

QSSs are for instance found within the celebrated Hamiltonian Mean Field (HMF) model, often referred to as the paradigmatic example for out-of-equilibrium studies on long-range interacting systems. The HMF model and the emergence of QSSs are the second topic covered in this Thesis.
In the course of time several attempts have been made aiming at providing a systematic theoretical description of QSSs. The most successfull attempt elaborates on the pioneering work of Lynden-Bell [9] and is based on the fact that in the continuum limit (infinite number of particles) the discrete set of equations stemming from the original N-body Hamiltonian, converges to a Vlasov equation. The Lynden Bell theory is however an approximate, statistical based, approach. Alternatively one could resort to a dynamical description, which should however originates from the relevant Vlasov setting. In this Thesis we will analyse the out-of-equilibrium HMF properties within the associated Vlasov picture, by fully exploiting the Hamiltonian formalism to derive closed analytical expressions for the main macroscopic observables. This technique here termed the Bracket Method is particularly targeted to short time analysis.

Finally, as a third point and to close up the picture, we will finally elaborate on the out-of-equilibrium effects of dilution. Also for this latter application, we will operate with reference to the HMF model, testing the robustness of the QSSs with respect to the dilution amount.

The outline of the Thesis is the following:

1. Chapter 1 is devoted to summarizing the main features of long-range systems. We discuss the anomalies relative to the thermodynamical behaviour, emphasising the crucial aspects related to the lack of additivity. We then recall the ensemble inequivalence concept, focusing on specific applications. We also elaborate on the dynamical behaviour of long-range systems, discussing in particular the puzzle of QSSs' emergence.

2. The second chapter presents a detailed analysis of an Ising like model, of the mean filed type, in presence of a diluted network of couplings. The latter converges to the Curie-Weiss model in the fully coupled limit. We explore in particular the modification on the equilibrium solution and investigate the finite size corrections to the equilibrium magnetization. This is achieved by performing two independent calculations that are subsequently benchmarked to direct simulations. The first procedure is based on the replica trick approximation, while the second develops on the cavity method.

3. In the third chapter we turn to analyze the HMF model, and start by reviewing the current literature entries on the subject. We briefly recall the equilibrium thermodynamic solution, and then rapidly introduce the concept of QSS. We recap on the Lynden Bell theory and comment on how it enables us to predict, with a good accuracy, the relevant macroscopic observables associated to the QSSs and corresponding out-of-equilibrium transition. Finally, we summarize the available results on the time duration of the QSSs. This is a complex, apparently controversial, issue that we try to clarify by providing novel numerical insight.

4. In Chapter 4 we analyse the HMF model, in its continuum limit, i.e. within the Vlasov scenario. We shall adopt a Hamiltonian formalism to derive an analytical expression for the global magnetization of the system as a function of time. We here analyse both the HMF violent relaxation process and the subsequent QSS regime focusing in particular with high and low energy dynamical regimes. We also analytically characterize the out-of-equilibrium phase transition separating homogeneous and non-homogeneous QSSs, testing our results versus direct simulations.

5. In the last chapter we will continue elaborating on the effects of a dilution, which is now assumed to alter the ideal, fully coupled HMF model. Are QSS robust versus the imposed dilution? This question is here answered

via dedicated simulations, also aimed at clarifying the associated QSS duration.

Chapter 1

Dynamics and thermodynamics of systems with long-range interactions

To provide an operative definition of long-range interactions we shall consider the two-body potential $V(r)$:

$$V(r) = \frac{C}{r^\alpha}, \tag{1.1}$$

where r is the modulus of the inter-particle distance. An approximate evaluation of the energy U of a particle positioned in the center of a sphere of radius R in a d-dimensional space (see Fig. 1.1) reads

$$\begin{aligned} U &= \int_\varepsilon^R \rho \left[\frac{1}{r^\alpha}\right] 4\pi r^{d-1} dr = \\ &= 4\pi\rho \int_\varepsilon^R r^{(d-1)-\alpha} dr \propto \begin{cases} \left[r^{d-\alpha}\right]_\varepsilon^R \sim R^{d-\alpha} & \text{if } d-\alpha \neq 0 \\ \left[\ln r\right]_\varepsilon^R \sim \ln R & \text{if } d-\alpha = 0 \end{cases}, \end{aligned}$$

where we evidence the dipendence on R and we neglect the contribution of a small ball of radius ε around the particle[1]. It is hence clear that the energy diverges with R if the exponent α is smaller than the embedding dimension d, namely the dimension of the physical space where the interaction occurs. Inspired by this peculiar observation and following the customary paradigms [10] we will define an interaction to be long-range if $\alpha \leq d$ ($\alpha \leq 3$ in the Euclidean space).

Remarkably, and according to the above definition, the surface contribution to the energy cannot be neglected when long-range couplings are at play. Each

[1] This requirement provides an effective smoothing of the potential by eliminating problems that arise due to the singular behaviour of the interaction at short distances.

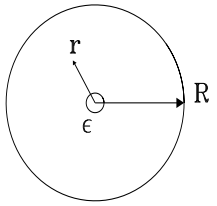

Figure 1.1: The energy in a $3D$ sphere of radius R diverges as $R^{3-\alpha}$ if the interaction is long-range, i.e. $\alpha \leq 3$.

particle is hence influenced by all other constituents, not just local neighbours, as it happens for short-range interactions.

When aiming at charaterizing the main properties of long-range systems, one can make reference to two distinct interpretative levels: The first has to do with the associated properties of equilibrium, while the second deals with non-equilibrium features. As we shall be addressing in the following, inequivalence of statistical *ensemble* is being reported, an observation which motivates the search for a consistent thermodynamics description. On the other hand, the emergence of Quasi Stationary States (QSSs) points to the need of elaborating a compherensive dynamical framework stemming from the principles of kinetic theory. Investigating the physics of systems subject to interactions decaying with distance and that can show singularities at short ranges proves difficult despite progresses has been recently reported along these lines. For these reasons it is customary to resort to the so called *mean-field approximation* ($\alpha = 0$) which turns out to be analitically tractable both in canonical and microcanonical ensemble. These systems will be object of our analysis.

In this chapter we shall briefly review some of the phenomena that characterize long-range interactions, with reference to both toy-models and real physical systems.

1.1 The lack of additivity

When attempting a statistical mechanics treatment of systems with long-range couplings, one faces the problem of lack of *additivity*, which can be exemplified as follows. Imagine to partition a given system into subsystems. Then, the total energy of the system does not correspond to the sum of the energies associated to each subsystems.

Let us turn to illustrate this concept, with reference to a simple mean-field

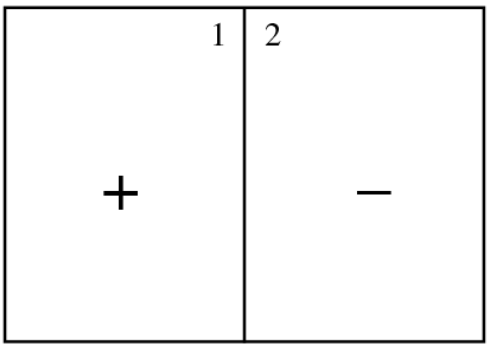

Figure 1.2: A microscopic configuration with total zero magnetization, illustrating the lack of additivity in the mean-field model (1.2).

Hamiltonian:

$$H = -\frac{J}{N}\left(\sum_i S_i\right)^2, \tag{1.2}$$

where the spins $S_i = \pm 1$, $i = 1, ..., N$, are all coupled. This is the celebrated Curie-Weiss model which we shall be deeply analysing in the forthcoming chapter. Notice that the rescaling prefactor $1/N$ ensures the extensivity of this Hamiltonian [11], since $H \propto N$. On the contrary, while being extensive, Hamiltonian (1.2) is not additive. To shed light onto this point, we divide the system into two equal parts, as schematically pictured in Fig. 1.2. Consider first the particular case when all spins in the left box are equal to 1, while all spins in the right portion are equal to -1. It is clear that the energy of the two different parts is the same, and reads $E_1 = E_2 = -\frac{J}{N}\left(\frac{N}{2}\right)^2 = -\frac{JN}{4}$. At variance, the energy of the whole system is $E = -\frac{J}{N}\left(\frac{N}{2} - \frac{N}{2}\right)^2 = 0$. Hence, the energy of such a system is not additive, since $E \neq E_1 + E_2$.

The fact that the system is non additive has strong consequences in the construction of the canonical *ensemble*, i.e. following the usual derivation which moves from the microcanonical *ensemble*. Consider a situation as depicted in Fig. 1.2, and imagine that system 1 is much smaller than system 2. The probability that system 1 carries an energy which falls within the interval $[E_1, E_1 + dE_1]$, given the system 2 has an energy E_2 (the conservation of total energy imposes that $E = E_1 + E_2$), is proportional to $\Omega(E_1)\Omega(E_2)dE_1$, where $\Omega(E)$ is the number of states of a system with a given energy E. $\Omega(E)$ is related to the entropy via the classical Boltzmann formula $S(E) = k_B \ln \Omega(E)$, where k_B stands for the Boltzmann constant. By invoking the additivity of the energy and considering that E_1 is much smaller than E, one can expand the term $S_2(E - E_1)$, thus yielding:

$$\begin{aligned}\Omega(E_1)\Omega(E_2)dE_1 &= \Omega(E_1)\Omega(E-E_1)dE_1 \\ &= \Omega(E_1)\exp[S_2(E-E_1)]dE_1 \\ &= \Omega(E_1)\exp[S_2(E) - E_1\frac{\partial S_2}{\partial E_2}|_E + ...]dE_1 \\ &\propto \Omega(E_1)\exp[-\beta E_1]dE_1,\end{aligned} \tag{1.3}$$

where $\beta = \frac{\partial S_2}{\partial E_2}|_E$. As an end result one obtains the usual canonical distribution. As it should be clear from the above, additivity is a crucial ingredient in the derivation, which in turn suggests that non additive systems may have peculiar behaviours, when placed in contact with a thermal reservoir. The next sections are devoted to presenting a selection of important, both dynamical and equilibrium features which are ultimately related to the long-range nature of the interaction and the associated lack of additivity.
We shall first focus on the equilibrium properties, to which the next section is entirely devoted. Then we will concentrate on dynamical aspects, so introducing the main topic addressed in this thesis work.

1.2 Equilibrium anomalies: Ensembles inequivalences, negative specific heat and temperature jumps

The lack of additivity is indirectly responsible for many unusual properties which have been detected for systems with long-range interactions [10]. Among the most striking equilibrium anomalies it is worth including the inequivalence of statistical *ensembles*, negative specific heat in the microcanonical *ensemble* and possible temperature discontinuities at first order transitions.

In the following, we elaborate on these concepts, by referring to specific examples [12].

Consider yet another spin model with infinite range, mean-field like interactions. The model is defined on a lattice, where each lattice point i is occupied by a spin-1 variable $S_i = 0, \pm 1$. The Hamiltonian is given by:

$$H = \Delta \sum_{i=1}^{N} S_i^2 - \frac{J}{2N}\left(\sum_{i=1} S_i\right)^2 \tag{1.4}$$

where $J > 0$ is a ferromagnetic coupling constant and Δ controls the energy difference between the magnetic ($S_i = \pm 1$) and the non-magnetic ($S_i = 0$) states. We set $J = 1$. This is a simpler version of the Blume-Emery-Griffiths (BEG) model [13], also known as the Blume-Capel model. As we will discuss later, the model phase diagram can be determined analytically, both within the canonical and the microcanonical *ensembles*, so allowing to shed light onto the inequivalence issue.

A global parameter to monitor the evolution of the model is the average magnetization m, given by:

$$m = \frac{1}{N}\sum_i S_i \quad . \tag{1.5}$$

The canonical equilibrium state can be obtained by maximizing the rescaled free energy (see details in [13])

$$\phi(\beta) = -\frac{1}{\beta}\lim_{N\to\infty}\frac{\ln Z}{N} \tag{1.6}$$

where Z is the partition function

$$Z = \sum_{S_i}\exp[-\beta H], \tag{1.7}$$

and $\beta = 1/k_B T$, T labelling the temperature of the system. k_B stands for the Boltzmann constant.

In general working in the microcanonical *ensemble* can prove rather cumbersome. However, with reference to this specific case study, the derivation of the equilibrium state in the microcanonical *ensemble* reduces to a simple counting problem [14]. This is due to the fact that all the spins interact with equal strength, irrespectively of their mutual distance. A given macroscopic configuration is characterized by the quantities N_+, N_-, N_0 respectively identifying up, down and zero spins. Cleary, the constraint $N_+ + N_- + N_0 = N$ applies. The energy E of such a configuration is solely function of N_+, N_- and N_0 and reads

$$E = \triangle Q - \frac{1}{2N}M^2, \tag{1.8}$$

where $Q = \sum_{i=1}^N S_i^2 = N_+ + N_-$ (the so called quadrupole moment) and $M = \sum_{i=1}^N S_i = N_+ - N_-$ (the magnetization amount) plays the role of the order parameters. The number of microscopic configurations Ω compatible with the macroscopic occupation numbers N_+, N_- and N_0 is

$$\Omega = \frac{N!}{N_+!N_-!N_0!}. \tag{1.9}$$

Using Stirling's approximation in the large N limit, the entropy, $S = \ln\Omega$ can be cast in the explicit form:

$$S = -N\Big[(1-q)\ln(1-q)+\frac{1}{2}(q+m)\ln(q+m)+\frac{1}{2}(q-m)\ln(q-m)-q\ln 2\Big] \tag{1.10}$$

where $q = Q/N$ and $m = M/N$ are the quadrupole moment and the magnetization per site, respectively.

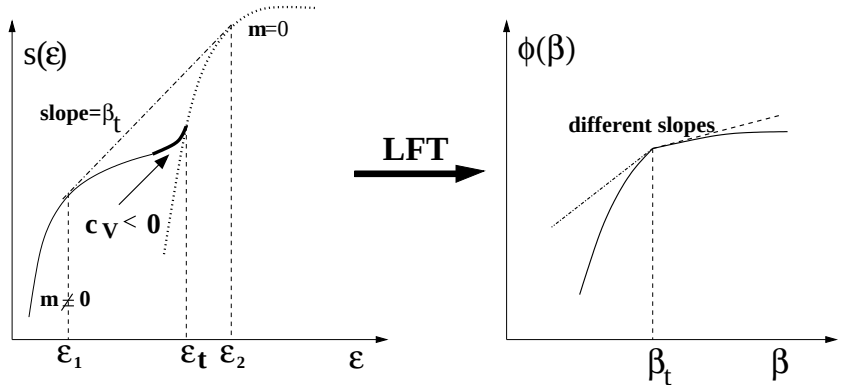

Figure 1.3: s(ϵ) as a function of energy density ϵ for the BEG model is plotted. Here the negative specific heat coexists with a temperature jump, the dash-dotted line is the concave envelope and the region with negative specific heat $c_V < 0$ is explicitily indicated. On the right the rescaled free energy is represented. The first order phase transition is located in β_t. The figure is taken from Ref. [12].

We are hence in a position to compare the predictions in the microcanonical and canonical *ensembles*, and identify possible traces of inequivalence. In doing so we shall mainly refer to the discussion in [12].

We shall elaborate on this important phenomenon in the remaining part of this section. In doing so we build on the specific BEG model, while at the same time identifying the general, reference concepts. In particular, we will show, for this specific example, that the inequivalence of ensemble is associated to the existence of a convex region of the microcanonical entropy as a function of the energy. This latter conclusion holds in general for long range interacting systems.

In Fig 1.3 a schematic rapresentation of the entropy and the rescaled free energy (defined in Eq. (1.6)) is depicted, being these observables related by a Legendre-Fenchel Transform (LFT):

$$\phi(\beta, n) = \inf_{\epsilon}[\beta\epsilon - s(\epsilon, n)]. \tag{1.11}$$

The entropy curve consists of two branches: the high energy branch is obtained for $m = 0$ (dotted line), while the low energy one refers to $m \neq 0$ (full line). The two branches merge at energy value ϵ_t where the left and right derivatives do not coincide; hence microcanonical temperature ($T(e) = \left(\frac{\partial s(e)}{\partial e}\right)^{-1}$) is different on the two sides, yielding to a *temperature jump* (this is better shown in Fig. 1.5 as we will discuss later). In the low energy branch, a region where entropy is locally convex (thick line) arises, that corresponds to *negative specific heat*, according to the formula $\frac{\partial^2 S}{\partial E^2} = -\frac{1}{C_v T^2}$. In the same figure, the rescaled free energy $\phi(\beta)$ is plotted. $\phi(\beta)$ is a concave function and for this reason in the canonical ensamble the specific heat is always positive. This is in turn the

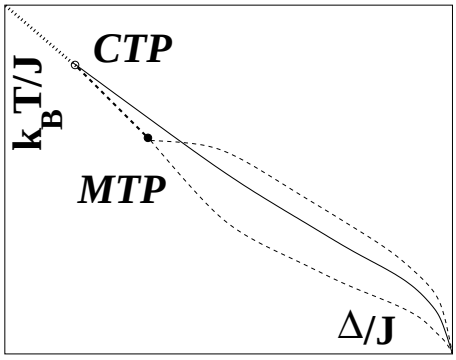

Figure 1.4: Schematic representation of the phase diagram, expanded around the canonical (CTP) and microcanonical (MTP) tricritical points. The dotted line refers to the common second order curve, while the solid line represents the canonical first order curve. The dashed lines correspond to the microcanonical *ensemble* (the bold one represents a continuous transition). Figure is taken from Ref. [12].

first stringent evidence that the two ensembles here considered, namely the micronanical and the canonical ones, are inequivalent.

The inequivalence is also appreciated when considering the inverse LFT transform, which enables us to recover the microcanonical entropy from the rescaled free energy $\phi(\beta)$. Mathematically in fact:

$$s(e,n) = \inf_{\beta}[\beta\epsilon - \phi(\beta,n)]. \tag{1.12}$$

Since the invesre LFT of a function is always concave one cannot recover the initial microcanonical entropy, which displays a "convex intruder". Indeed, one gets the concave envelope of the entropy function as reported in in left side of Fig. 1.3, with the dashed-dotted line.

Moreover we note that, in β_t, left and right derivatives of $\phi(\beta)$ (given by ϵ_1 and ϵ_2 respectively) are different. This is the first order phase transition point in the canonical *ensemble*. The BEG model displays, indeed, phase transitions, both of first and second order, but the transition curves in the phase diagram obtained within the two *ensemble* are different, as clearly shown in Fig. 1.4 [10]. First the position of the tricritical points, which connect the first order curve to the second order one, is not the same, thus implying that there is a region in which the canonical phase transition is first order, while the microcanonical one is second order. It is precisely in this region that the specific heat is negative. Again this is a general fact that we here learned with reference to a specific application: The region with negative specific heat develops in correspondence of a first oder transition in the canonical ensemble. Back to the BEG model, in the microcanonical *ensemble*, beyond the tricritical point, the temperature experiences a jump at the transition energy. The

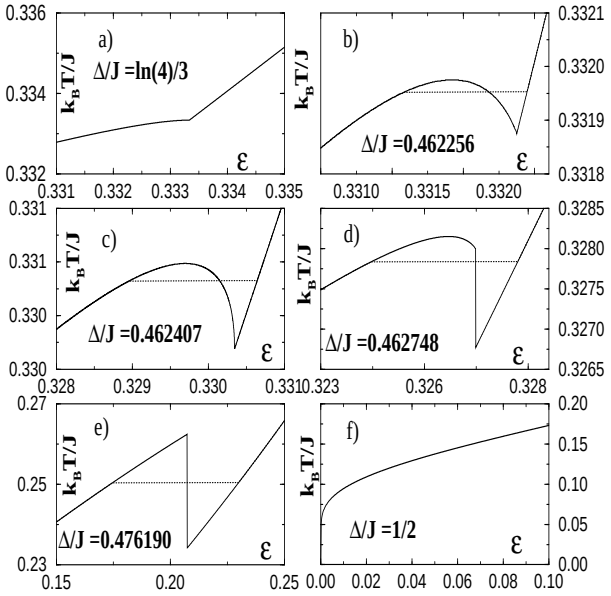

Figure 1.5: Caloric curves for the Blume-Emery-Griffiths model. Δ/J is the ratio between a local coupling term and the global ferromagnetic coupling. Figure is taken from Ref. [12].

two lines emerging on the right side from the microcanonical tricritical point (MTP) correspond to the two limiting temperatures, which are reached when approaching the transition energy from below and from above.

Let us now turn to clarifying the temperature-energy relation $T(e)$ and associated temperature jump as identified above. Also this curve displays two branches, as shown in Fig. 1.5: A high energy branch, corresponding to the homogeneous state, and a low energy branch relative to the magnetized phase. Fig. 1.5a corresponds to the canonical tricritical point (CTP). Here, the lower branch of the curve has a zero slope at the intersection point. Thus the specific heat of the magnetized phase diverges at this point. This effect signals the canonical tricritical point, as it appears in the microcanonical ensemble. Increasing Δ up to a value in the region between the two tricritical points a *negative specific heat* in the microcanonical *ensemble* first arises ($\partial T/\partial e < 0$, see Fig. 1.5b). At the microcanonical tricritical point the derivative $\partial T/\partial e$ of the lower branch diverges, yielding a vanishing specific heat (Fig. 1.5c). For larger values of Δ/J a jump in the temperature appears at the transition energy (Fig. 1.5d). The lower temperature corresponds to $m = 0$ solution and the upper one is the temperature of the magnetized ($m \neq 0$) solution at the transition point.

1.3 Non-equilibrium dynamical properties

As previously mentioned, long-range systems also present intriguing out-of-equilibrium features. When dealing with systems driven by short-range couplings (e.g. a gas of neutral particles), out-of equilibrium initial conditions does not significantly influence the subsequent dynamical evolution. After a short transient, the system converges (exponentially fast) to thermal equilibrium, where the property of ergodicity is satisfied. At odd with this vision, interesting and unexpected dynamical behaviours can develop, when considering long-range couplings. Simulations in the microcanonical *ensemble* can for instance reveal that the system is not ergodic, implying that only a limited portion of the accessible phase space is visited during the dynamical evolution. More importantly, when starting far from equilibrium, long-range systems typically get trapped in the so-called Quasy Stationary States (QSSs), intermediate regimes which persist for a long time (diverging with the numbers of degrees of freedom) before the system relaxes to the deputed thermal equilibrium. This interesting phenomenon is one of the topics addressed in this Thesis.

Before elaborating on the QSS concept, we introduce another interesting dynamical phenomenon as investigated in [15]. There an Ising model with both short and long-range interactions was analyzed. Such a model describes a system of spins mathematically specified by the following Hamiltonian:

$$H = -\frac{K}{2}\sum_{i=1}^{N}(S_i S_{i+1} - 1) - \frac{J}{2N}\left(\sum_{i=1}^{N} S_i\right)^2 , \tag{1.13}$$

where $S_i = \pm 1$. Molecular dynamics simulations demonstrated that the accessible region of extensive parameters (energy, magnetization, etc.) may be non convex. This implies that *broken ergodicity* can appear, due to the fact that the accessible magnetization states, at a given energy, can be disconnected. An example is illustrated in Fig. 1.6 which compares two different situations: on the one hand (panel a) different magnetized states are accessible in a microcanonical simulation. In the other case a magnetization gap forbids transitions between different states (panel (b)). Random dynamics is performed using the microcanonical Creutz algorithm [16].

1.4 Quasi Stationary States (QSSs)

As anticipated, long-range systems get frozen in Quasi Stationary States (QSSs), i.e. apparently stable states that persist for long time, followed then by a slow relaxation to the thermal equilibrium.
These regimes are for instance encountered within the framework of the celebrated Hamiltonian Mean Field (HMF) model, a paradigmatic mean-field model to which we shall be making extensive reference in the following. Without entering into the details of its mathematical formulation, we shall simply

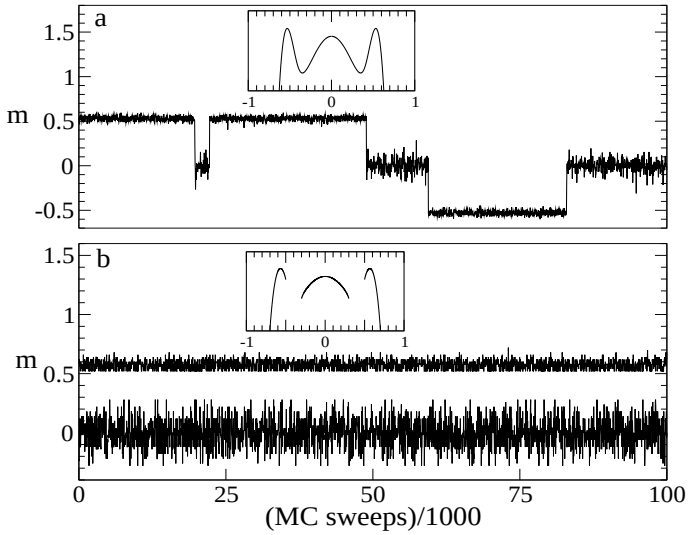

Figure 1.6: Time evolution of the magnetization for $K = -0.4$ (a) in the ergodic region ($\epsilon = -0.318$) and (b) in the non-ergodic region ($\epsilon = -0.325$). The corresponding entropy curves are shown in the inset. Figure is from Ref. [15].

mention that the HMF model describes the coupled evolution of N rotators confined on a unitary circle. When it comes to characterizing the dynamics, it is customary to refer to the global magnetization which provides a sensible measure for the degree of clusterization of the particles on the ring (see Section 3.1).

Starting from an out-of-equilibrium initial condition, after a violent relaxation, the systems gets stuck in a QSS, as confirmed by visual inspection of Fig. 1.7, where the magnetization amount is reported as function of time. Such picture is also particularly instructive to elucidate the dependence of the duration of QSSs on the system size. The relaxation to thermal equilibrium is driven by granularity and the QSSs lifetime, T, diverges with the number of particles N. For a particular class of initial conditions, a power law $T \propto N^{\nu}$ is shown to accurately reproduce the life time scaling, the exponent being $\nu \simeq 1.7$. This rather unusual scaling was for the first time observed by Yamaguchi *et al.* in [17].[2] These latter observations extend to a vast realm of physical systems and emphasizes the importance of deriving a consistent theoretical framework for the QSSs emergence. In real physical systems, in fact a huge number of particles is often involved, so making virtually infinite the time to equilibration. QSSs are hence the solely regime experimentally observable.

As a reference example we quote the case of Single-Pass Free Electron

[2] All along this thesis, we shall elaborate on the correctness of the proposed scaling, providing novel numerical evidence.

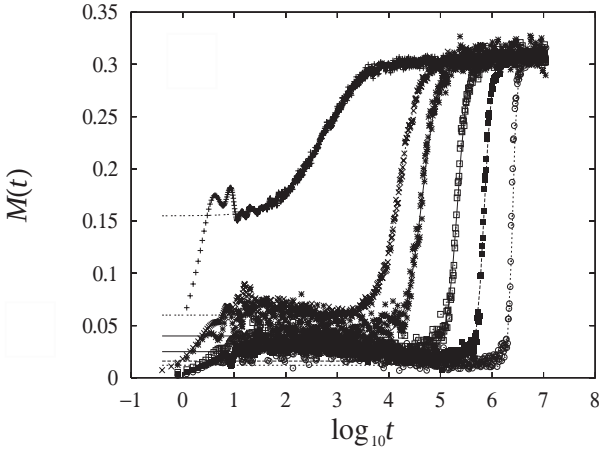

Figure 1.7: Temporal evolution of the magnetization $M(t)$ for different particles numbers: $N = 10^2(10^3)$, $10^3(10^2)$, $2.10^3(8)$, $5.10^3(8)$, $10^4(8)$ and $2.10^4(4)$ from left to right (the number between brackets corresponding to the number of samples).

Laser (FEL). This is an experimental device which exploits the interaction of a relativistic electron beam with a magnetostatic field to produce powerful laser light, with tunable wave-length. Under particular assumptions (which are generally consistent with a typical experimental set up), the evolution of the system can be modelled by a one-dimensional Hamiltonian model (Colson-Bonifacio) [18]. This model is quite general and shares striking similarities with other systems characterized by wave-particle interactions, e.g. the Travelling Wave Tube and CARL (Collective Atoms Recoil Laser) [19, 20]. After an initial violent relaxation, in which the intensity grows exponentially, an apparent stationary regime is attained, where small oscillations are displayed around a well defined *plateau*. Here, however, the average intensity is lower than the final level which is eventually attained at thermal equilibrium: Only after a finite time the system experiences a slow relaxation which takes the intensity towards the value predicted by Boltzmann-Gibbs statistics. An indirect signature that such states emerge far from equilibrium is also provided by the particles velocity distribution functions: In the QSSs the latter present strong non Gaussian features [21], which clearly cannot be captured by equilibrium statistical mechanics treatments.

In the last decades, several attempts have been proposed aiming at providing a systematic theoretical description of QSSs. The most successfull interpretative scenario is inspired to a maximum entropy principle, based on Lynden-Bell theory [9]. It was recently proven in a series of paper [22, 23, 24, 25] that Lynden-Bell theory enables one to predict with a good accuracy the relevant macroscopic observables associated to the QSSs. In Chapter 3 we shall review the Lynden-Bell theory, and present its main predictions with reference to the HMF case study. Despite this success, and the demonstrated predictive ade-

quacy of the Lynden-Bell *ansatz*, many open problems still remain which make the puzzle of QSSs origin and stability a fascinating one.

1.5 Examples of systems with long-range interactions

A growing scientific community has recently begun to tackle the problem of long-range interactions with different viewpoints [10, 26, 3, 12, 27]. Long-range interatcions are in fact ubiquitous and prove central in both fundamental applications and a large variety of physical systems and experiments, that are currently under development. In the following subsections we will briefly discuss the most relevant examples.

Gravitational systems. The first important example of long-range interactions is given by the gravitational potential:

$$V(\vec{r}) = -\frac{K}{|\vec{r}|}. \tag{1.14}$$

In this case $d = 3$ and $\alpha = 1$. The singularity at the origin makes the study of this interaction particularly hard, and generate phenomena like the "gravitational collapse". To avoid this latter, it is customary to introduce a dedicated regularization. Clearly, gravity plays a central role in astrophysics and cosmology, especially as for as the problem of structure formation in the expanding universe is concerned [28].

Plasmas. Rarefied plasmas share many similarities with collisionless stellar systems. In particular the mean-field drives the evolution and it is more important than the local fields of individual nearby particles. Here, again, the Coulomb force is of long-range type, and, as for the gravitational case, $d = 3$ and $\alpha = 1$. However, as opposed to the previous example, plasmas have both positive and negative charges: Hence they are neutral on large scales and can form static homogeneous equilibria. An important example in the context of plasma physics is played by the so-called beam-plasma instability: When a weak electron beam is injected into a thermal plasma, electrostatic modes at the plasma frequency (Langmuir modes) are destabilized [3]. The interaction of Langmuir waves and electrons constituting the beam is studied in the framework of a self-consistent one dimensional Hamiltonian, which bears an universality character being also found in other disciplinary contexts where wave-particles interactions are central [3, 18].

Free Electron Lasers. As already anticipated, the Free Electron Lasers (FELs) represent innovative laser sources, that provide tunable powerful light, even at very small wave-length [29]. The physical mechanism responsible for light emission and amplification is the interaction between a relativistic electron beam, a magnetostatic periodic field generated by an undulator and an

optical wave co-propagating with the electrons. Under realistic assumptions, the longitudinal dynamics of the system can be described by a one dimensional model [18]: The particles do not interact directly with each other, but are indirectly coupled via the external field, which in turn provides the long-range connection (in this case $d = 1$ and $\alpha = 0$).

2D Hydrodynamics. Two-dimensional incompressible hydrodynamics represents another important application where the interactions are of long-range nature [30]. Indeed, the stream function ψ is related to the modulus of the vorticity ω, via the Poisson equation $\triangle\psi = \omega$. Using the Green's function technique, one easily finds that the solution is

$$\psi(\vec{r}) = -\frac{1}{2\pi}\int_D d^2\vec{r}'\omega(\vec{r}')G(\vec{r}-\vec{r}') \quad , \tag{1.15}$$

where $G(\vec{r}-\vec{r}')$ depends on D, but $G(\vec{r}) \sim |\ln\vec{r}|$, when $r \to 0$. The kinetic energy being conserved by the Euler equation (dissipative-less), it is straightforward to compute it on the domain D, with boundary ∂D,

$$\begin{aligned} E &= \int_D d^2\vec{r}\frac{1}{2}(\nabla\psi)^2 \\ &= \oint_{\partial D}\vec{n}dl\nabla\psi + \frac{1}{2}\int_D d^2\vec{r}\omega(\vec{r})\psi(\vec{r}) \\ &= -\frac{1}{4\pi}\int\int_D d^2\vec{r}d^2\vec{r}'\omega(\vec{r}')\omega(\vec{r})\ln|\vec{r}-\vec{r}'|, \end{aligned} \tag{1.16}$$

since $\psi = 0$ on ∂D. This result confirms that logarithmic interactions are involved. The long-range character becomes even more explicit if one approximates the vorticity field by point vortices $\omega(\vec{r}) = \sum_i \Gamma_i\delta(\vec{r}-\vec{r}_i)$, located at $\vec{r}_i$, with a given circulation Γ_i. The energy of the system reads now:

$$E = \frac{1}{2}\sum_{i\neq j}\Gamma_i\Gamma_j\ln|\vec{r}_i-\vec{r}_j|. \tag{1.17}$$

The vortices' interaction has a logarithmic character, which corresponds to $\alpha = 0$. We remark that Eq. (1.17) is nothing but the energy due to vortices in 2D XY model.

Small systems. In addition to large systems, where the interaction are truly long-range, one should consider small systems where the range of the interactions is of the order of the system size. Also in this case the system is not additive, and many similarities with a pure long-range setting are displayed. Phase transitions are universal properties of interacting matter which have been widely studied in the thermodynamic limit of *infinite* systems. However, in many physical situations this limit is not attained and phase transitions

should be considered from a more general perspective. This is the case for specific microscopic or mesoscopic systems: atomic clusters can melt, small drops of quantum fluids may undergo a Bose-Einstein condensation or a superfluid phase transition, dense hadronic matter is predicted to merge in a quark and gluon plasma phase, while nuclei are expected to exhibit a liquid-gas phase transition. Given the above, it is mandatory to develop a general understanding of phase transition for a *finite* systems.

Most of the theoretical approaches that have been proposed to explain the peculiar behaviour of systems with long-range interactions are currently under development. It is therefore important to define dedicated toy-models, suitable for theoretical analysis, which enable to address the rich phenomenology of long-range systems. A paradigmatic, though particular class of long-range system is characterized by mean-field models. An emblematic example, already mentioned above, is the Curie-Weiss model, where discrete spin variables are associated to each node of a fully coupled network, and mutually interact as prescribed by Hamiltonian (1.2). This model is a a long-range system with $\alpha = 0$, and constitutes an important entry to the wider class of non-zero α systems. The model can be straightfowardly characterized in terms of its associated statistical equilibrium properties. It becomes however intriguingly complex when allowing for an effective dilution of the underlying network of connections, i.e. reducing the average number of links per node. Exploring the modification induced by the dilution to the equilibrium solution, as well as investigating the role of finite size corrections, represents the main objective of the next chapter. Being also interested in the out-of-equilibrium diluted dynamics we will subsequently consider the presence of QSSs in an "ad hoc" modified version of the celebrated HMF model. In Chapter 4, a novel analytical treatment targeted to the short time evolution will be discussed and, in Chapter 5, the role of dilution inspected via numerical simulations.

Chapter 2

Dilute Ising model on random graph

Among mean-field models the Ising model plays a central role. It can be studied in its fully coupled version (Curie-Weiss model) or on a specific graph[1] topology. Most studies have so far focused on the finite connectivity scaling, that is graphs such that the number of sites N and number of bonds M go to infinity, keeping the ratio N/M fixed. Models defined on such graphs have been extensively studied in the physics literature, especially in the context of spin glasses and combinatorial optimization. Several recent mathematical works also analyze rigorously Ising models on such networks [31, 32, 33, 34, 35]. Besides the fully coupled case, which as we commented previously constitute a reference case study for the broad class of long-range interacting systems, comparatively very few works are devoted to the infinite connectivity scalings, where N, M and M/N all go to infinity. Bovier and Gayrard [36] showed rigorously that, under an appropriate rescaling, the Ising model defined on such graphs is completely equivalent in the infinite N limit to its fully connected ($M = N(N-1)/2$) counterpart. On the basis of this finding, it can be safely conjectured that analogous conclusions apply to other spin models when inspected on a similar geometry.
The rigorous result by Bovier and Gayrard leaves however open the question of the speed of convergence towards the fully connected limit. Finite size effects are indeed crucial when aiming at understanding the behavior of a finite graph. Given a finite random graph with relatively high connectivity, two different approaches may be used to address this issue: on one hand, one might consider expanding around the fully connected solution of [36], to compute the leading order finite-N corrections; on the other hand, the graph under scrutiny can

[1] In mathematical term a network is represented by a graph. A graph is a pair of sets $G = \{P, E\}$, where P is a set of N points or nodes (in this case spins) and E is a set of M edges or links [8].

be seen as a realization of an Erdős-Rényi[2] random graph [37], with high, but finite, mean connectivity. This observation enables one to employ the powerful techniques developed for this latter scaling.
In this chapter we investigate the finite size corrections to the equilibrium magnetization of a diluted Ising model performing both computations, the first by resorting to the celebrated replica trick; the second, by means of the cavity method. Theoretical estimates will be then compared to numerical simulations, performed for different sizes and connectivities, in order to test their accuracy.
The kind of randomness we will focus on is a *quenched* type: The underlying graph is generated in the beginning and the macroscopic observables estimated by averaging over several independent realizations. This procedure is opposed to the *annealed* scenario, where links are allowed to vary on timescales comparable to those governing the evolution of individual degrees of freedom.
As expected, the system displays a phase transition of the mean-field type for all the considered values of γ at the transition temperature of the fully connected (Curie-Weiss) graph.
We will also bring convincing evidences that finite size corrections do play an important role in presence of a diluted network and thus need to be carefully addressed. The underlying objective is to start investigating the effect of dilution in a reference case study for the broad class of long-range interacting systems. The problem of inspecting the out-of-equilibrium modification as induced by the dilution will be commented upon in the forthcoming chapters, with reference to the HMF case study.

2.1 The model

We here consider an Ising model defined on a uniform random network topology. The network is made of N sites, each tagged by a discrete counter i, which ranges from 1 to N. On each site sits an Ising spin variable $S_i = \pm 1$. Two randomly selected nodes, say i and j, are connected through a coupling constant J_{ij}. The number of links N_L is bounded from above by $\widetilde{N} = N(N-1)/2$, which corresponds to the fully connected case, since we are avoiding double edging of two sites and self wiring. We introduce the dilution parameter γ by scaling the number of links as $N_L = \binom{N}{\gamma} = N^\gamma/\gamma!\,(1 + O(1/N))$, the normalization factor $\gamma!$ is introduced so that the fully connected topology is exactly reproduced when $\gamma \to 2$. We restrict our analysis to the interval $1 < \gamma \leq 2$, which corresponds to network topologies that range from a number of links growing linearly with the size of the system ($\gamma = 1$) up to the fully connected case ($\gamma = 2$).

[2] Erdős-Rényi graph is a random graph constructed as follows: Imagine to have a *ensemble* of N nodes; every pair of nodes is then connected with probability p. As p increase from 0 to 1 the total number of edges increases and scales as $\binom{N}{2}p$ for a graph of N vertices.

The Hamiltonian of the Ising model on such a diluted network is

$$H = -\frac{N}{2N_L} \sum_{i \neq j} J_{ij} S_i S_j. \tag{2.1}$$

With this scaling of the coupling constant the energy is extensive. In the simplest formulation, J_{ij} is set to an identical reference value, say $J > 0$, if the nodes i and j are connected, zero otherwise. In the following we shall study the behaviour of the system as a function of the dilution rate γ. As proved in [36], for γ strictly larger than its lower bound 1, a second order phase transition of the Curie-Weiss type always occurs. Our main goal is to characterize the behaviour of the system for a finite size N. In the following we start by analyzing the large N limit. The partition function Z reads

$$Z = \sum_{\{S_i\}} \exp\left(\frac{\beta N}{2N_L} \sum_{i \neq j} J_{ij} S_i S_j\right) = \sum_{\{S_i\}} \prod_{i \neq j} \exp\left(\frac{\beta N}{2N_L} J_{ij} S_i S_j\right) , \tag{2.2}$$

where β stands for $1/k_B T$, where k_B is the Boltzmann constant and T the system's temperature. The outer sum in Eq. (2.2) extends over all possible spin configurations. The coupling factor J_{ij} is related to the linking probability via the following condition

$$J_{ij} = \begin{cases} J & \text{with probability } p \\ 0 & \text{with probability } 1-p \ , \end{cases} \tag{2.3}$$

where p is

$$p = N_L / \widetilde{N} = \frac{2}{\gamma!} N^{\gamma - 2} \left(1 + O\left(\frac{1}{N}\right)\right) \ . \tag{2.4}$$

The $O(1/N)$ term in the probability represents subdominant finite size effects, and plays no role in the following. The probability distribution $P(J_{ij})$ reads

$$P(J_{ij}) = p\delta(J_{ij} - J) + (1-p)\delta(J_{ij}) \ . \tag{2.5}$$

We end this section by showing that for all $1 < \gamma \leq 2$, this system is exactly equivalent, in the $N \to \infty$ limit, to the fully coupled Curie-Weiss model. This is a non rigorous rephrasing of the main result in Ref. [36], which will set the stage for the finite-N studies of the following sections.

We want to compute $\langle \ln Z \rangle_J$, where $\langle \cdot \rangle_J$ denotes the average over disorder. This is achieved via the celebrated replica trick, which is based on the identity

$$\langle \ln Z \rangle_J = \lim_{n \to 0} \frac{\langle Z^n \rangle_J - 1}{n} \ , \tag{2.6}$$

where n is a assumed to be a real number. The central idea consists in carrying out the computation for all integers n, extending the results for all n, and performing in the end the limit for $n \to 0$.

In our setting the replicated partition function reads

$$\begin{aligned} Z^n &= \big[\sum_{\{S_i\}} \exp\left(-\beta H\right)\big]^n = \\ &= \sum_{\{S_i^a\}} \exp\left(\frac{\gamma!}{2}\beta\frac{1}{N^{\gamma-1}}\sum_a\sum_{i\neq j} J_{ij}S_i^aS_j^a\right) = \\ &= \sum_{\{S_i^a\}} \exp\left(\frac{\gamma!}{2}\beta\frac{1}{N^{\gamma-1}}\sum_{i\neq j} J_{ij}\sum_a S_i^aS_j^a\right) \ , \end{aligned} \tag{2.7}$$

where the index a runs over the n replicas.

Averaging over the disorder returns

$$\begin{aligned} \langle Z^n\rangle_J &= \sum_{J_{ij}} P(J_{ij}) \sum_{\{S_i^a\}} \exp\left(\frac{\gamma!}{2}\beta\frac{1}{N^{\gamma-1}}\sum_{i\neq j} J_{ij}T_{ij}\right) = \\ &= \sum_{\{S_i^a\}}\sum_{J_{ij}} P(J_{ij}) \prod_{i\neq j} \exp\left(\frac{\gamma!}{2}\beta\frac{1}{N^{\gamma-1}}J_{ij}T_{ij}\right) \ , \end{aligned} \tag{2.8}$$

where $T_{ij} = \sum_a S_i^aS_j^a$. Recalling Eq. (2.5), one straightforwardly obtains

$$\langle Z^n\rangle_J = \sum_{\{S_i^a\}}\prod_{i\neq j}\big[1 - \frac{2}{\gamma!}\frac{1}{N^{2-\gamma}} + \frac{2}{\gamma!}\frac{1}{N^{2-\gamma}}e^{\frac{\gamma!}{2}\beta\frac{1}{N^{\gamma-1}}T_{ij}}\big]. \tag{2.9}$$

where J is set to 1. To proceed further, we now expand the exponential function to its second order approximation, which immediately yields

$$\begin{aligned} \langle Z^n\rangle_J &= \sum_{\{S_i^a\}} \exp\Big(\sum_{i\neq j} \ln\big[1 - \frac{2}{\gamma!}\frac{1}{N^{2-\gamma}} + \\ &+ \frac{2}{\gamma!}\frac{1}{N^{2-\gamma}}\big(1 + \frac{\gamma!}{2}\beta\frac{1}{N^{\gamma-1}}T_{ij} + \frac{1}{2}\frac{\gamma!^2}{4}\beta^2\frac{1}{N^{2\gamma-2}}T_{ij}^2 + ...\big)\big]\Big), \end{aligned} \tag{2.10}$$

and, expanding the logarithm

$$\langle Z^n\rangle_J = \sum_{\{S_i^a\}} \exp\Big(\sum_{i\neq j}\big[\frac{\beta}{N}T_{ij} + \frac{\gamma!}{4}\frac{\beta^2}{N^\gamma}T_{ij}^2 - \frac{1}{2}\frac{\beta^2}{N^2}T_{ij}^2\big]\Big) \ . \tag{2.11}$$

Keeping only the leading order in N, we have

$$\begin{aligned}
\langle Z^n \rangle_J &= \sum_{\{S_i^a\}} \exp\Big(\sum_{i\neq j} [\frac{\beta}{N} T_{ij}] \Big) = \\
&= \sum_{\{S_i^a\}} \exp\Big(\frac{\beta}{N} \sum_a \sum_{i\neq j} S_i^a S_j^a \Big) = \\
&= \left[\sum_{\{S_i\}} \exp\Big(\frac{\beta}{N} \sum_{i\neq j} S_i S_j \Big) \right]^n = \\
&= [Z_{MF}]^n \,, \qquad (2.12)
\end{aligned}$$

where Z_{MF} is the partition function of the Curie-Weiss model. Thus, we recover the fact that at leading order in N, the dilute model is equivalent to the fully coupled one for all $1 < \gamma \leq 2$. We can calculate the Z_{MF} using by using the Hubbard-Stratonovich transformation

$$\exp\big(ba^2\big) = \sqrt{\frac{b}{\pi}} \int_{-\infty}^{+\infty} dx \exp\big(-bx^2 + 2abx\big) \;, \qquad (2.13)$$

The partition function Z_{MF} (hereafter simply Z) can be cast in the form

$$\begin{aligned}
Z &= \sum_{\{S_i\}} \exp\left(\frac{\beta}{N} (\sum_i S_i)^2 \right) = \qquad (2.14) \\
&= \sum_{\{S_i\}} \exp\left(\frac{N^2\beta}{N} (\frac{(\sum_i S_i)}{N})^2 \right) = \\
&= \sqrt{\frac{\beta N}{\pi}} \sum_{\{S_i\}} \int_{-\infty}^{+\infty} dx \exp\left(-\beta N x^2 + 2\beta N \sum_i \frac{S_i x}{N} \right) = \\
&= \sqrt{\frac{\beta N}{\pi}} \int_{-\infty}^{+\infty} dx \exp\big(-\beta N x^2\big) \sum_{\{S_i\}} \exp\left(2\beta N \sum_i \frac{S_i x}{N} \right) \;,
\end{aligned}$$

where $a = (\sum_i S_i)^2$ and $b = \beta N$ and eventually

$$Z = \sqrt{\frac{\beta N}{\pi}} \int_{-\infty}^{+\infty} dx \exp\big(-N(\beta x^2 - \ln(2\cosh(2\beta x)))\big) \;. \qquad (2.15)$$

The free energy function results in

$$\begin{aligned}
-\beta F &= \lim_{N\to\infty} \frac{1}{N} \ln Z_N = \qquad (2.16) \\
&= \lim_{N\to\infty} \frac{1}{N} \ln \Big[\sqrt{\frac{\beta N}{\pi}} \int_{-\infty}^{+\infty} dx \exp\Big(-N\big(\beta x^2 - \ln(2\cosh(2\beta x))\big)\Big) \Big] \;,
\end{aligned}$$

and using the saddle point approximation

$$-\beta F = \max_x[-\beta x^2 + \ln(2\cosh(2\beta x))]. \tag{2.17}$$

The magnetization of the system $m = \lim_{N\to\infty} \sum_i S_i/N$ is obtained by solving the implicit equation

$$m = \tanh(2\beta m) \ . \tag{2.18}$$

The critical inverse temperature, $\beta_c = 1/2$, separates the non magnetized phase from the magnetized one. The probability distribution function of the magnetization can be calculated from the free energy $F(m)$ as

$$P(m) = \frac{1}{Z(\beta)} \sum_{\{\mathcal{C}|m(\mathcal{C})=m\}} \exp\left(-\beta F(m) N\right) \ , \tag{2.19}$$

where $\mathcal{C}$ represents the subsets of spins configurations that have magnetization equal to m. For small m, one can expand $F(m)$ in powers of m and obtain

$$P(m) \propto \exp\left(-c_2 m^2 - c_4 m^4\right) \ . \tag{2.20}$$

At the critical point $\beta_c = 1/2$, one gets $c_2 = 0$ and $c_4 = 1/12$. We stress once again that all these results do not depend on γ in the $N \to \infty$ limit.

In the following section, we will discuss the numerical implementation, test the above infinite N theory and quantify the finite size corrections.

2.2 Numerical simulations

The properties of the system are numerically studied via the Metropolis Monte Carlo algorithm [38]. We focus on the quenched scenario and reconstruct the average distribution of the main quantities of interest by averaging over several realizations of the graph of connections.

2.2.1 Annealed solution

Before going forward we give the annealed solution of the model (2.1). Averaging the partition function Eq. (2.2) over the J_{ij}'s, using the probability distribution (2.3), one straightforwardly obtains

$$\begin{aligned}\langle Z\rangle_J &= \sum_{\{S_i\}} \prod_{<i,j>} [1 - \frac{2}{\gamma!} N^{\gamma-2} + \frac{2}{\gamma!} N^{\gamma-2} e^{\frac{\gamma!\beta}{2N^{\gamma-1}} S_i S_j}] = \\ &= \sum_{\{S_i\}} \exp[\sum_{i,j} \ln(1 - \frac{2}{\gamma!} N^{\gamma-2} + \frac{2}{\gamma!} N^{\gamma-2} e^{\frac{\gamma!\beta}{2N^{\gamma-1}} S_i S_j})].\end{aligned} \tag{2.21}$$

To proceed further we shall recall that $\gamma > 1$, an observation which in turn allows us to expand in power of $1/N$ the above expression. The following expression is formally recovered

$$\langle Z \rangle_J = \sum_{\{S_i\}} \exp\big(\frac{J\beta_N}{2N} \sum_{i,j} S_i S_j\big) \ , \tag{2.22}$$

where the finite N temperature, β_N, reads

$$\beta_N = \beta + J^2\beta^3 \left(\frac{\gamma!^2}{24N^{2\gamma-2}} - \frac{\gamma!}{4N^\gamma} + \frac{1}{3N^2} \right) \ . \tag{2.23}$$

In the above derivation we made use of the fact that $(S_iS_j)^m = 1$ for m even and $(S_iS_j)^m = S_iS_j$ otherwise. In the limit for $N \to \infty$, Eq. (2.23) implies $\beta_N \to \beta$, which in turn implies

$$\langle Z \rangle_J = \sum_{\{S_i\}} \exp\big(\frac{J\beta}{2N} \sum_{i,j} S_i S_j\big) \ , \tag{2.24}$$

for each value of the γ parameter. The annealed solution is thus also equivalent to the fully coupled graph solution, in the $N \to \infty$ limit. For finite N, Eq. (2.23) implies a modification of the temperature due to finite size effects. According to Eq. (2.23), we can imagine to replace the finite N system at temperature $T = 1/k_B\beta$ with its Curie-Weiss counterpart, provided a slightly smaller value of the temperature is allowed. This finding would in turn suggest that the finite graininess of the distribution drives an increase of the critical temperature. Consequently, one would expect to observe an inhomogeneous state at the mean-field transition temperature. This is at variance with what is found in our (quenched) simulations, where an opposite tendency is manifested, see below.

2.2.2 Numerical results

The simulated system reproduces well the phase transition, the actual value of the temperature associated with symmetry breaking depending on the number of simulated spins. To test the scenario discussed in the previous section, we first estimate β_c using the so-called Binder cumulant [39], defined as

$$U_N(T) \equiv 1 - \frac{\langle m^4 \rangle}{3\langle m^2 \rangle^2} \ , \tag{2.25}$$

where $\langle m^2 \rangle$ and $\langle m^4 \rangle$ denote respectively the second and fourth moments of the magnetization. The Binder cumulant is computed for different values of the imposed temperature. These numerical experiments are repeated for distinct values of N, while keeping γ fixed. The obtained profiles U_N vs. T are reported in Fig. 2.1 for various values of γ. Notice that we have introduced a subscript N

to recall that the plotted profiles are reconstructed from finite N calculations. The importance of the cumulant concept stems from the observation that curves corresponding to different N all intersect at approximately the same temperature, which provides an estimate of the critical temperature $T_c = 1/\beta_c$ in the infinite N limit. A direct inspection of the enclosed figures suggests that, for all values of γ scanning the relevant interval $(1.2, 1.7)$, $T_c = 2$. This result is in agreement with the convergence to the mean-field limit irrespectively of γ. Clearly, the convergence to the mean-field solution is expected to be faster for larger values of γ. Indeed, Fig. 2.1, panel a), which refers to the case $\gamma = 1.2$, shows a less clear intersection in the interval of N covered by our investigations, when compared to similar plots depicted for larger values of γ.

More interestingly, working at finite N, one can monitor the magnetization and plot it as a function of the dilution parameter γ. Results are reported in Fig. 2.2 for two different choices of N (symbols): A tendency to asymptotically approach the mean-field reference (solid) line is clearly displayed, in agreement with the above scenario. Finite size corrections play however a crucial role, which deserves to be carefully addressed.

Aiming at shedding light onto this issue, we use in the following two different analytical methods to estimate the finite N corrections.

Finally let us return on the validity of the simple annealed calculation as discussed above. In Fig. 2.3. we also anticipate the results from the replica based analysis as developed of Section 2.4, which, as we shall see, shares the quenched viewpoint of direct simulation. A similar trend between simulations and replica calculations (though the matching is not perfect as commented afterwords) is observed. Conversely, the annealed prediction obtained from the mean-field magnetization associated to the finite N temperature (2.23), returns a striking different behaviour.

2.3 The replica method

The first method relies on the replica trick. Starting with the calculations of Section 2.1, we now include the leading order finite N corrections. We start again from Eq. (2.11), which we recall here

$$\langle Z^n \rangle_J = \sum_{\{S_i^a\}} \exp\Big(\sum_{i \neq j} \big[\frac{\beta}{N} T_{ij} + \frac{\gamma!}{4} \frac{\beta^2}{N^\gamma} T_{ij}^2 - \frac{1}{2} \frac{\beta^2}{N^2} T_{ij}^2 \big] \Big) \ . \tag{2.26}$$

The largest neglected term in this expansion is $\frac{\gamma!^2}{24} \frac{\beta^3}{N^{2\gamma-1}} T_{ij}^{3\,3}$; including it would imply coupling three replicas and make the calculation technically more

[3] Note that the relative importance of the terms in Eq. (2.26) depends on the specific value of γ. As $\gamma < 3/2$, the first term here neglected dominates over the smallest included in the development. This observation sets the limit of our replica approximation and suggests that discrepances between the theory and the observations are to be expected in such a parameter interval.

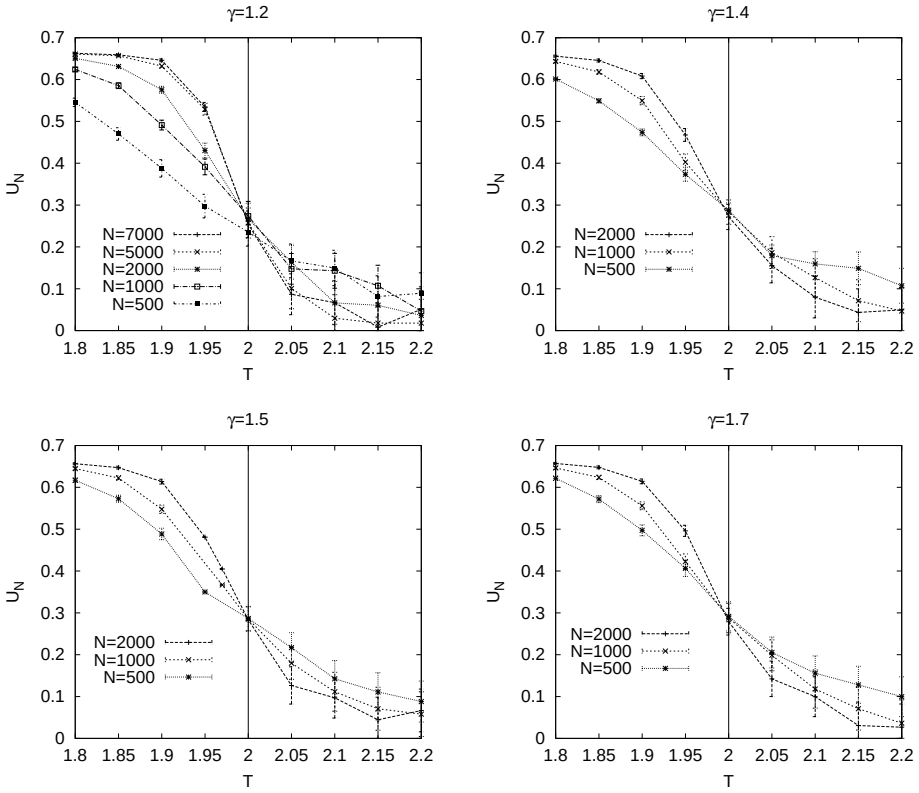

Figure 2.1: Binder cumulants U_N as a function of temperature T, for $\gamma = 1.2, 1.4, 1.5, 1.7$. The time averages are calculated over 4.10^4 Monte Carlo sweeps. The error bars are estimated with the resampling technique using 10 sets of 1000 sweeps and calculating the associated variance. In all panels the curves relative to $N = 500, 1000, 2000$ are reported. In addition, for $\gamma = 1.2$, the profiles relative to $N = 5000, 7000$ have been also included to better appreciate the convergence in N.

difficult. However, this term becomes progressively more important as γ approaches 1 from above; this may possibly affect the accuracy of the prediction derived here, in this region of parameters. In the following we shall also neglect $O(N^{-2})$ terms in expression (2.26), which is certainly well motivated as long as $\gamma < 2$ (in a strict sense).

Notice that the following relations apply

$$\sum_{i\neq j} T_{ij} = \sum_{i\neq j}\sum_{a} S_i^a S_j^a = \sum_{a}\sum_{i\neq j} S_i^a S_j^a = \sum_{a}\big(\sum_{i} S_i^a\big)^2 - Nn = N^2\sum_{a} m_a^2 - Nn\,, \tag{2.27}$$

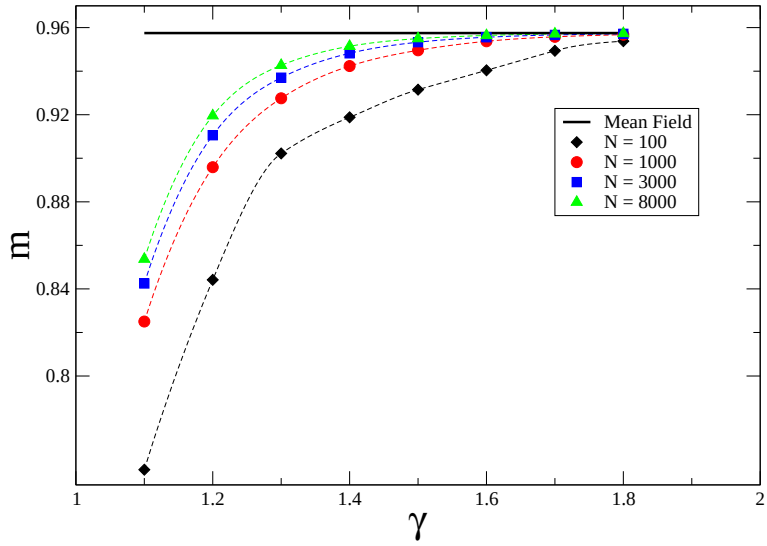

Figure 2.2: Magnetization versus γ for $\beta = 1$. Symbols refer to the quenched numerical simulations for, respectively, $N = 100$ (diamonds), $N = 1000$ (circles), $N = 3000$ (squares) and $N = 8000$ (triangles). Dashed lines are guides for the eye. The solid line stands for the mean-field solution (2.18).

and

$$\sum_{i\neq j} T_{ij}^2 = \sum_{i\neq j}\sum_{a,b} S_i^a S_j^a S_i^b S_j^b = \sum_{a,b}\Big(\sum_{i,j} S_i^a S_j^a S_i^b S_j^b - N\Big) = \tag{2.28}$$
$$= \sum_{a,b}\Big(\sum_i S_i^a S_i^b\Big)^2 - n^2 N = 2N^2 \sum_{a<b} m_{ab}^2 + nN^2 - n^2 N \ ,$$

where use has been made of the definitions

$$m_a = \sum_i S_i^a / N \ , \tag{2.29}$$

$$m_{ab} = \sum_i S_i^a S_i^b / N \ . \tag{2.30}$$

Substituting (2.27) and (2.29) into Eq. (2.11) yields

$$\langle Z^n \rangle_J = \sum_{\{S_i^a\}} \exp\left(\beta N \sum_a m_a^2 - n\beta + \frac{\gamma!\beta^2}{2} N^{2-\gamma} \sum_{a<b} m_{ab}^2 + \frac{\gamma!\beta^2}{4} N^{2-\gamma} n\right) \ , \tag{2.31}$$

where the term scaling as n^2 has been dropped (recall that we shall be concerned with the limit $n \to 0$).

The Hubbard-Stratonovich identity can now be invoked to rewrite the

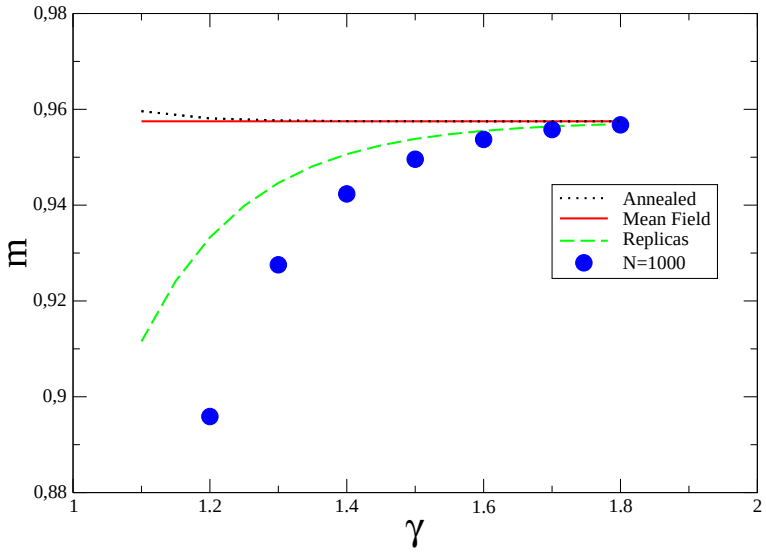

Figure 2.3: Magnetization versus γ for $\beta = 1$. The solid line refers to the mean-field solution; the dashed line stands for the replica based calculation; the dotted line represents the annealed perturbative estimate. Points represent numerical data for $N = 1000$.

above exponentials involving m_a^2 and m_{ab}^2

$$\exp\left(\beta N m_a^2\right) = \sqrt{\frac{\beta N}{\pi}} \int_{-\infty}^{\infty} d\lambda_a \exp\left(-\beta N \lambda_a^2 + 2\beta N m_a \lambda_a\right) \tag{2.32}$$

$$\exp\left(\frac{\gamma!\beta^2}{2} N^{2-\gamma} m_{ab}^2\right) = \sqrt{\frac{\gamma!\beta^2 N^{2-\gamma}}{2\pi}} \int_{-\infty}^{\infty} dq_{ab} \times \tag{2.33}$$
$$\times \exp\left(-\frac{\gamma!\beta^2}{2} N^{2-\gamma} q_{ab}^2 + \gamma!\beta^2 N^{2-\gamma} m_{ab} q_{ab}\right).$$

Putting the various pieces together, the average replicated partition function reads

$$\begin{aligned}
\langle Z^n \rangle_J &= C \sum_{\{S_i^a\}} \int_{-\infty}^{\infty} \prod_a d\lambda_a \prod_{a<b} dq_{ab} \times \\
&\times \exp\left(-\beta N \sum_a \lambda_a^2 + 2\beta N \sum_a m_a \lambda_a - \frac{\gamma!\beta^2}{2} N^{2-\gamma} \sum_{a<b} q_{ab}^2 + \gamma!\beta^2 N^{2-\gamma} \sum_{a<b} m_{ab} q_{ab}\right) \\
&= C \int_{-\infty}^{\infty} \prod_a d\lambda_a \prod_{a<b} dq_{ab} \exp\left(-\beta N \sum_a \lambda_a^2 - \frac{\gamma!\beta^2}{2} N^{2-\gamma} \sum_{a<b} q_{ab}^2\right) \times \\
&\times \sum_{\{S_i^a\}} \exp\left(2\beta N \sum_a m_a \lambda_a + \gamma!\beta^2 N^{2-\gamma} \sum_{a<b} m_{ab} q_{ab}\right),
\end{aligned} \tag{2.34}$$

where the normalization $C(\gamma,\beta,n,N)=\sqrt{\frac{\beta N}{\pi}}\sqrt{\frac{\gamma!\beta^2N^{2-\gamma}}{2\pi}}$ can be safely ignored in the forthcoming development.

Let us focus now on the last sum appearing in Eq. (2.34). A straightforward manipulation leads to

$$\begin{aligned}
&\sum_{\{S_i^a\}}\exp\Big(2\beta N\sum_a m_a\lambda_a+\gamma!\beta^2N^{2-\gamma}\sum_{a<b}m_{ab}q_{ab}\Big)=\\
=\;&\sum_{\{S_i^a\}}\exp\Big(2\beta N\sum_a\lambda_a\sum_i\frac{S_i^a}{N}+\gamma!\beta^2N^{2-\gamma}\sum_{a<b}q_{ab}\sum_i\frac{S_i^aS_i^b}{N}\Big)=\\
=\;&\left(\sum_{\{S^a\}}\exp\Big(2\beta\sum_a\lambda_aS^a+\gamma!\beta^2N^{1-\gamma}\sum_{a<b}q_{ab}S^aS^b\Big)\right)^N, \qquad (2.35)
\end{aligned}$$

where the index i can be removed, being replaced by the power N.

Let us now introduce the function Ψ as

$$\Psi(\lambda_a,q_{ab})=\sum_{\{S_a\}}\exp\Big(2\beta N\sum_a\lambda_aS^a+\gamma!\beta^2N^{1-\gamma}\sum_{a<b}q_{ab}S^aS^b\Big)\,. \qquad (2.36)$$

We now make the replica symmetric hypothesis which corresponds to setting $\lambda_a=\lambda$ and $q_{ab}=q\;\forall a,b$. After this *ansatz*, Ψ can be cast in the form

$$\Psi(\lambda,q)=\sum_{\{S_a\}}\exp\Big(2\beta\sum_a\lambda_aS^a+\gamma!\beta^2N^{1-\gamma}q\Big[\frac{1}{2}(\sum_aS^a)^2-\frac{n}{2}\Big]\Big). \qquad (2.37)$$

The Hubbard-Stratonovich trick allows us to write

$$\exp\left(\frac{\gamma!\beta^2}{2}N^{1-\gamma}q(\sum_aS^a)^2\right)=\sqrt{\frac{\gamma!}{2\pi}}\int_{-\infty}^{\infty}dx\exp\left(-\frac{\gamma!}{2}x^2+\gamma!\beta N^{\frac{1-\gamma}{2}}\sqrt{q}\sum_aS^ax\right) \qquad (2.38)$$

which leads to the following expression for Ψ

$$\begin{aligned}
\Psi(\lambda,q)\;&=\;\exp\left(-\frac{\gamma!\beta^2N^{1-\gamma}qn}{2}\right)\sqrt{\frac{\gamma!}{2\pi}}\int_{-\infty}^{+\infty}dx\exp\left(-\frac{\gamma!}{2}x^2\right)\times\\
&\quad\times\sum_{\{S_a\}}\exp\Big((2\beta\lambda+2\gamma!\beta N^{\frac{1-\gamma}{2}}\sqrt{q}x)\sum_aS^a\Big)=\\
&=\;\exp\left(-\frac{\gamma!\beta^2N^{1-\gamma}qn}{2}\right)\sqrt{\frac{\gamma!}{2\pi}}\int_{-\infty}^{+\infty}dx\exp\left(-\frac{\gamma!}{2}x^2\right)\times\\
&\quad\times\Big[2\cosh(2\beta\lambda+\gamma!\beta N^{\frac{1-\gamma}{2}}\sqrt{q}x)\Big]^n. \qquad (2.39)
\end{aligned}$$

Finally, we obtain

$$\langle Z^n\rangle_J=C\int_{-\infty}^{\infty}d\lambda dq\exp[NL_n]\;, \qquad (2.40)$$

where

$$L_n = \Big[-\beta n\lambda^2 - \frac{\gamma!\beta^2}{2} N^{1-\gamma} \frac{n(n-1)}{2} q^2 + \ln \Psi \Big] \ . \tag{2.41}$$

We want to keep the terms linear in n in Eq. (2.41), since they are the only ones to give a contribution in the limit $n \to 0$. A straightforward expansion in n yields, in the $n \to 0$ limit,

$$\begin{aligned} \frac{1}{n} \ln \Psi \ \longrightarrow \quad & -\frac{1}{2}\gamma!\beta^2 N^{1-\gamma} q + \ln 2 + \sqrt{\frac{\gamma!}{2\pi}} \int_{-\infty}^{+\infty} \exp\left(-\gamma! x^2/2\right) \times \\ & \times \ln\cosh\left(2\beta\lambda + \gamma!\beta N^{(1-\gamma)/2}\sqrt{q}x\right) \ dx \ . \end{aligned} \tag{2.42}$$

The computation of the free energy is now reduced to finding the saddle point of the following function

$$\begin{aligned} \phi(\lambda, q) \ = \ & -\beta\lambda^2 + \frac{\varepsilon^2}{4\gamma!} q^2 - \frac{\varepsilon^2}{2\gamma!} q + \ln 2 + \sqrt{\frac{\gamma!}{2\pi}} \int_{-\infty}^{+\infty} \exp\left(-\gamma! x^2/2\right) \times \\ & \times \ln\cosh\left(2\beta\lambda + \varepsilon\sqrt{q}x\right) \ dx \ , \end{aligned} \tag{2.43}$$

where we have introduced the small parameter

$$\varepsilon = \gamma!\beta N^{(1-\gamma)/2} \ . \tag{2.44}$$

Expanding in ε up to order ε^2 and performing the Gaussian integrations, we get

$$\phi(\lambda, q) = -\beta\lambda^2 + \ln\cosh 2\beta\lambda + \frac{\varepsilon^2}{4\gamma!} q^2 - \frac{\varepsilon^2}{2\gamma!} q \tanh^2 2\beta\lambda + \ln 2 + o(\varepsilon^2) \ . \tag{2.45}$$

At order ε^0, the conditions $\partial_\lambda \phi = 0$ and $\partial_q \phi = 0$ yield

$$\lambda_0 = \tanh 2\beta\lambda_0 \ , \ q_0 = \tanh^2 2\beta\lambda_0 \ . \tag{2.46}$$

As it should, the mean-field solution is recovered from these equations, see Eq. (2.18). We now write $\lambda = \lambda_0 + \varepsilon^2\lambda_1$, and we get from the condition $\partial_\lambda \phi = 0$

$$\lambda_1 = -\frac{1}{\gamma!} \frac{\lambda_0^3(1-\lambda_0^2)}{1 - 2\beta(1-\lambda_0^2)} \ . \tag{2.47}$$

The dummy parameter λ can be shown to correspond to the magnetization. Thus, one can compare the replica based prediction Eq. (2.47) (which takes into account the leading order finite N corrections) to direct numerical simulations. The comparison is made in Fig. 2.4, where the magnetization is plotted as a function of γ. The global trend is captured by Eq. (2.47); however the agreement deteriorates quickly for small values of γ. This may be due to the approximations involved in the calculation.

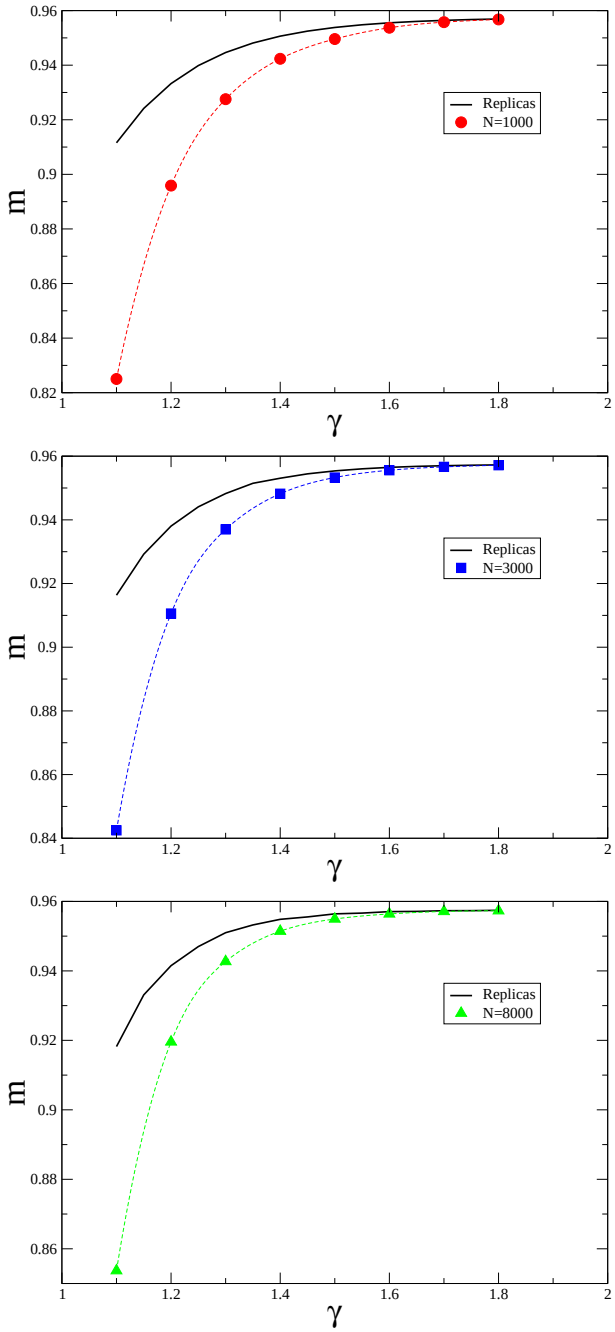

Figure 2.4: Magnetization versus γ for $\beta = 1$. Symbols refer to numerical simulations. From top to bottom: $N = 1000$ (circles), $N = 3000$ (squares) and $N = 8000$ (triangles). The dashed lines serves as a guide for the eye. The solid line stands for the replica based solution (2.47).

As a final step, let us compute the leading finite N correction to the transition temperature. We recall that its $N \to \infty$ value is $\beta_c = 1/2$. We compute the Hessian matrix $H_\phi(0,0)$ of ϕ in $(\lambda, q) = (0,0)$, getting

$$H_\phi(0,0) = \begin{pmatrix} 2\beta(2\beta-1) & 0 \\ 0 & \frac{\varepsilon^2}{2\gamma!} \cdot \end{pmatrix} \tag{2.48}$$

The critical temperature corresponds to a vanishing determinant for $H_\phi(0,0)$. We find, at order ε^2, $\beta_c = 1/2$. In conclusion, at this level of approximation, there is no modification of the critical temperature due to finite N effects.

We end this section with a comment. A given finite random graph with N sites and M links may be seen as a finite N realization of a dilute random graph as above, for some value of γ. It may also actually be seen as a finite N realization of a graph constructed according to the rule described in Eq. (2.4) and Eq. (2.5), with $p = \alpha N_L/\widetilde{N} \simeq \frac{2\alpha}{\gamma!} N^{\gamma-2}$. To each choice of $\gamma \in]1,2[$ corresponds a value of α. There is then an infinite number of models to which our graph at hand may be compared. This freedom could be in principle exploit to optimize the predictions for a finite N graph via tha replica based calculation. However, our analysis at first subleading order in $1/N$, does not depend on the specific choice of γ and α. This conclusion is reached above for the case $\alpha = 1$. In conclusion and limiting the dicussion to the first corrections here evaluated one can not take full advantage of the aforementioned flexibility intrinsic to the fromulation of the model.

2.4 An alternative approach: The cavity method

The method used in the previous section (expansion in powers of N coupled to a replica calculation) does not give very precise results for small to moderate values of γ. We now turn to an alternative theoretical approach to interpret the results of our simulations: a finite size graph with N sites, constructed with the rule (2.5) for a given γ, may be seen as a standard Erdős-Rényi random graph with parameter $\lambda_{ER} = N^{(\gamma-1)}/\gamma!$ (that represents the mean connectivity) [37, 40]. This makes possible the use of the powerful methods devised for finite connectivity random graphs, such as the cavity method.

The solution of the Ising model on random graphs with arbitrary distributions of links is given in [41, 42]; we follow here the formulation given in [43], which is there applied to the solution of an Ising spin glass on a Bethe lattices. Our case is much simpler, as we are studying a ferromagnet; a small complication is related to the probability distribution of the site connectivities.

We briefly recall the main steps leading to the (replica symmetric) cavity equations, following Ref. [43]. Consider the Hamiltonian (2.1) defined on a random graph. Figure 2.5 represents a node, denoted with 0, and its $k = 3$ neighbours. We represent by h_i, $i = 1, ..., k$ the total field acting on spin S_i *in the absence* of the central spin S_0. The magnetization of the i-th spin reads

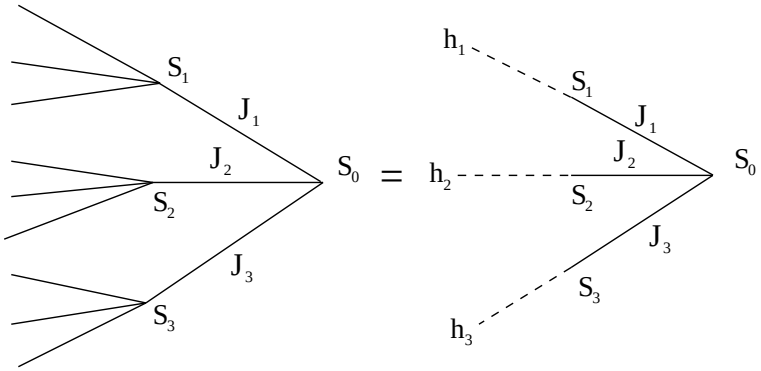

Figure 2.5: This figure shows an example of a tree-like structure with $k = 3$. The cavity fields h_i represent the total field acting on the spin S_i, when the central spin S_0 is removed.

$m_i = \tanh(\beta h_i)$. The basic ingredient of the cavity method is to assume that the fields h_i are uncorrelated.

Let us define the partition function of the spin S_0 as follows

$$Z_{S_0} = \sum_{S_0,S_1,..,S_k} \exp\left(\beta^{'} S_0 \sum_{i=1}^{k} J S_i + \beta^{'} \sum_{i=1}^{k} h_i S_i\right) , \tag{2.49}$$

where

$$\beta^{'} = \gamma! \frac{1}{N^{\gamma-1}} \beta \ . \tag{2.50}$$

One can now invoke the basic identity

$$\sum_{S_i=\pm 1} \exp\left(\beta^{'} S_0 J S_i + \beta^{'} h_i S_i\right) = c(J,h_i) \exp(\beta^{'} u(J,h_i) S_0) \ , \tag{2.51}$$

where the two functions $u(\cdot,\cdot)$ and $c(\cdot,\cdot)$ respectively read

$$u(J,h) = \frac{1}{\beta^{'}} \text{arc}\tanh[\tanh(\beta^{'} J)\tanh(\beta^{'} h)] \ , \tag{2.52}$$

$$c(J,h) = 2\frac{\cosh(\beta^{'} J)\cosh(\beta^{'} h)}{\cosh(\beta^{'} u(J,h))}, \tag{2.53}$$

and rewrite the partition function (2.49) as

$$Z_{S_0} = \sum_{S_0,S_1,..,S_k} \prod_{i=1}^{k} c(J,k_i) \exp\left(\beta^{'} \sum_{i=1}^{k} u(J,h_i) S_0\right) \ . \tag{2.54}$$

In practice the magnetization on site 0 is thus given by $m_0 = \langle S_0 \rangle = \tanh(\beta' h_0)$, where

$$h_0 = \sum_{i=1}^{k} u(J, h_i) \ . \tag{2.55}$$

The connectivity k of a given site in the finite size random graph we study is a random variable with distribution

$$\pi_0(k) = \frac{(N-1)!}{k!(N-1-k)!}(1 - N^{\gamma-2})^{N-k} N^{(\gamma-2)k} \ . \tag{2.56}$$

We want to compare our finite size random graph with the corresponding infinite size graph with the same Erdős-Rényi parameter $\lambda_{ER} = N^{\gamma-1}/\gamma!$. This graph has a Poissonian connectivity distribution with paramter λ_{ER}. Thus, we use in the cavity calculations the following distribution, which is close to (2.56),

$$\pi(k) = e^{-\lambda_{ER}} \frac{\lambda_{ER}^k}{k} \ . \tag{2.57}$$

Eqs. (2.55) and (2.57) allows one to write the following implicit relation for the probability density $Q(h)$ of local fields

$$Q(h) = \sum_k \pi(k) \int \prod_{i=1}^{k} [dh_i Q(h_i)] \delta(h - \sum_{i=1}^{k} u(J_i, h_i)). \tag{2.58}$$

Eq. (2.58) can be solved using a population dynamics algorithm [43] to access an estimate of the local field distribution $Q(h)$, and eventually compute the magnetization of the system. More concretely, one starts with arbitrarily chosen population of Ω fields and proceeds iteratively as follows. A random number k is picked up with probability $\pi(k)$; a subset of k fields is randomly selected in the population, and used to compute the h_0 field, as prescribed by Eq. (2.55). Then one field is removed at random from the population, and replaced with the computed h_0. Such a scheme defines a Markov chain on the space of the Ω fields which admits a stationary distribution. In the limit $\Omega \to \infty$ such a stationary distribution clearly satisfies the self-consistency relation (2.58). The magnetization m is hence straightforwardly recovered as $m = \sum_i \tanh(\beta' h_i)/N$.

This method provides very accurate predictions, as shown in Fig. 2.6, much better than the finite N expansion around the replica calculation discussed in Section 2.3.

Summing up, in this chapter we have investigated the finite size corrections to the equilibrium magnetization of the Ising model defined on a diluted network. Varying the dilution parameter γ, these networks interpolate between

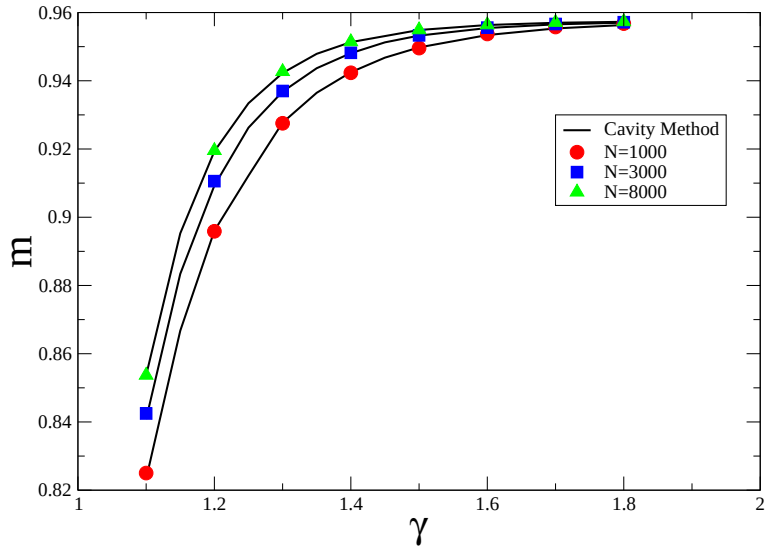

Figure 2.6: Magnetization versus γ for $\beta = 1$. Symbols refer to numerical simulations: $N = 1000$ (circles), $N = 3000$ (squares) and $N = 8000$ (triangles). The solid lines are the solution obtained using the cavity method. The agreement is much better than for the replica approach (see Fig.2.4).

the fully connected network ($\gamma = 2$) and the opposite setting where the number of links scales linearly with system size N ($\gamma = 1$). Systematic deviations with respect to the asymptotic mean-field behavior are observed when a finite number of spins is considered, such discrepancies being more pronounced as γ approaches its lower bound $\gamma = 1$. This phenomenon is clearly displayed in the plot of the magnetization m versus γ. A replica based perturbative analysis is developed, whose predictions are compared with the outcome of the numerics. The dependence of m on γ is qualitatively captured, but the quantitative match is not satisfying, especially as the dilution rate is increased. A cavity based calculation, inspired by the Mèzard-Parisi technique [43] is able to reproduce the data with an excellent degree of accuracy.
We have in conclusion brought convincing evidences that finite size corrections do play an important role in presence of a diluted network and thus need to be carefully addressed.

In the next chapter we turn to discussing the HMF model, the reference case study for out-of-equilibrium properties of long-range interacting systems. We will start by reviewing the existing literature, being particularly interested with the emergence of Quasi Stationary States. The final objective, persecuted in Chapter 5 will be to elucidate the effect of dilution on the out-of-equilibrium dynamics.

Chapter 3

The Hamiltonian Mean Field model: equilibrium and out-of-equilibrium features

---

The HMF [44] model belongs to the class of toy-models, specifically designed to investigate the properties of long-range systems. Toy models allow one to capture the basic physical modalities of a class of systems under scrutiny, often reproducing with a satisfying degree of accuracy the correct experimental phenomenology. In doing so they enable for a drastic reduction in complexity, and return an ideal playground for theoreticians.

When it comes to the HMF, we already recalled that it displays rather peculiar out-of-equilibrium features which are also shared by other physical systems [3, 29]. As we will clarify in the following, the HMF admits a Hamiltonian formulation in terms of continuous variables, at variance with the Curie-Weiss model analysed in the previous chapter. It is exactly solvable both in the canonical and microcanonical *ensembles*, leading in this case to equivalent results, and displays a second order phase transitions from homogeneous to magnetized distributions. In the last years, several extensions of the original formulation have been proposed, so to account among the other, for a spatial modulation of the the interaction [45], higher dimensionality (e.g. a 2D spatial version of the model here considered [46]) and refined coupling mechanisms [10]. In the following we shall however limit our discussion to the original HMF model.

When performing numerical simulations starting out-of-equilibrium, the system is usually trapped in long-lived Quasi Stationary States (QSSs), before relaxing to the deputed equilibrium solution. The QSSs display a rich phenomenology that was alluded to in the preceding discussion, and that will be further developed below. We shall be in particular concerned with reviewing

the literature devoted to the QSS and bring novel numerical insight on the relation between their lifetime and the system size. More specifically, this chapter is organised as follows. In the next section we will introduce the model and shortly discuss its equilibrium thermodynamics. Then, in Section 3.1.2, we will report on the out-of-equilibrium dynamics, with emphasis on the emergence of QSSs. Section 3.2 is devoted to discussing the continuous limit of the discrete N-body picture. This yields to the Vlasov equation which plays a crucial role in understanding the QSS properties, as discussed in Section 3.3. Finally, in the last section, we present new evidences relative to the lifetime of the QSS and discuss them with reference to the existing data in order to broaden and clarify the current picture.

3.1 The HMF model

The Hamiltonian Mean Field model [44] describes the motion of N particles on a ring (see Fig. 3.1) and is characterized by the following Hamiltonian

$$H = \frac{1}{2}\sum_{j=1}^{N} p_j^2 + \frac{\epsilon}{2N}\sum_{i,j=1}^{N}[1-\cos(\theta_i-\theta_j)] \tag{3.1}$$

where $\theta_j \in [0, 2\pi[$ represents the position (angle) of the j-th particle in the ring and p_j stands for its conjugate momentum. Once two particles comes to the same location, we can either think that they cross each other or collide elastically, since they share the same mass. Such a model is a nothing but a globally coupled XY model augmented with a kinetic term.
Depending on the coupling constant ϵ the interaction can be attractive ($\epsilon > 0$) or repulsive ($\epsilon < 0$). In this former (resp. latter) case, the HMF is obtained by retaining only the first harmonic of the one-dimensional self-gravitating [47] (resp. Coulomb charged planes) potential $V(x) \propto -|x|$ (resp. $V(x) \propto +|x|$) and assuming periodic boundary conditions [48]. The rescaling factor $1/N$ which appears in the potential term of Hamiltonian (3.1) is introduced to guarantee the energy extensivity and avoid divergences. This is the so-called Kac prescription [11]. The equations of motion follows from (3.1) and read:

$$\begin{aligned} \dot{\theta}_i &= \frac{\partial H}{\partial p_i} = p_i \\ \dot{p}_i &= -\frac{\partial H}{\partial \theta_i} = -\frac{\epsilon}{N}\sum_{j=1}^{N}\sin(\theta_i-\theta_j). \end{aligned} \tag{3.2}$$

To monitor the evolution of the system, it is customary to introduce the local magnetization vector $\mathbf{m}_i = (\cos\theta_i, \sin\theta_i)$ and the average (complex) magnetization $\overrightarrow{\mathbf{M}}$, a global order parameter whose norm reads:

$$M = \left|\overrightarrow{\mathbf{M}}\right| = |M_x + iM_y| = \left|\sum \mathbf{m}_i/N\right|. \tag{3.3}$$

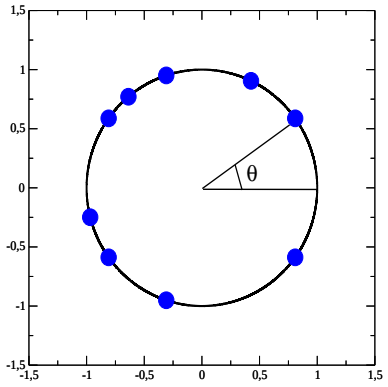

Figure 3.1: The Hamiltonian Mean Field model describes the coupled motion of a bunch of massive particles confined on a unit ring. The position of each particle is identified via the angle θ, as depicted in the cartoon.

The phase, ϕ, satisfies:

$$\tan(\phi) = \frac{M_y}{M_x}. \tag{3.4}$$

Making use of the above definition, Eqs. (3.2) can be cast in the form

$$\begin{aligned} \dot{\theta}_i &= p_i \\ \dot{p}_i &= -\epsilon M \sin(\theta_i - \phi). \end{aligned} \tag{3.5}$$

All along this thesis we shall concentrate on the ferromagnetic case ($\epsilon = 1$), this latter being the interesting scneraio when it comes to elucidating the emergent QSS dynamics [49, 44, 49].

3.1.1 Equilibrium thermodynamics

In the following we will discuss the equilibrium solution of the HMF. The discussion follows closely [50, 51]. The exact canonical solution of the HMF is obtained by applying the Hubbard-Stratonovich trick. The partition function for the HMF model reads in fact:

$$Z = \int \prod_{i=1}^{N} dp_i d\theta_i \exp(-\beta H), \tag{3.6}$$

where the integration is extended over all the phase space and β stands for the inverse temperature, $\beta = 1/(k_B T)$. Integrating over momenta, yields:

$$Z = \left(\frac{2\pi}{\beta}\right)^{N/2} \exp(-\frac{\beta N}{2}) J, \tag{3.7}$$

with

$$J = \int_0^{2\pi} \prod_{i=1}^{N} d\theta_i \exp\left[\frac{\beta}{2N} \sum_{i,j=1}^{N} \cos(\theta_i - \theta_j)\right] = \int_0^{2\pi} \prod_{i=1}^{N} d\theta_i \exp\left[\frac{\beta}{2N} \left(\sum_{i}^{N} \mathbf{m}_i\right)^2\right]. \quad (3.8)$$

In order to evaluate this integral, one resorts to the Hubbard-Stratonovich transformation in the $\mu > 0$ case, which takes the form:

$$\exp\left[\frac{\mu}{2}\mathbf{x}^2\right] = \frac{1}{\pi} \int_{-\infty}^{\infty}\int_{-\infty}^{\infty} d\mathbf{y} \exp[-\mathbf{y}^2 + \sqrt{2\mu}\mathbf{x} \cdot \mathbf{y}], \quad (3.9)$$

where $\mathbf{x}$ and $\mathbf{y}$ are two-dimensional vectors. Eq. (3.8) hence becomes

$$J = \frac{1}{\pi} \int_0^{2\pi} \prod_{i=1}^{N} d\theta_i \int_{-\infty}^{\infty}\int_{-\infty}^{\infty} d\mathbf{y} \exp[-\mathbf{y}^2 + \sqrt{2\mu} \sum_{i,j=1}^{N} \mathbf{m}_i \cdot \mathbf{y}], \quad (3.10)$$

with $\mu = \beta/N$. We can now exchange the order of the integrals in (3.10) and factorize the integration over the coordinates of the N particles. Introducing the rescaled variable $\mathbf{y} \to \mathbf{y}\sqrt{N/2\beta}$, one obtains

$$J = \frac{N}{2\pi\beta} \int_{-\infty}^{\infty}\int_{-\infty}^{\infty} d\mathbf{y} \exp\left[-N\left(\frac{y^2}{2\beta} - \ln(2\pi I_0(y))\right)\right], \quad (3.11)$$

where y is the modulus of $\mathbf{y}$ and I_0 represents the modified Bessel function of order 0. This latter integral can be evaluated with the saddle point technique in the mean-field limit ($N \to \infty$). In this limit, the Helmoltz free energy F reads:

$$F = -\lim_{N\to\infty} \frac{1}{\beta N} \ln Z = -\frac{1}{2} \ln\left(\frac{2\pi}{\beta}\right) + \frac{\beta}{2} + \max_{y}\left(\frac{y^2}{2\beta} - \ln(2\pi I_0(y))\right). \quad (3.12)$$

The maximization of the last term in (3.12) yields to the consistency equation:

$$\frac{y}{\beta} = \frac{I_1(y)}{I_0(y)}. \quad (3.13)$$

For $\beta < 2$ Eq. (3.13) has a minimal free energy solution for $y = 0$, which corresponds to a homogeneous equilibrium distribution with zero magnetization. On the contrary, for $\beta > 2$ the minimal free energy solution is a non-vanishing β-depending value $\bar{y}$ that can be deduced numerically, so specifying the magnetized equilibrium solution. The value of M for such non-homogeneous states is given by the ratio of the Bessel functions

$$M = \frac{I_1(\bar{y})}{I_0(\bar{y})}. \quad (3.14)$$

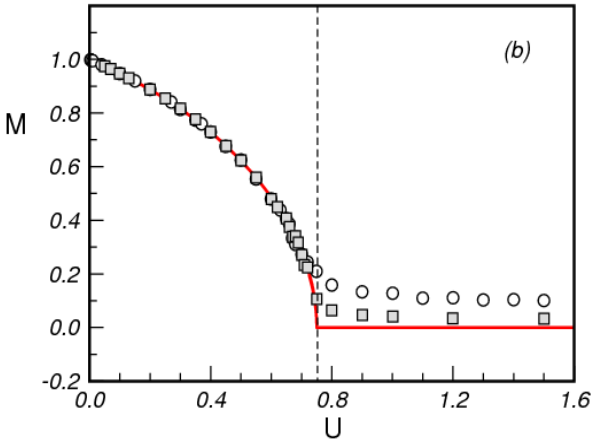

Figure 3.2: Equilibrium magnetization M as a function of the energy per particle U. Symbols refer to direct N-body simulations data for $N = 10^2$ and 10^3, while the solid line stands for the canonical prediction. The vertical dashed line points to the critical energy, which is located at $U_c = 0.75$, $\beta_c = 2$. The figure is from Ref. [51].

Hence, the system displays a phase transition at the critical temperature $\beta_c = 2$, which can be proven to be of the second order type[1] [44], with the exponent $1/2$.

This prediction is consistent with numerical simulations, as clearly displayed in Fig. 3.2. Here the equilibrium magnetization is plotted against the internal energy U of the system. This latter follows from the free energy as

$$U = \frac{\partial(\beta F)}{\partial \beta}, \tag{3.15}$$

which yields

$$U = \frac{1}{2\beta} + \frac{1 - M^2}{2}. \tag{3.16}$$

The temperature vs. the internal energy at equilibrium is reported in Fig. 3.3. Comparisons with numerical simulations are also displayed (see Ref. [51]).

With reference to the microcanonical *ensemble*, the first numerical experiments, performed at constant energy, showed that for energies slightly below the canonical phase transition, $U_c = \frac{1}{(2\beta_c)} + \frac{1}{2}$, the system rapidly relaxes to an apparent equilibrium different from the canonical one [44]. This finding was initially thought to be the fingerprint of inequivalence between microcanonical and canonical *ensemble*, considering the long-range nature of the interaction. However, it was later recognized that inequivalence only occurs when in presence of a first order canonical phase transition, which is not the case for the

[1] This means that the magnetization passes continuously from zero to a finite value, when decreasing the temperature (or increasing β).

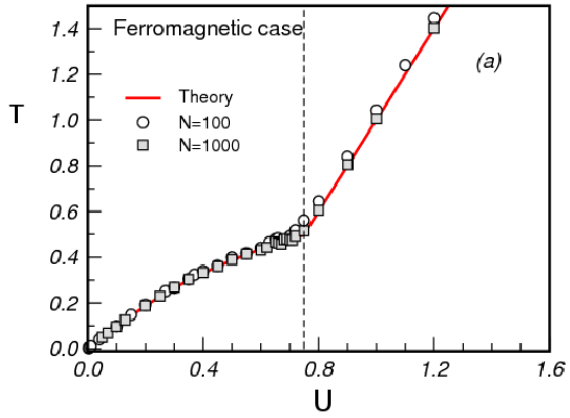

Figure 3.3: Equilibrium temperature T vs energy per particle U. Symbols refer to N-body simulations for $N = 10^2$ and 10^3, while the solid line stands for the canonical prediction. Figure is from Ref. [51].

HMF. Indeed, it was also rigorously proved [48, 52] that *ensembles* are equivalent for the case of the HMF, the Large Deviation technique being applied to derive the exact HMF microcanonical solution. The aforementioned disagreement as revealed by microcanonical simulations stems from the peculiar dynamical evolution of the HMF, which was subsequently found to occur also in other context [53]. The following section is devoted to discussing these important aspects into details.

3.1.2 On the emergence of QSS: Non-equilibrium dynamics

To investigate the HMF dynamics one has to perform direct (microcanonical) numerical simulations of eqs. (3.2). A careful numerical analysis suggests that the evolution of the system is very sensitive to the choice of the initial condition [44, 49, 54]. Depending on the specific traits of the initial particle distribution, the system can be frozen in long-lasting Quasi Stationary States [49]. In other words, there is no straight convergence to the Boltzmann distribution, and particles are apparently stuck in a intermediate regime, whose macroscopic characteristics strongly differ from the corresponding equilibrium configuration.

Yamaguchi *et al.* performed a comprehensive campaign of simulations employing a 4^{th}-order symplectic scheme, with a time step $\tau = 10^{-1}$. The system was initialized in the so-called "water-bag" distribution. This corresponds to imposing a uniformly occupied rectangle in phase space:

$$f(\theta, p, 0) = \begin{cases} f_0 = 1/(4\Delta\theta\Delta p) & \text{if } -\Delta p \leq p < \Delta p \text{ and } -\Delta\theta \leq \theta < \Delta\theta \\ 0 & \text{otherwise.} \end{cases} \tag{3.17}$$

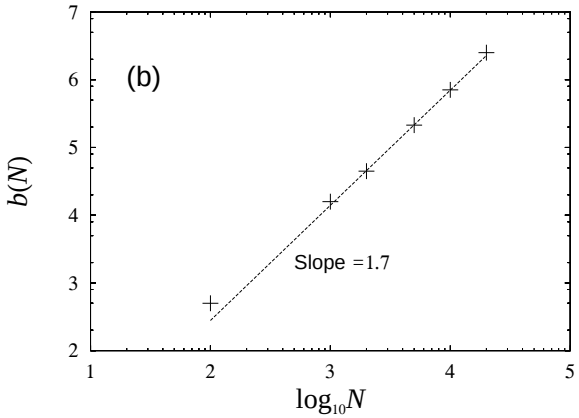

Figure 3.4: The timescale $b(N)$ as a function of $\log_{10} N$, as follows direct N-body simulation for an initial water-bag distribution with $M_0 = 0$ and $U = 0.69$.

This choice identifies a whole family of possible initial conditions parametrized via the quantities $\Delta\theta$ and Δp. By tuning $\Delta\theta$ and Δp we can adjust the specific characteristics of the selected profile in terms of associated anergy and initial magnetization.
The spatial coordinates θ_j are randomly chosen in the interval [-$\Delta\theta$,$\Delta\theta$[. For the special setting $\Delta\theta = \pi$ one obtains an initial magnetization of order $1/\sqrt{N}$, i.e. corrisponding to an homogeneous condition in the large N limit. The momenta p_j are also randomly chosen from the interval $[-\triangle p, \triangle p[$. With this choice, one can express the initial energy density $U = H/N$ and the initial magnetization as functions of $\Delta\theta$ and Δp:

$$M_0 = \frac{\sin(\Delta\theta)}{\Delta\theta}, \quad U = \frac{(\Delta p)^2}{6} + \frac{1 - (M_0)^2}{2}. \tag{3.18}$$

To monitor the system dynamics one can track the global magnetization as a function of time. The initial evolution takes place on timescale which are independent on the value of the simulated particles[2] N. Such an early evolution corresponds to the "violent relaxation" process, which brings the system towards the QSS. The lifetime τ_{QSS} of the QSS, i.e. the time that is necessary to abandon the intermediate phase and eventually jump to equilibrium, is instead increasing with the system size N. Yamaguchi's simulation, performed with reference to an initial homogeneous ($M_0 = 0$) water-bag, returned a power law divergence N^ν, with the rather surprising exponent $\nu = 1.7$ [17], see Fig 3.4. To extract a sound estimate of τ_{QSS}, Yamaguchi considered the log-lin plot of the magnetization time series, dropping the part relative to the violent relaxation. The sigmoid shape so obtained can be interpolated via the following ansazt:

[2]This observation is valid with exception of the initially homogeneous case, where the violent relaxation scales as $\log N$ [55].

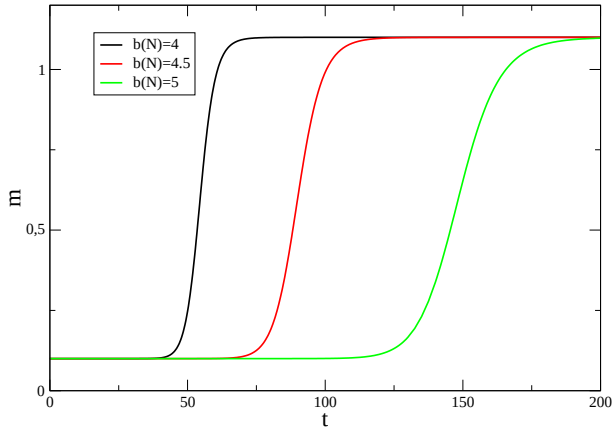

Figure 3.5: Function (3.19) is plotted for $a(N) = 10$, $c(N) = 0.5$, $d(N) = 0.1$ and for $b(N) = 4, 4.5, 5$ (green, red and black line respectively).

$$M(t) = [1 + \tanh(a(N)(\log_{10} t - b(N)))]c(N) + d(N) \tag{3.19}$$

where the best fit value for $b(N)$ returns an estimate for the duration of the intermediate lethargic phase, as $\tau_{QSS} = 10^{b(N)}$ and which yields to the scaling recalled above. Eq. (3.19) can be also re-written as

$$M(t) = [1 + \tanh(a(N)\log_{10}(\frac{t}{\tau_{QSS}}))]c(N) + d(N) \tag{3.20}$$

The parameters $c(N)$ and $d(N)$ are also adjusted by a proper fitting procedure and respectively represent the half-width between the initial and the equilibrium levels of $M(t)$ and the initial *plateau* of the magnetization. In Fig. 3.5 the function (3.19) is plotted for $a(N) = 10$, $c(N) = 0.5$, $d(N) = 0.1$ and three values of $b(N)$.
The important conclusion is hence that the lifetime of the QSS diverges when performing the thermodynamic limit $N \to \infty$. In such a limit, the system is permamently trapped in the out-of-equilibrium QSS and cannot eventually relax to the Boltzmann equilibrium. Such an intriguing observation implies that the limit for $t \to \infty$ and $N \to \infty$ do not commute. The system behaves in fact in a sensibly different fashion, depending on the order the two limits are taken. Importantly, and developing on this observation, QSSs can be seen as stable stationary equilibria of a continuous system, formally recovered from the original discrete formulation, when sending $N \to \infty$. As we shall prove in the forthcoming chapter, this procedure yields to the celebrated Vlasov equation, which is nowdays believed to return the correct interpretative framework for clarifying the puzzle of QSSs' emergence in presence of long-range interactions [21].

3.2 The continuous limit: the Vlasov equation

As anticipated, we are here concerned with deriving the continuous counterpart of the HMF Hamiltonian, i.e. its equivalent description which holds for diverging system size. To this end, one can invoke the rigorous result of Braun-Hepp [56] who cast the problem within a solid mathematical perspective. At variance, and to preserve physical intuition, we will here follow a kinetic theory argument which moves from the so called Klimontovich equation [57, 58].

3.2.1 A kinetic theory approach: The Klimontovich equation

We will start by considering a general one dimensional Hamiltonian setting. The derivation reported below closely follows Refs. [59, 12]. The discrete N-body Hamiltonian hence reads:

$$H = \sum_{i=1}^{N} \frac{p_i^2}{2} + U(\theta_i) \tag{3.21}$$

where $U(\theta_i)$ refers to the potential which we express as a function of the individual particles coordinates θ_i:

$$U(\theta_1, .., \theta_N) = \sum_{i<j}^{N} V(\theta_i - \theta_j). \tag{3.22}$$

The HMF clearly falls within the above realm. The state of the N-body system is specified by the discrete, one-particle, time dependent density function f_d given by:

$$f_d(\theta, p, t) = \frac{1}{N} \sum_{i=1}^{N} \delta(\theta - \theta_i(t))\delta(p - p_i) \tag{3.23}$$

where δ stands for the Dirac function, (θ, p) indicate the Eulerian coordinates in the phase space. (θ_i, p_i) is the Lagrangian coordinates of the i-th particle, whose dynamics is ruled by the following equations of motion:

$$\begin{aligned} \dot{\theta}_i &= p_i \\ \dot{p}_i &= -\frac{\partial U}{\partial \theta_i}. \end{aligned} \tag{3.24}$$

Differentiating with respect to time the one-particle density (3.23) and making use of equations (3.24) one gets

$$\frac{\partial f_d(\theta, p, t)}{\partial t} = -\frac{1}{N} \sum_{i=1}^{N} p_i \frac{\partial}{\partial \theta} \delta(\theta - \theta_i(t))\delta(p - p_i(t)) + \frac{1}{N} \sum_{i=1}^{N} \frac{\partial U}{\partial \theta_i} \frac{\partial}{\partial p} \delta(\theta - \theta_i(t))\delta(p - p_i(t)). \tag{3.25}$$

Recalling that $a\delta(a-b) = b\delta(a-b)$ one can re-write the previous equations as:

$$\frac{\partial f_d(\theta,p,t)}{\partial t} = -\frac{1}{N}\sum_{i=1}^{N} p\frac{\partial}{\partial\theta}\delta(\theta-\theta_i(t))\delta(p-p_i(t)) + \frac{1}{N}\sum_{i=1}^{N}\frac{\partial v}{\partial\theta}\frac{\partial}{\partial p}\delta(\theta-\theta_i(t))\delta(p-p_i(t)) \tag{3.26}$$

where:

$$v(\theta,t) = N\int d\theta' dp' V(\theta-\theta') f_d(\theta',p',t) \tag{3.27}$$

which eventually yields to the well-known Klimontovich equation:

$$\frac{\partial f_d}{\partial t} + p\frac{\partial f_d}{\partial\theta} - \frac{\partial v}{\partial\theta}\frac{\partial f_d}{\partial p} = 0. \tag{3.28}$$

This equation is still exact, even for a finite number of particles N, and contains the information about the orbit of every single particle. Klimontovich equation is especially useful as a starting point for deriving approximate equations that enables one to describe the average properties of the system under scrutiny. One can in particular perform a perturbative development with respect to the system size, so to obtain an indication of the so called mean-field like approximation. More specifically, one can pose:

$$f_d = \langle f_d(\theta,p,t)\rangle + \frac{1}{\sqrt{N}}\delta f(\theta,p,t) = f_0(\theta,p,t) + \frac{1}{\sqrt{N}}\delta f(\theta,p,t) \tag{3.29}$$

where $f_0(\theta,p,t) = \langle f_d(\theta,p,t)\rangle$ represents the averaged one-particle density function. The average is here taken over a large set of independent microscopic initial realizations, relative the same macroscopic state [12]. Inserting (3.29) in (3.27) clearly implies:

$$v(\theta,t) = \langle v\rangle(\theta,t) + \frac{1}{\sqrt{N}}\delta v(\theta,t) \tag{3.30}$$

where the first term reads:

$$\langle v\rangle(\theta,t) = N\int d\theta' dp' V(\theta-\theta') f_0(\theta',p',t) \tag{3.31}$$

Inserting both expression (3.29) and (3.30) into the Klimontovich equation one obtains:

$$\frac{\partial f_0}{\partial t} + p\frac{\partial f_0}{\partial\theta} - \frac{\partial\langle v\rangle}{\partial\theta}\frac{\partial f_0}{\partial p} = -\frac{1}{\sqrt{N}}\Big(\frac{\partial\delta f}{\partial t} + p\frac{\partial\delta f}{\partial\theta} - \frac{\partial v}{\partial\theta}\frac{\partial f_0}{\partial p} - \frac{\partial\langle v\rangle}{\partial\theta}\frac{\partial f}{\partial p}\Big) + \frac{1}{N}\frac{\partial\delta v}{\partial\theta}\frac{\partial\delta f}{\partial p}. \tag{3.32}$$

Averaging the above equation over f_{in}, finally yields to:

$$\frac{\partial f_0}{\partial t} + p\frac{\partial f_0}{\partial\theta} - \frac{\partial\langle v\rangle}{\partial\theta}\frac{\partial f_0}{\partial p} = \frac{1}{N}\Big\langle\frac{\partial\delta v}{\partial\theta}\frac{\partial\delta f}{\partial p}\Big\rangle \tag{3.33}$$

Equation (3.33) is still exact. Performing the limit for $N \to \infty$, so neglecting finite size corrections, one ends up with the Vlasov equation, namely:

$$\frac{\partial f_0}{\partial t} + p\frac{\partial f_0}{\partial \theta} - \frac{\partial \langle v \rangle}{\partial \theta}\frac{\partial f_0}{\partial p} = 0 \tag{3.34}$$

This ultimately defines the correct framework to investigate the origin of QSSs. These are in fact intermediate out-of-equilibrium regimes of the discrete dynamics, which become stable solutions of the corresponding continuous picture.

As opposed to the Klimontovich derivation, the Braun-Hepp theorem [56] states that, for a mean-field microscopic two-body smooth potential, the distance between two initially close solutions of the Vlasov equation increases at most exponentially in time. If we apply this result to a large N approximation of a continuous distribution, the error at $t = 0$ is typically of order $1/\sqrt{N}$, thus for any "small" ϵ and any "large enough" particle number N, there is a time t up to which the dynamics of the original Hamiltonian and its Vlasov description coincide, within error bounded by ϵ. The theorem implies that such a time t increases at least as $\ln N$, and is linked with the faster possible instability of the Vlasov dynamics.
Since quasi-stationary states evolve on time scale that diverge with N, the Braun-Hepp result suggests that QSSs might gain their stability from being "close" to some stable stationary states of Vlasov dynamics. One can expect that this associated slow evolution takes place passing through different stable Vlasov stationary states.
At this stage the system is trapped close to one of the numerous stable stationary states of the Vlasov equation. This state may be the statistical equilibrium of the Vlasov equation. An interpretation of this process is the Lynden-Bell statistics, that will be discussed in the next section.

3.2.2 On the properties of the Vlasov equation

The discrete dynamics of equations (3.24) conserves the average energy per particle $e(p, q) = H(p, q)/N$ and other selected quantities depending on the symmetry properties of the potential $V(q)$ (e.g. the average momentum for translational invariant potentials, as it is the case for the HMF model). The Vlasov equation (3.34) clearly conserves the very same constants of motion, which are to be properly expressed in term of the particles distribution f. As an example, the average energy density reads

$$h[f] = \int\int dpdqf(p, q)\frac{p^2}{2} + \int\int dpdqf(p, q)\phi(q), \tag{3.35}$$

and similar relations are straightforwardly derived for the other quantities involved. Importantly, the total mass

$$\mu[f] = \int \int dpdqf(p,q), \tag{3.36}$$

is also conserved, which in turn corresponds to keeping constant the number of particles in the discrete scenario. In addition, the Vlasov dynamics (3.34) also preserves the following quantities:

$$C_n[f] = \int \int dpdqf^n(p,q). \tag{3.37}$$

usually referred to as to Casimirs [3]. This is indeed a crucial property, which makes the Vlasov dynamics interestingly rich. As we shall demonstrate, the formal distinctions between the aforementioned Lynden-Bell statistics (i.e. the statistical mechanics of the Vlasov picture) and the conventional Boltzmann-Gibbs description stem from these unique characteristics.

3.2.3 The Vlasov equation for the HMF

Making explicit reference to the case of the HMF, the following version of the Vlasov equation (3.34) is readily recovered when taking the continuum limit:

$$\frac{\partial f}{\partial t} + p\frac{\partial f}{\partial \theta} - \{M_x[f]\sin(\theta) - M_y[f]\cos(\theta)\}\frac{\partial f}{\partial p} = 0, \tag{3.38}$$

with $M_x[f] = \int f\cos(\theta)d\theta dp$ and $M_y[f] = \int f\sin(\theta)d\theta dp$. System (3.38) conserves the energy

$$h[f] = \int \int (p^2/2)f(\theta,p,t)\mathrm{d}\theta\mathrm{d}p - (M_x^2 + M_y^2 - 1)/2 \tag{3.39}$$

and the average momentum

$$P[f] = \int \int pf(\theta,p,t)\mathrm{d}\theta\mathrm{d}p \tag{3.40}$$

as well as the normalization of the distribution

$$\mu[f] = \int \int f(\theta,p,t)\mathrm{d}\theta\mathrm{d}p = 1. \tag{3.41}$$

The adequacy of such a scheme can be also tested via direct numerical simulations. We here present the computer simulations performed by Antoniazzi *et al.* aimed at confronting the N-body scenario to its corresponding continuous picture [60]. The algorithm employed to solve the Vlasov system in phase space is based on the so-called "splitting scheme", a common strategy in numerical fluid dynamics. N-body simulations are performed for various choices of the

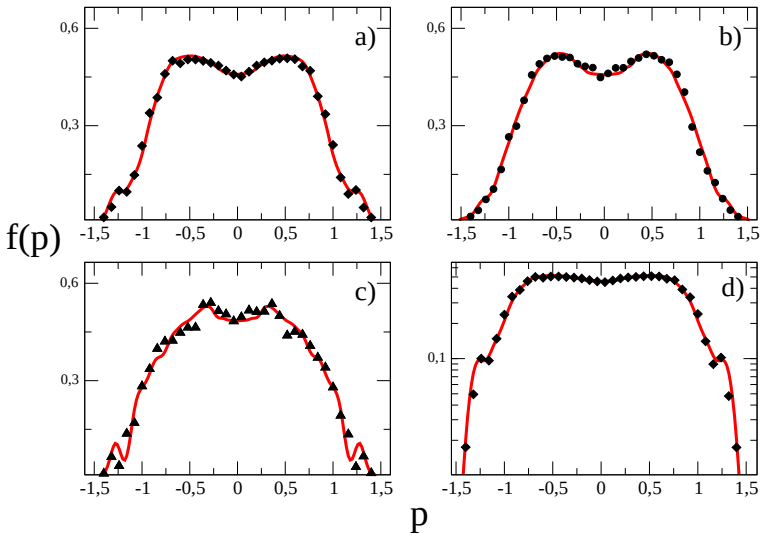

Figure 3.6: Particle velocity distribution functions for $U = 0.69$ and different initial magnetization: (a) $M_0 = 0.3$, (b) $M_0 = 0.5$, (c) $M_0 = 0.7$. The solid lines refer to the solutions of the Vlasov equation (3.38), while the symbols correspond to the N-body simulations. The picture in (d) is the same as (a), but it has been plotted in logarithmic scale, in order to emphasize the agreement in the tails of the distributions. The figure is taken from [60].

number of simulated particles (10^3 to 10^6). As it should be clear from the above, one expects that the macroscopic observables measured in the Hamiltonian discrete setting superpose to the homologous Vlasov quantities, over a time interval which gets progressively larger for increasing N. This conclusion is unambiguosly reached in [60]. We here solely present the comparison between the velocity probability distribution functions relative respectively to the continuum and N-body settings: The profiles are reported in Fig. 3.6 and display an excellent agreement. Curves refer to a large enough number of simulated particles ($N = 10^6$), with respect to the selected time of integration (the larger the number of N the longer the time for which the agreement is expected to hold). Motivated by such a nice correspondence, one wish to gain analytical insight into the QSS by resorting to the Vlasov scenario. This is eventually achieved by elaborating on the Lynden-Bell maximum entropy principle, to which next section is entirely devoted.

3.3 Lynden-Bell statistics explains the QSS and reveals the exixtence of an out-of-equilibrium phase transition

The approach proposed by Lynden-Bell, and presented in his seminal paper in 1967 [9], is elaborated within cosmological context and aims at explaining the observable stars distributions in elliptical galaxies. For infinite number interacting bodies, the system reduces in fact to a Vlasov equation, gravity being the governing force. Similarly to what observed above, galaxies are QSS which do correspond to statistical equilibria of the Vlasov dynamics. After an initial rapid evolution, the function f becomes progressively more filamented and stirred at smaller and smaller scales, without attaining any final stable equilibrium. However, averaging over larger windows in phase space which encompass the above filamentations, one obtains a coarse-grained function $\bar{f}$ that is smooth and likely to converge toward an equilibrium state.

Thus, assuming the dynamics of each coarse-grained element of f to satisfy a mixing hypothesis during the violent relaxation process, one can naturally infer that the QSS corresponds to a statistical equilibrium of equation (3.34). Like in the usual Boltzmann approach, one assumes that all the possible microstates are visited with the same probability, during the mixing dynamics. Hence the equilibrium is obtained as the most probable macrostate $\bar{f}$, i.e. the one that maximizes the mixing entropy, consistent with all the constraints imposed by the dynamics.

We shall here focus on the family of water-bag initial distributions, which correspond to a uniformly occupied rectangle in phase space (θ, p) (3.17). The mixing entropy is the logarithm of the number of microscopic configurations associated with the same macroscopic state characterized by the probability density $\bar{f}(\theta, p)$ [9, 61, 62]:

$$s = \ln[W(\{\bar{f}\})]. \tag{3.42}$$

To get the number W the phase space is discretized into a finite number of macrocells $[q, q + dq] \times [p, p + dp]$, the volume $dp \times dq$ being much smaller than the whole phase space. Dividing these macrocells in ν microcells with size h smaller than the fine-grained distribution, these can be either occupied by the level f_0 or 0, one excluding the other, similarly to Pauli principle. A combinatorial calculation detailed in [9, 51] yields to the final expression:

$$s(\bar{f}) = -\int \left[\frac{\bar{f}}{f_0}\ln\frac{\bar{f}}{f_0} + \left(1 - \frac{\bar{f}}{f_0}\right)\ln\left(1 - \frac{\bar{f}}{f_0}\right)\right] \mathrm{d}\theta\, \mathrm{d}p. \tag{3.43}$$

where in particular the limit $(h\nu) \to 0$ has been performed. Let us emphasize that this conclusion is fully justified from first principle and follows a direct counting process, as in the spirit of conventional statistical mechanics. The initimate nature of the Vlasov dynamics enters the picture via the exclusion principle, a direct consequence of the Casimirs invariance which makes the

Lynden-Bell statistics very similar to the Fermi-Dirac one. The analogy is purely formal since the contexts are different, as already emphasized in [21, 61]. Moreover, it is worth stressing that in the limit $f_0 \to \infty$ such additional contribution can be neglected: The usual Boltzmann-Gibbs statistics is hence recovered.

In order to compute the equilibrium distribution, one has to maximize expression (3.43), while imposing the conservation of the invariants. Consider the HMF model and refer to the water-bag initial conditions (3.17), the two levels being respectively $f_0 = 1/(4\Delta_\theta \Delta_p)$ and 0. Each element of the water-bag family is completely specified by the associated internal energy U and initial magnetization $\mathbf{M}_0 = (M_{x0}, M_{y0})$ [3].

The maximum entropy solution is derived from the constrained variational problem:

$$S(e,\sigma) = \max_{\bar{f}} \left(s(\bar{f}) \middle| h(\bar{f}) = e; P(\bar{f}) = \sigma; \int \mathrm{d}\theta \mathrm{d}p \bar{f} = 1 \right) . \tag{3.44}$$

The problem is solved by introducing three Lagrange multipliers β/f_0, λ/f_0 and μ/f_0 for respectively energy, momentum and normalization. This leads, after some calculations, to the following analytical form of the distribution

$$\bar{f}(\theta,p) = f_0 \frac{e^{-\beta(p^2/2 - M_y[\bar{f}]\sin\theta - M_x[\bar{f}]\cos\theta) - \lambda p - \mu}}{1 + e^{-\beta(p^2/2 - M_y[\bar{f}]\sin\theta - M_x[\bar{f}]\cos\theta) - \lambda p - \mu}}. \tag{3.45}$$

Again we notice that this latter differs from the Boltzmann-Gibbs distribution because of the "fermionic" denominator which is originated by the form of the entropy. Besides, it clearly manifests non-Gaussian features in the core, while the tails decay exponentially, as for usual Maxwellian profile.

The variational problem (3.45) results in a system of implicit equations that can be tackled numerically. Multiple stationary solutions are in principle possible. To identify the global maximum, which in turn corresponds to the equilibrium state, one has to punctually evaluate the entropy in correspondence of the selected stationary points. Depending on the predicted value of $M = \sqrt{M_x^2 + M_y^2}$, we can ideally distinguish between two distinct regimes: The homogeneous case corresponds to $M \simeq 0$ (non-magnetized), while the non-homogeneous (magnetized) setting is found for $M \neq 0$ distributions. Indeed the predictions of the Lynden-Bell equilibrium (3.45) are derived scanning the parameter plane (M_0, U), which we recall univocally identify the initially selected water-bag distribution. The underlying scenario, as first recognized in [25], is depicted in Fig. 3.7. When fixing the initial magnetization

[3] In general, one should consider also the average momentum $P = \int dpd\theta p f_0$, but we here assumed the distributions to be centered around $(\theta, p) = (0, 0)$, which clearly implies $P = 0$. This is not a restrictive choice: a non-zero average momentum results in the same evolution, with the superposition of a constant translational drift.

and decreasing the energy density, the system undergoes a phase transition, from homogeneous to magnetized QSS. The plane can be then formally divided into two zones respectively associated to an ordered non-homogeneous phase, $M_{QSS} \neq 0$, (lower part of Fig. 3.7), and a disordered homogeneous state, $M_{QSS} = 0$ (upper part). These regions are separated by a transition line, collection of all the critical points (M_0^c, U^c), which can be segmented into two distinct parts. The dashed line corresponds to a second order phase tran-

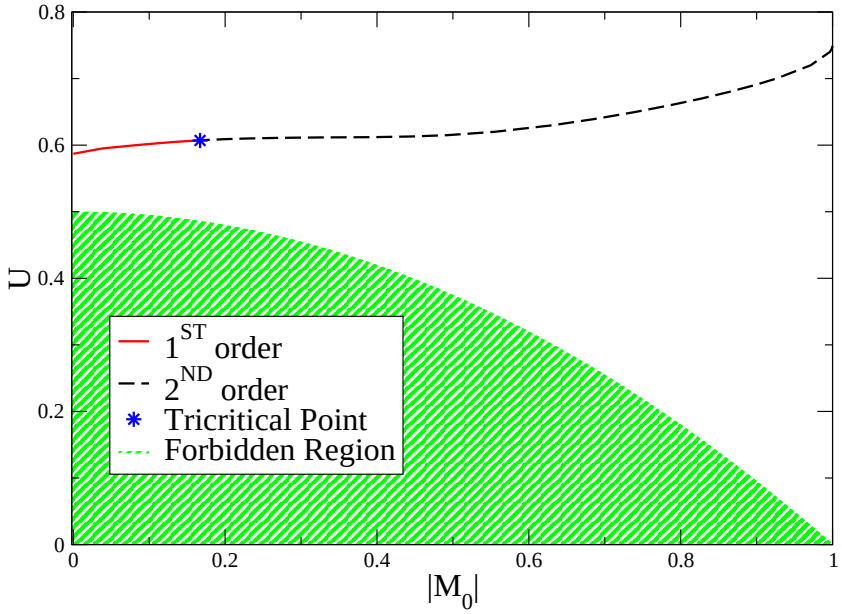

Figure 3.7: Theoretical phase diagram in the control parameter plane (M_0, U) for a rectangular water-bag initial profile. The dashed line stands for the second order phase transition, while its continuation as a full line refers to the first order phase transition. The full dot is the tricritical point. The green zone corresponds to forbidden domain of the parameter space.

sition, meaning that the magnetization is continuously modulated, from zero to positive values, when passing the curve from top to bottom. Conversely, the full line refers to a first order phase transition: Here, the magnetization experiences a sudden jump when crossing the critical value (M_0^c, U^c). First and second lines merge together in a tricritical point approximately located at $(M_0, U) = (0.2, 0.61)$. Such a rich out-of-equilibrium scenario results from a straightforward application of the Lynden-Bell theory and proves extremely accurate versus direct simulations based on the discrete formulation of Eq. (3.2). The existence of phase transition is in particular numerically confirmed. The values of the critical parameters (U^c, M_0^c) and the order transition are correctly predicted. More recent evidence on the adequacy of the Lynden-Bell scenario

for the HMF model are reported in Staniscia *et al.* [63] where the presence of re-entrance phases is demonstrates. Lynden-Bell theory constitutes indeed a powerful analytical tool which enables one to characterize the global properties of QSSs and unravel their unexpected richness. Having recognized the existence of at least two different classes of QSS points out the need of further clarifying the issue of their time duration. Is the scaling $N^{1.7}$ universal or, conversely, does it apply only under specific condition? In the following we settle down to further explore this important point.

3.4 On the lifetime of homogeneous and magnetized QSS: Different scalings, numerical simulations and kinetic theory

Let us start by reviewing the available results on the time duration of the QSS for the HMF model. As already mentioned in Section 3.1.2, Yamaguchi *et al.* reported in [17] that the lifetime of the QSS diverges as $N^{1.7}$ when increasing the system size. Their numerical simulations refer to initially homogeneous water-bag ($M_0 = 0$) and for a specific choice of the energy ($U_0 = 0.69$), which lies in the portion of the parameter space yielding to (almost) unmagnetized QSS ($M_{QSS} = 0$). Later on, Anteneodo *et al.* performed an independent campaign of simulations [64] initializing the system as a water-bag specifed by the conditions $M_0 = 1$, $U_0 = 0.69$, which admits the equilibrium values $M \approx 0.31$ and $T \approx 0.457$ for magnetization and temperature respectively.
When preparing the initial water-bag, Anteneodo *et al.* set $\theta_i = 0$ for $i = 1, ..., N$ and assume regularly valued momenta (instead of random ones as customarily done) with the addition of a small noise to allow for a statistical realization[4]. In Fig 3.8 the (average) temporal evolution of the temperature $T(t) = \sum_i \langle p_i^2 \rangle / N$ is plotted. Then, Anteneodo *et al.* rescaled the time axis by a factor $N^{1.7}$, clearly inspired to the the work of Yamaguchi *et al.*. Different curves nicely collapse onto each other, see Fig. 3.9, suggesting that the lifetime of the QSS at $M_0 = 1$ obeys to a scaling law identical to that associated to the $M_0 = 0$ case. Two comments are mandatory at this point. On the one hand working at $U = 0.69$ for $M_0 = 1$, one would expect to find a magnetized QSS, while Anteneodo data returns homogeneous configuration, as confirmed by visual inspection of Fig. 3.9. How can this observation reconcile with the existence of the transition line, as identified via the Lynden-Bell calculation? Also, having identified the same scaling for two extreme values of M_0 (resp. set to 0 and 1) and energy values respectively below and above the corresponding transition point, would naively suggest that the QSS lifetime is not sensitive to the initial water-bag characteristics.

[4]No specific information is provided in [64] on the strength of the superposed stochastic contribution. As we shall argue in the following we do believe that the noise is practically

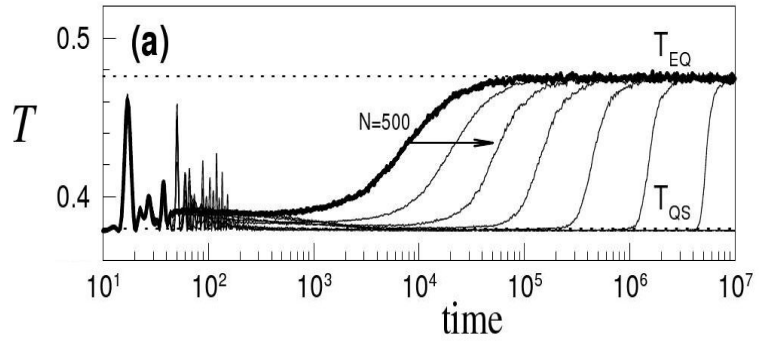

Figure 3.8: Average of time series of the temperature T for $U = 0.69$ and different values of the simulated particles N ($N = 500 \times 2^k$, with $k = 0, ..., 9$). Averages were taken over $2.56 \times 10^5/N$ realizations starting from a "isotropic" (regularly valued momenta) water-bag initial configuration at $t = 0$. Dotted lines correspond to temperatures at equilibrium, $T_{EQ} = 0.476$ and at QSS, $T_{QSS} = 0.38$ (this temperature corresponds to $M_{QSS} = 0$ according to the formula $U = \frac{T}{2} + \frac{1}{2}(1 - M^2)$). Figure is from Ref. [64].

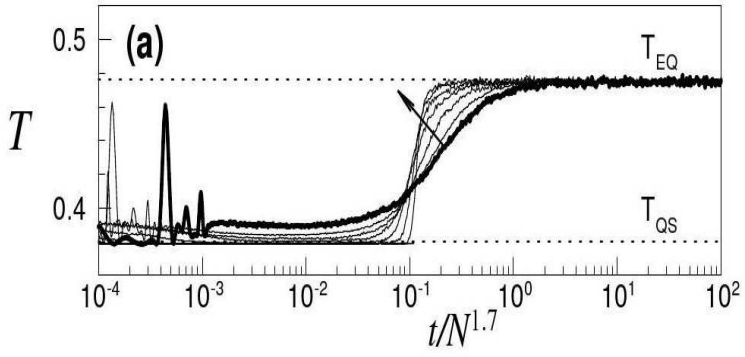

Figure 3.9: Averaged time series of temperature T as a function of $t/N^{1.7}$. Parameters are the same as in the caption of Fig. 3.8. The figure is taken from Ref. [64].

The whole picture is however far more complicate as revealed by an independent set of measurements performed by Rapisarda and collaborators [49]. In his work, Rapisarda assumed a water-bag initial condition, the particles position being $\theta_i = 0$ for all i, which corresponds to setting $M_0 = 1$. The energy is again $U = 0.69$, but, at odd with the procedure followed by Anteneodo, the velocities are randomly assigned with uniform probability. Surprisingly, the QSS lifetime is now reported to increase linearly with the system size N, see Fig. 3.10. When it comes to the observed value of M_{QSS}, refined analysis by Rapisarda himself [65] indicates that inhomogeneous configuration prevails, in agreement with the Lynden-Bell prediction. Even more astonishingly no comment is found in the literature concerning the apparent discrepency of the two studies mentioned above. This puzzle finds its solution, when considering the work of Campa *et al.* [66]. In this paper the authors focus on different classes of initial conditions, all relative to energy density $U = 0.69$. In particular they numerically show that when starting from particles equally spaced both in momentum and positions, the system naturally evolves towards a homogeneous QSS configuration (even if the system is initiated in a region that Lynden-Bell theory baptises associated to inhomogeneous QSS). Conversely, if the particles are initially randomly distributed then the Lynden-Bell partition into magnetized and demagnetized QSS is respected. Antenodo simulations falls in the former class (assuming the stochastic perturbation weak enough) and the system rapidly moves towards a homogeneous QSS, similar to that faced by Yamaguchi when dealing with the choice $M_0 = 0$ and $U = 0.69$. In this respect, following the intriguing dynamical mechanisms identified by Campa, which still calls for a sound theoretical interpretation, it is quite natural to expect an analogous dependence with reference to the observed scaling properties. Completely different is the situation explored by Rapisarda, since the initial condition chosen in [49] (random distribution) returns preferentially magnetized QSS.
In conclusion looking with a critical eye to the results published in the literature one can argue that the QSS characteristics are non trivially affected by the initial distribution of the particles. *The associated duration time gets equally influenced.*

Motivated by this complex, and apparently controversial scenario, we hypothesise that two main scaling exists for the QSS lifetime[5]: Above the Lynden-Bell transition line we conjecture a N^α scaling law, α closely resembling the value 1.7 detected by Yamaguchi and Anteneodo respectively. Conversely, below the Lynden-Bell transition line, we predict a N divergence for the QSS lifetime, when increasing the number of simulated particles.
To shed light onto this issue and eventually verify the correctness of our inter-

too small to induce any sensible modification from the equally spaced configuration.

[5]In our study we consider the particles to be randomly distributed within the initial water-bag domain.

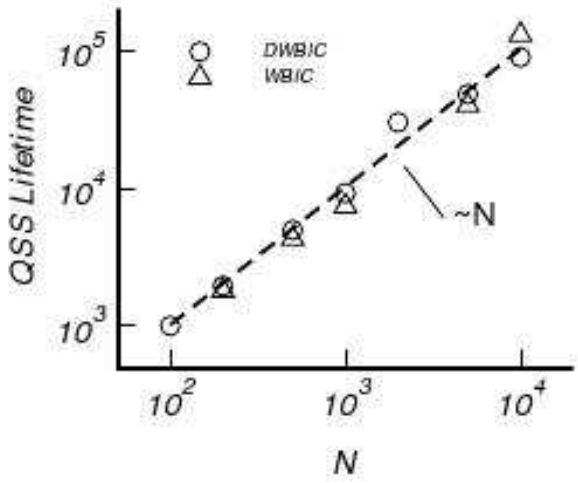

Figure 3.10: Log-log of the QSS lifetime is reported as a function of the size N, for $U = 0.69$ and $M_0 = 1$. The lifetime diverges linerly with N. The figure is taken from Ref. [66].

pretative picture we turn to numerical simulations. As we shall be discussing in the following we also argue that the exponent α is indeed 1.5, as suggested by a lengthy generalization of the kinetic argument proposed in Section 3.2.1. We have numerically integrated the equations of motion (3.2), by using symplectic 4th-order integrators, the McLaghan-Atela's algorithms [67]. The timestep $dt = 0.7$ was chosen as a trade-off between a good energy conservation (with a relative accuracy $|\triangle E/E| \sim 10^{-5}$) and the possibility to perform long enough simulations, for relatively large systems, in a reasonable amount of computation time.
We consider a water-bag initial condition (3.17) where the spatial coordinates θ_i randomly populate the interval $[-\triangle\theta, \triangle\theta[$, with a uniform distribution. Analogoulsy, the momenta are assigned into the the interval $[-\triangle p, \triangle p[$. The energy follows from $U = \frac{(\triangle p)^2}{6} + \frac{1-(M_0)^2}{2}$.

We are interested in measuring the duration of the QSS as the system size is changed. Consider first $U = 0.69$ for three different values of M_0 respectively set to 0, 0.2, 0.7. All cases fall above the Lynden-Bell transition line and are hence expected to yield to a demagnetized QSS, for which the scaling N^α, $\alpha \simeq 1.7$ applies. In Fig. (3.11) the temporal evolution of the magnetization versus the rescaled time, $t/N^{1.7}$, for $M_0 = 0$ is plotted. Distinct curves relative to different choices of N collapse onto a universal profile, so pointing to the correctness of the proposed scaling. To further reinforce our conclusion, we also extract a direct estimate of the equilibration time following the fitting scheme introduced by Yamaguchi *et al.* [17] and revisited above, see Eq. (3.19). In Fig. 3.12 the best fitted value of $b(N)$ is plotted versus $\log_{10}(N)$. The three panels refer to the values of M_0 here considered. The superimposed

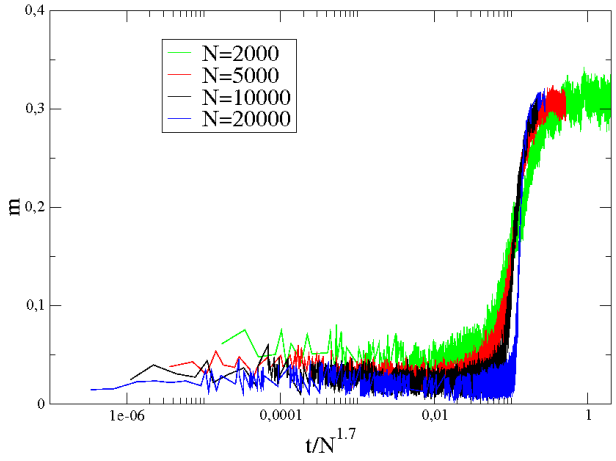

Figure 3.11: The magnetization for different values of N versus the rescaled time $t/N^1.7$ is plotted. Here $N = 2 \cdot 10^3(8)$, $5 \cdot 10^3(8)$, $10^4(4)$ and $2 \cdot 10^4(4)$ from left to right (the number in between brackets stands for the number of samples) are reported. Simulations refer to $M_0 = 0$ and $U = 0.69$.

dotted line correspond to a power law scaling with $\alpha = 1.7$ as suggested by Yamaguchi/Anteneodo investigations. The dashed line is instead calculated for $\alpha = 1.5$, and, in our opinion, it also interpolates correctly the data. We shall return on this important point in the following.

To complete our analysis we here report results of the simulations relative to the same choice of M_0 but different U. In particular we set $U = 0.58$, i.e. a value that fall below the Lynden-Bell transition line for all selected values of M_0. The associated QSS are hence expected to be of the magnetized type. Results of the simulation are presented in Fig. 3.13: Here the time is rescaled by a factor N, and the curves shows a clear tendence to accumulate over a universal profile, regardless of the specific N value to which they refer. This finding is in agreement with Rapisarda's simulation relative to the specific case $M_0 = 1$ and more generally suggest that the lifetime of magnetized QSS grows linearly with the system size.

In conclusion, and based on the above numerical evidence, we suggest that the QSS lifetime obeys to two distinct scaling depending on the initial parameters of the water-bag. The different scalings correlate with the out-of-equilibrium transition line as detected via the Lynden-Bell theory of violent relaxation. The suggested scenario is summarised in Fig. 3.14.

Let us now concentrate on the possible origin of the different scaling. We shall be interested in finding a justification for the observed behaviours, which, we believe, should ultimately stem from kinetic theory. Consider the Klimontovich equation (3.33) and imagine to develop around a homogeneous solution, as it is the case (after a fast transient) when working above the transition line

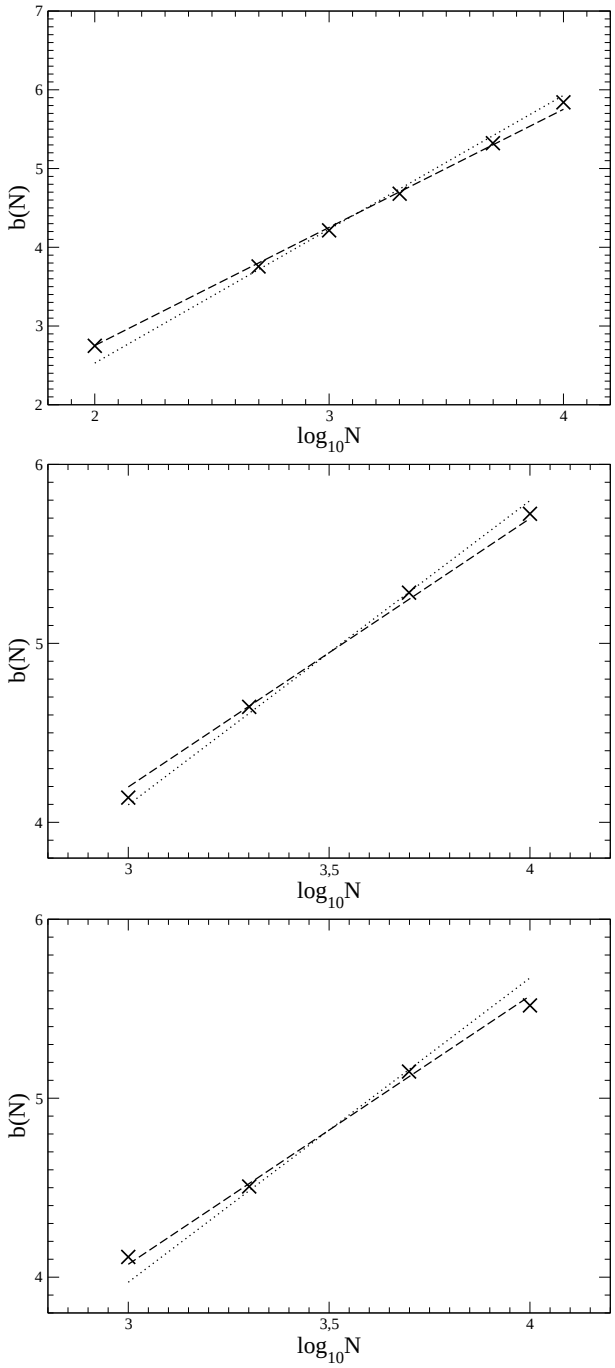

Figure 3.12: Logarithmic timescale $b(N)$ as a function of $\log_{10} N$ for $U = 0.69$ and three different choices of M_0. From top to the bottom, $M_0 = 0$, 0.2, 0.7. The dotted and the dashed lines represent the laws $\tau_{QSS} = 10^{b(N)} \sim N^{1.7}$ and $\tau_{QSS} = 10^{b(N)} \sim N^{1.5}$ respectively.

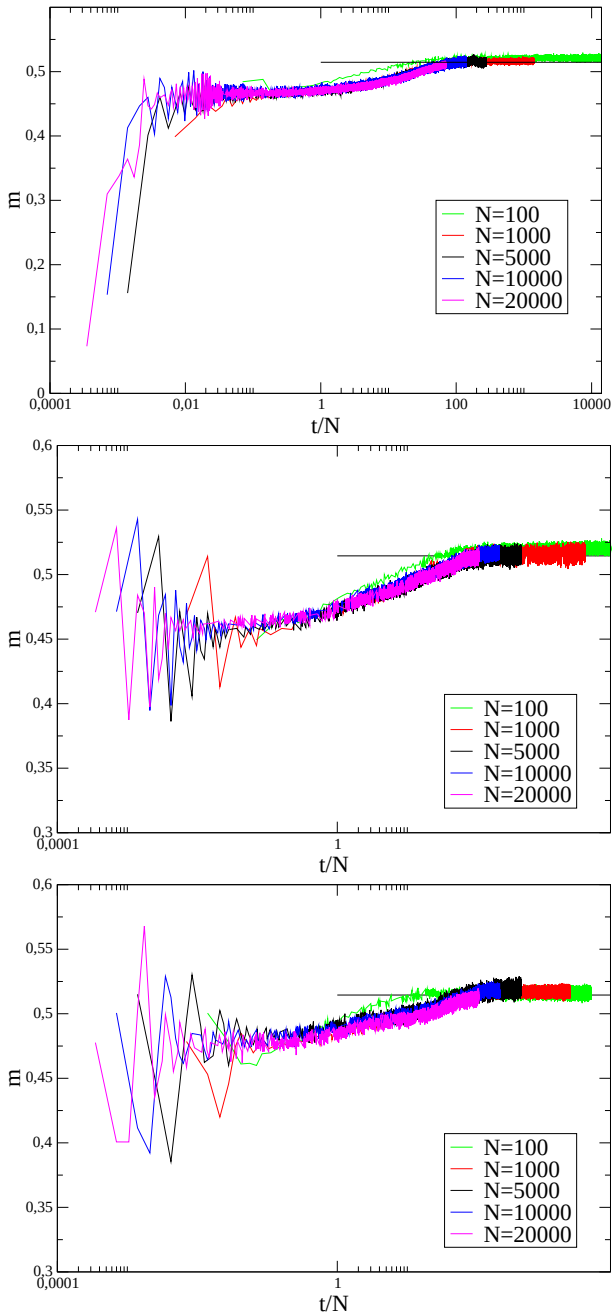

Figure 3.13: The magnetization for different values of N versus the rescaled time t/N is plotted. Here $N = 10^2(10^3)$, $10^3(10^2)$, $5 \cdot 10^3(8)$, $10^4(8)$ and $2 \cdot 10^4(4)$ from left to right (the number between brackets corresponding to the number of samples). Data are referred to $U = 0.58$ and $M_0 = 0, 0.2, 0.7$.

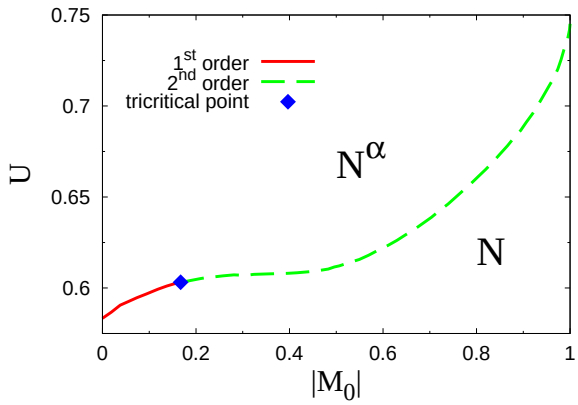

Figure 3.14: Two scaling laws for the QSS lifetime as a function of the number of simulated particles are detected: Above the transition line as predicted by Lynden-Bell theory of violent relaxation, the QSS lasts for a time that diverges as a power law of the system size, N^{α}. $\alpha = 1.7$ fits the data, but the alternative scaling $\alpha = 1.5$ results equally appropriate. Below the transition line, when magnetized QSS are to be expected, one observes a linear dependence of the QSS duration versus N, the size of the system.

of Fig. 3.14. Then, under this condition, it can be shown [58, 12, 61, 62] that the first order correction to the Vlasov equation, i.e. the collisional term:

$$\frac{1}{N}\langle\frac{\partial\delta v_0}{\partial\theta}\frac{\partial\delta f_0}{\partial p}\rangle \tag{3.46}$$

(where the zero index indicates the zeroth order of approximation) vanishes. Generalizing the perturbative calculation so to account for higher order corrections, one can show that the next-to-leading correction to the mean-field Vlasov scenario scales as $1/N^{1.5}$ [68]. This in turn suggests that the system migrates from the ideal Vlasov setting on time scales which get longer and longer when increasing the system size and in particular diverging as $N^{1.5}$, in quantitative agreement with the results of our simulations.

In the opposite regime, when the QSS is magnetized, and so intrinsically non homogeneous, one cannot drop the collisional term (3.46), this later is in principle present and contributes with a non-zero forcing which drives the relaxation to equilibrium. The equilibration time is hence expected to diverge linearly with N, as seen in our simulations.

Chapter 4

Analytical results on the magnetization of the Hamiltonian Mean Field model

As discussed in the previous chapter, the Lynden-Bell theory returns a rather accurate description of the QSS phenomenology in the HMF model. This is an approximate statistical based approach which builds on the underlying Vlasov picture, formally recovered in the limit for diverging system sizes. Alternatively, one could resort to a dynamical description which should however originates from the relevant Vlasov setting.

Motivated by this observation, we here focus both on the HMF violent relaxation process and the subsequent QSS regime within the associated Vlasov scenario. To anticipate our findings, we shall exploit an Hamiltonian formalism to derive analytical expressions for the global magnetization as function of time. Recall that the magnetization is a macroscopic observable which is directly influenced by the microscopic, single particle trajectory. It is in general particularly cumbersome to bridge the gap between the microscopic realm of the many-body interacting constituents and the macroscopic world of collective dynamics. A recipe is here provided and succesfully tested versus direct numerical simulation. We shall be in particular concerned with inspecting two opposite dynamical regimes, respectively high and low energy ones.

As an additional point, and still exploiting the formalism being here put forward, we shall analytically characterize the out-of-equilibrium phase transition separating homogeneous and non-homogeneous QSS, as previosuly discussed. This is achieved by monitoring the initial relaxation of the magnetization, as a function of reference key parameters, and targeting the first peak value

as the control quantity. The parameter space is hence partitioned into two regions, depending on the magnetization amount, a finding which positively correlate with direct numerics. The proposed method is rather flexible and in principle applies to other settings, beyond the class of water-bag initial conditions here adopted. We shall hence dispose of an *ad hoc* strategy to predict out-of-equilibrium phase transitions, with reference to an ample spectrum of experimental settings, and extending over previous investigations [25].

In the next section, we start by dicussing the analytical foundation of the so-called Bracket Method, making reference to the specific HMF case study.

4.1 Model and methods

4.1.1 Lie-Poisson structure of the Vlasov equation

We start by recalling the HMF Hamiltonian:

$$H = \sum_{i=1}^{N} \left[\frac{p_i^2}{2} + \frac{1}{2N} \sum_{j=1}^{N} [1 - \cos(\theta_i - \theta_j)] \right], \tag{4.1}$$

where (θ_i, p_i) are canonically conjugate variables which means that the Poisson bracket giving the dynamics (Hamilton's equations) is given by

$$\{F, G\} = \sum_{i=1}^{N} \left(\frac{\partial F}{\partial p_i} \frac{\partial G}{\partial \theta_i} - \frac{\partial F}{\partial \theta_i} \frac{\partial G}{\partial p_i} \right).$$

In the continuous limit, we know that we can consider an Eulerian description of the system, which gives the dynamical evolution of the distribution of particles $f(\theta, p; t)$ in phase space via the following Vlasov equation:

$$\frac{\partial f}{\partial t} = -p \frac{\partial f}{\partial \theta} + \frac{dV[f]}{d\theta} \frac{\partial f}{\partial p}, \tag{4.2}$$

where $V[f](\theta) = 1 - M_x[f] \cos\theta - M_y[f] \sin\theta$. The magnetization $M[f] = M_x + iM_y$ is defined as

$$M[f] = \iint f e^{i\theta} d\theta dp, \tag{4.3}$$

where the integrals are taken over $[-\pi, \pi] \times \mathbb{R}$. Equation (4.2) can be cast into a Hamiltonian form where the (infinite dimensional) phase space is composed of the functions $f(\theta, p)$ of $]-\pi, \pi] \times \mathbb{R}$. The Hamiltonian is given by

$$H[f] = \iint f \frac{p^2}{2} d\theta dp - \frac{M_x[f]^2 + M_y[f]^2 - 1}{2}, \tag{4.4}$$

and the associated Lie-Poisson bracket by

$$\{F, G\} = \iint f \left(\frac{\partial}{\partial p} \frac{\delta F}{\delta f} \frac{\partial}{\partial \theta} \frac{\delta G}{\delta f} - \frac{\partial}{\partial \theta} \frac{\delta F}{\delta f} \frac{\partial}{\partial p} \frac{\delta G}{\delta f} \right) d\theta dp, \tag{4.5}$$

for F and G two observables (that is, functionals of f). The functional derivatives $\delta F/\delta f$ are computed following the expansion :

$$F[f+\varphi] - F[f] = \iint \frac{\delta F}{\delta f}\varphi d\theta dp + O(\varphi^2).$$

The Poisson bracket (4.5) satisfies several properties: bilinearity, Leibniz rule and Jacobi identity [69, 70]. Its Casimir invariants are given by

$$C[f] = \iint c(f) d\theta dp,$$

where $c(f)$ is any function of $f(\theta, p)$. In particular, the total distribution $\iint f d\theta dp$ is one of such Casimir invariants and hence is conserved by the flow, as we already discussed. The evolution of any observable $F[f]$ is then given by

$$\dot{F} = \{H, F\}. \tag{4.6}$$

For instance, for $F[f] = f(\theta, p)$, we recover Eq. (4.2). An interesting observable is the magnetization $M[f]$ given by Eq. (4.3), which quantifies the degree of spatial aggregation of the particles. Below the transition line (see Fig. 3.7), the magnetization relaxes to an out-of-equilibrium *plateau*, around which it fluctuates (see Fig. 4.1). In this case, particles are trapped into a large resonance resulting from the finite magnetization amount (magnetized state see upper panel of Fig. 4.2). At energies above the critical value, the magnetization is almost zero (see Fig. 4.1). This is the so called homogeneous phase (lower panel of Fig. 4.2). We shall return on this important point in the following, when providing a quantitative interpretation of the switch between these two regimes, and making contact with the stroboscopic single particle analysis of Bachelard *et al.* [71].

The dynamics given by Eq. (4.6) is deduced from the linear operator $\mathcal{H}$. From the evaluation of the functional derivative of H with respect to f

$$\frac{\delta H}{\delta f} = \frac{p^2}{2} - M_x[f]\cos\theta - M_y[f]\sin\theta,$$

we get the expression of $\mathcal{H}$:

$$\begin{aligned} \mathcal{H} &\equiv \{H, .\} \\ &= \iint d\theta dp f \left(p\frac{\partial}{\partial\theta} + \frac{Me^{-i\theta} - M^* e^{i\theta}}{2i}\frac{\partial}{\partial p}\right)\frac{\delta}{\delta f}. \end{aligned} \tag{4.7}$$

In the algebraic computations that follows, we make an explicit use of the linearity of $\mathcal{H}$ and Leibniz rule:

$$\begin{aligned} \mathcal{H}(F + \alpha G) &= \mathcal{H}F + \alpha\mathcal{H}G, \\ \mathcal{H}(FG) &= F\mathcal{H}G + (\mathcal{H}F)G. \end{aligned}$$

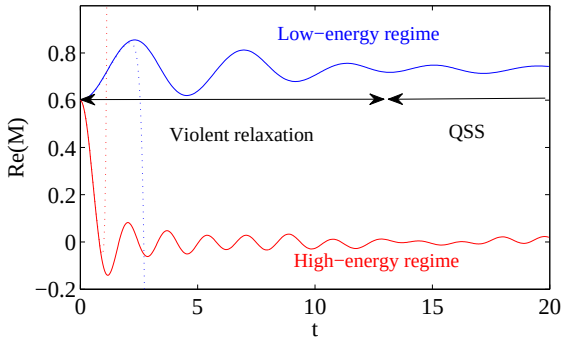

Figure 4.1: Real part of the magnetization given by Eq. (4.3) as a function of time obtained by integrating the dynamics given by Eq. (4.6) for $M_0 = 0.6$. The system reaches either a finite-magnetization for low energies ($U = 0.4$, in blue), or a low-magnetization for high energies ($U = 3$, in red). The plain lines refer to simulations described in Section 3.4 with $h = 0.01$ and for $N = 10000$, while the dotted lines come from the predictions given by Eq. (4.10) for $k_0 = 20$.

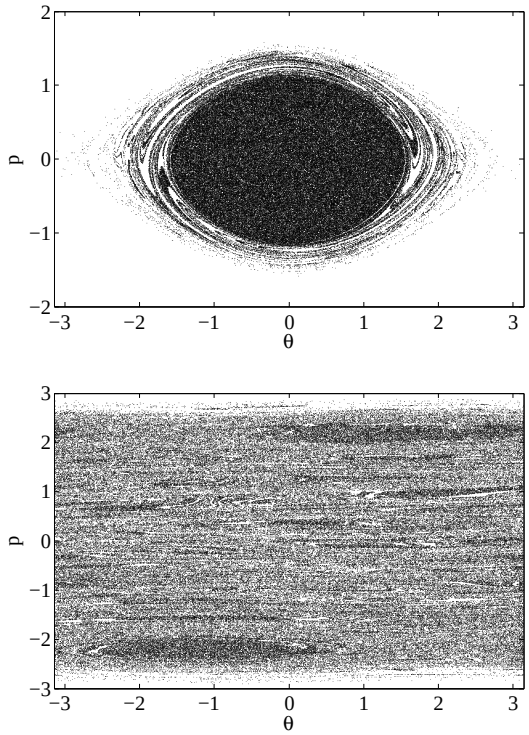

Figure 4.2: Phase space portrait of the system (4.1) once saturation has been reached for $M_0 = 0.6$: The low energy regime ($U = 0.5$, upper panel) is characterized by one large cluster of particles, whereas for higher energies ($U = 1.7$, lower panel), phase space is quite homogeneous, except for two clusters $at \pm 2.2$ (i.e. moving in opposite directions).

4.1.2 Bracket method

The Bracket Method is based on the $\mathcal{H}$ operator, that contains the equations of motion of the system and dynamical evolution of every observable:

$$F[f](t) = e^{t\mathcal{H}} F[f_0], \tag{4.8}$$

where f_0 is the initial distribution. The operator $e^{t\mathcal{H}}$ can be explicitly calculated only in a few cases but it is possile to use the natural expansion of this operator that reads as

$$e^{t\mathcal{H}} = \sum_{k=0}^{\infty} \frac{t^k}{k!} \mathcal{H}^k \longrightarrow F[f](t) = \sum_{k=0}^{\infty} \frac{t^k}{k!} \mathcal{H}^k F[f_0]. \tag{4.9}$$

We note here that this method presents some big advantages:

- It is possible to extend the k_0 expansion to higher order only applying the operator $\mathcal{H}$ more times, the coefficients of the series $\mathcal{H}^k F$ are obtained recursively by applying $\mathcal{H}$ on the previous term $\mathcal{H}^{k-1} F$. One can arrive at every level of precision without modifing the model at all.
- The method has an explicit dependence on the initial conditions.
- The procedure is valid for every initial conditions and this features is a useful tool to investigate the out-of-quilibrium violent relaxation of the system.

Here we compute a finite number of terms in this series in order to obtain a Taylor expansion for the solution of the dynamics of F:

$$F[f](t) \approx \sum_{k=0}^{k_0} \frac{t^k}{k!} \mathcal{H}^k F[f_0], \tag{4.10}$$

where k_0 is the truncation parameter. Of course, this approximation is accurate up to some time t depending on k_0. A convergence over longer times is expected for increasing k_0.
At this point we need to derive the operator $\mathcal{H}^n$. Since more accurate predictions need larger n we have to implement a numerical method to make the calculations as fast as possible even with a high-order expansion.
Since the evaluation of the $\mathcal{H}^n$ operator involves derivatives, functional derivatives and integrals we need a sort of trick to skip the problem.
We consider the subspace of functions composed by sums and products of the following elements (which are also functionals of f):

$$b_{n,m}[f] = \iint d\theta dp f e^{in\theta} p^m,$$

where $(n,m) \in \mathbb{Z} \times \mathbb{N}$. We notice that the main observables of the system such as the n-th order magnetization $M_n = \iint e^{in\theta} f d\theta dp$ or the momenta $P_m = \iint p^m f d\theta dp$ of the system belong to this family. This family is stable by the action of $\mathcal{H}$ given by

$$\mathcal{H} b_{n,m} = in b_{n,m+1} + \frac{m}{2i}(b_{1,0} b_{n-1,m-1} - b_{-1,0} b_{n+1,m-1}). \tag{4.11}$$

We notice that only positive values of m are involved in the iterations of the recursion relation since the second term is proportional to m. Taking into account the linearity and the Leibniz rule for $\mathcal{H}$ mentioned in the previous section, the derivation of the short-time evolution (4.10) of a given observable F is computed algebraically as a sum of products of elements $b_{n,m}$. For instance, the magnetization is given by $M = b_{1,0}$ and its first order evolution is obtained from Eq. (4.11):

$$\begin{aligned} M(t) &= b_{1,0}[f_0] + t\mathcal{H} b_{1,0}[f_0] + \frac{t^2}{2}\mathcal{H}^2 b_{1,0}[f_0] + O(t^3), \\ &= b_{1,0}[f_0] + it b_{1,1}[f_0] + i\frac{t^2}{2}\mathcal{H} b_{1,1}[f_0] + O(t^3), \\ &= b_{1,0}[f_0] + it b_{1,1}[f_0] \\ &\quad + \frac{t^2}{2}\left(-b_{1,2}[f_0] + \frac{1}{2}(b_{1,0}[f_0] - b_{-1,0}[f_0] b_{2,0}[f_0])\right) \\ &\quad + O(t^3). \end{aligned}$$

Of course, a satisfying approximation of the time evolution of any observable needs a large number of terms in the expansion (4.10). At a given time t, the number of terms necessary to obtain a reasonably good approximation of the dynamics depends on the initial distribution f_0 as it is shown in Fig. 4.1 where, at low energies, the accuracy extends to longer times than at high energies. In addition, we need to specify the initial distribution which will be used to compute $b_{n,m}(0)$ necessary to complete the computation of the approximate evolution. In the following sections, we use a water-bag distribution as initial condition.

4.1.3 Initial conditions

Also in this case and to make contact with the previous investigations, we use a water-bag initial condition. Let us recall that the initial distribution $f_0(\theta, p)$ is equal to $1/(4\Delta\theta\Delta p)$ if $(\theta, p) \in [-\Delta\theta, \Delta\theta[\times[-\Delta p, \Delta p[$ and zero otherwise. The values of $b_{n,m}$ at $t = 0$ can be computed explicitly in this case and read

$$b_{n,m}(0) = \frac{(\Delta p)^{m+1} - (-\Delta p)^{m+1}}{2(m+1)\Delta p} \mathrm{sinc}(n\Delta\theta),$$

where $\mathrm{sinc}(\cdot) = \sin(\cdot)/(\cdot)$. In particular, we notice that $b_{n,m}(0) = 0$ for m odd. The water-bag is characterized by two parameters $(\Delta\theta, \Delta p)$. Instead we

consider the initial magnetization M_0 and the energy U to label the initial conditions:

$$M_0 \equiv b_{1,0}(0) = \mathrm{sinc}(\Delta\theta),$$
$$U \equiv \frac{1}{2}\left(b_{0,2} - b_{1,0}b_{-1,0} + 1\right) = \frac{\Delta p^2}{6} - \frac{M_0^2 - 1}{2}.$$

In the following, we investigate the high energy $U \gg 1$ and low energy $U \ll 1$ limits for the initial distribution.

4.2 Analytical results

The first terms of the expansion for the magnetization $M(t)$ given by Eq. (4.10) (for a water-bag initial distribution) are listed in Tab. 4.1 up to sixth order in time. We notice that the number of terms in the expansion increases exponentially, making such expressions difficult to handle in practice. In Fig. 4.1, we notice that even with $k_0 = 20$ which involves approximately one thousand terms, a good agreement is observed only up to $t = 2$. In Fig. 4.3, the algebraic expressions for the magnetization obtained by Eq. (4.10) are plotted at different orders. Other than the initial regime, if one is interested in the intermediate regimes, the only hope is to find the governing rules behind this algebraic computations in order to draw some conclusions. This is the case for the low and high energy limits where the leading terms of the expansion can be extracted to all orders. These simplifications allow us to derive some dynamical properties of the system.

Table 4.1: First terms in the expansion of the magnetization $M(t)$ given by Eq. (4.10) for the water-bag initial distribution.

$t^2/2!$	Δp^0	$(1 - \mathrm{sinc}(2\Delta\theta))M_0/2$
	Δp^2	$-M_0/3$
$t^4/4!$	Δp^0	$(1 - 2\,\mathrm{sinc}(2\Delta\theta) + \mathrm{sinc}(2\Delta\theta)^2 - 4M_0^2 + 4M_0\,\mathrm{sinc}(3\Delta\theta))M_0/4$
	Δp^2	$-2\left(3\,\mathrm{sinc}(2\Delta\theta) + 1\right)M_0/3$
	Δp^4	$M_0/5$
$t^6/6!$	Δp^0	$(1 + 3\,\mathrm{sinc}(2\Delta\theta) + 64M_0^2 + 3\,\mathrm{sinc}(2\Delta\theta)^2 + 26M_0\,\mathrm{sinc}(3\Delta\theta)$ $+98M_0^2\,\mathrm{sinc}(2\Delta\theta) - \mathrm{sinc}(2\Delta\theta)^3 - 34M_0^2\,\mathrm{sinc}(4\Delta\theta)$ $-26M_0\,\mathrm{sinc}(2\Delta\theta)\,\mathrm{sinc}(3\Delta\theta))M_0/8$
	Δp^2	$(-202\,\mathrm{sinc}(2\Delta\theta)M_0 - 51\,\mathrm{sinc}(2\Delta\theta)^2 + 58\,\mathrm{sinc}(2\Delta\theta) + 138M_0^2$ $-7)M_0/12$
	Δp^4	$(-239\,\mathrm{sinc}(2\Delta\theta) + 23)\,M_0/30$
	Δp^6	$-M_0/7$

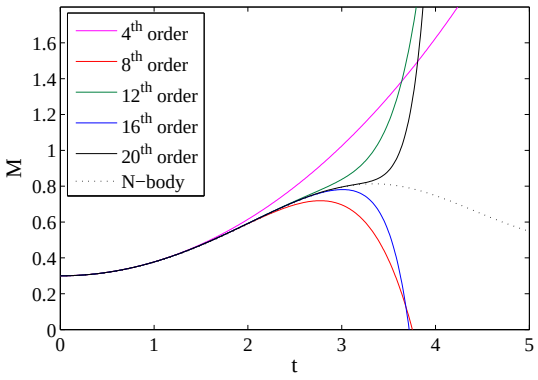

Figure 4.3: Magnetization $M(t)$ versus time for $M_0 = 0.2$ and $U = 0.6$. Dotted black curve refers to simulations (see Fig. 4.1). Solid curves represents the algebraic expansions at various orders, from the 4th to the 20th order.

4.2.1 High-energy limit

First we consider the high energy limit, which corresponds to $\Delta p \gg 1$ in the initial water-bag. In this regime, since the kinetic term is dominant, the dynamics is driven by the reduced Liouville operator, which takes into account only the kinetic term

$$\mathcal{H}_{HE} = \iint d\theta dp f p \frac{\partial}{\partial \theta} \frac{\delta}{\delta f}. \tag{4.12}$$

From Eq. (4.11), the successive actions of $\mathcal{H}$ on $b_{n,m}$ is given by

$$\mathcal{H}^k b_{n,m} = (in)^k b_{n,m+k}.$$

For the water-bag initial distribution, it is straightforward to deduce the evolution of the magnetization of order n:

$$M_n(t) = M_n(0)\mathrm{sinc}(n\Delta p t). \tag{4.13}$$

The magnetization envelop exhibits a slow decay (as $1/(\Delta p t)$) towards the asymptotic (equilibrium) state $M = 0$ (see Fig. 4.4).

The profile obtained from numerical simulations is correctly interpolated over a finite time window by Eq. (4.13). As U is increased, the agreement gets better, even if deviations from Eq. (4.13) are observed at later times. Such a discrepancy is due to the cumulative effects of the neglected contributions in Δp (see Tab. 4.1).

It is known [71] that, for large values of the energy, and for any given initial magnetization, two large resonances spontaneously develop and effectively divide the available phase space into independent regions. Such resonances move in opposite directions, over the unit circle. Their velocity p_r is identical in modulus and tends to grow as the energy is increased. This is indeed a

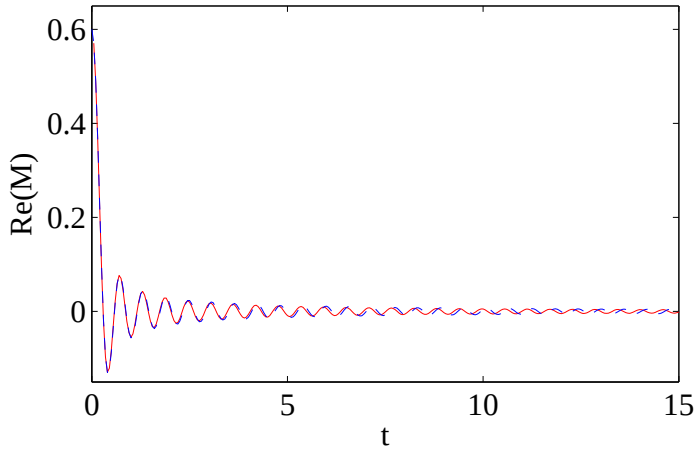

Figure 4.4: Real part of the magnetization $M(t)$ versus time for $M_0 = 0.6$ and $U = 20$. The solid red line refers to direct simulations (see Fig. 4.1), while the dashed blue one stands for the approximate solution (4.13).

recent observation put reported in [71] which points to a different, dynamical interpretation of the out-of-equilibrium phase transition first observed in [25]. It was in fact argued by Bachelard and collaborators that tori can form in phase space as a result of a self-consistent interaction in the thermodynamic limit. While for a small number N of degrees of freedom the single particle motion is largely erratic, the trajectories become more and more regular as $N \to \infty$. These trajectories arise from a low-dimensional time dependent effective Hamiltonian. Working in this framework, two different regimes can be identified, as shown in [71]: For large enough energy values, a bicluster QSS arises, which is then gradually transformed into a monocluster QSS when reducing the energy amount. To shed light on this issue, Bachelard *et al.* proceeded as follows: For fixed M_0 and N, they gradually increase the energy U and reconstructed the stroboscopic motion of single particle resorting to a technique inspired to the Poincaré sections. More specifically, they considered the time average $\bar{M}$ (after a transient) and record the positions and momenta of a few selected particles $(\theta_i,\ p_i)$ when $M(t) = \bar{M}$ and $dM/dt > 0$ (since M typically shows an oscillatory behavior). The resulting stroboscopic sections are displayed in Fig. 4.5, showing the two dynamical regimes referenced to above. The recorded sections are analyzed by identifying the number of resonances and measuring the associated width and position (both calculated in the p direction). Results for $M_0 = 0.6$ are presented in [71] and here reproduced in the lower panel of Fig. 4.6: The shaded region, bounded by the dashed lines, quantifies the width of the resonances. As anticipated, one can recognize the typical signature of a bifurcation pattern. Repeating the above analysis for different values of the initial magnetization M_0, allows us to draw a bifurca-

tion line in the parameter space (M_0, U). In the upper panel of Fig. 4.6 this bifurcation line (full) is compared to Lynden-Bell phase transition (dashed) lines [25], returning a certain degree of similarity.

In the high energy regime, where the particles organizes in the two resonances, the magnetization $M(t)$ is hence mostly influenced by the instantaneous positions of the resonances. A snapshot of the positions of the particles obtained using N-body simulations is depicted in Fig. 4.2 (lower panel). It reveals the two resonances moving in opposite directions (with velocity p_r). The maxima of $M(t)$ are obtained when the two resonances are aligned since the bunching of particles is maximum in this case. During two successive maxima of $M(t)$ each cluster travels on a segment of length 2π in θ, which takes a time $2\pi/p_r$. On the other hand, according to Eq. (4.13), two successive bumps in the magnetization are separated by a time interval $2\pi/\Delta p$. This leads to

$$p_r = \Delta p = \sqrt{6\left(U - \frac{1 - M_0^2}{2}\right)}, \tag{4.14}$$

which applies in the high-energy limit. The above prediction is compared with N-body simulations in Fig. (4.7): The velocity (and corresponding width) of the resonances is plotted for different energies U (circles). The solid line refers to the analytical expression (4.14). We notice a very good agreement between the numerics and the prediction (4.14). As expected, as U decreases, some discrepancy is observed since the system approaches the phase transition.

The above conclusion and in particular Eq. (4.13) can be also recovered using the following argument: In the high energy limit, the particles move essentially freely. The potential energy accommodates for just a small fraction of the total energy. Under this hypothesis, the individual phase θ evolves as:

$$\theta(t) = \theta_0 + p_0 t$$

where the index 0 refers to the initial position of a single particle. From the definition of the magnetization, once a change of variables has been applied from (θ, p) to (θ_0, p_0), we obtain:

$$M_n(t) \approx \iint e^{in(\theta_0 + p_0 t)} f(\theta_0, p_0) d\theta_0 dp_0,$$

and Eq. (4.13) is recovered.

The next step is to incorporate the additional contributions, so far neglected. In particular, we focus our attention on the terms $t^{2n}\Delta p^{2n-2}$ in Tab. 4.1. For $\Delta\theta \approx \pi$ (i.e. $M_0 \ll 1$), the dominant term is $-M_0\Delta p^2 t^4/36$ since all the other terms are of higher order in M_0. This latter can be seen as originated from a modification of Eq. (4.13) where a constant factor c is being introduced as:

$$M(t) = M_0 \mathrm{sinc}(t\sqrt{\Delta p^2 - c}). \tag{4.15}$$

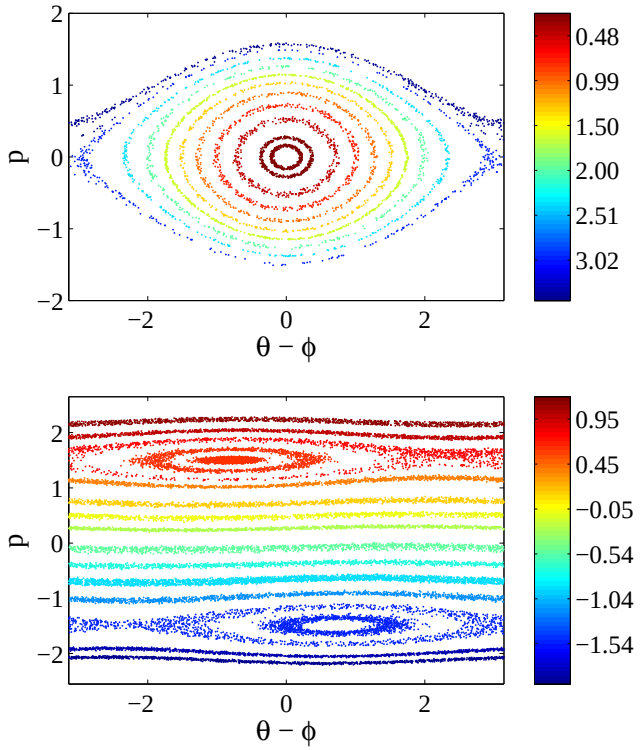

Figure 4.5: Poincaré sections of a few selected particles relative to $N = 2 \times 10^5$ in the QSS regime for two different water-bag initial conditions : $(M_0, U) = (0.6, 0.54)$ (upper panel) and $(M_0, U) = (0.6, 0.88)$ (lower panel). The stroboscopic analysis enbales us to visualize the presence of two distinc dynamical regimes: The single cluster (upper panel), which gives a non-zero magnetization QSS ($M_{QSS} \approx 0.5$), and the bicluster regime (lower panel). In this latter case the presence of a large set of rotational tori implies a substantially lower magnetization level, whereas the librational tori around the two clusters are responsible for the residual magnetization. The color code corresponds to the values of the action variable associated with individual particles. Figure taken from Ref. [71].

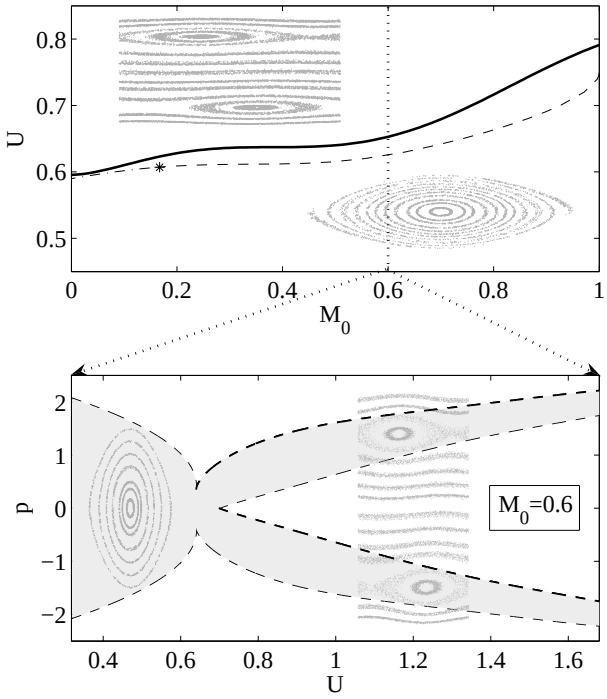

Figure 4.6: Upper panel: Phase diagram in the control parameter plane (M_0, U) of the out-of-equilibrium phase transition of the HMF model from a magnetized to the (almost) demagnetized phase. The solid curve pinpoints the position of the bifurcation from the monocluster to the bicluster QSS. The dashed line stands for the theoretical prediction based on Lynden-Bell's violent relaxation theory. The star refers to the tricritical point separating first from second order phase transitions. Lower panel: The bifurcation is monitored as function of U, for $M_0 = 0.6$. The grey zones refer to the width of the resonances. Figure taken from Ref. [71].

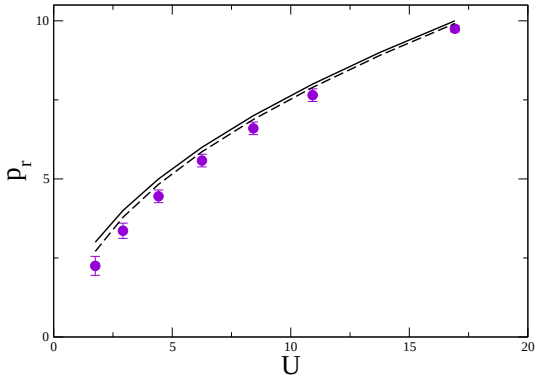

Figure 4.7: The velocity of the resonances (in the high energy regime) as a function of the energy U for $M_0 = 0.7$. The circles refer to the velocities obtained numerically using N-body simulations (see Fig. 4.1). The vertical bars delimit the width of the resonances in the p-direction. The solid line is given by Eq. (4.14), and the dashed line by Eq. (4.15).

The coefficient of $\Delta p^4 t^4$ of Eq. (4.13) is replaced by $\Delta p^4 t^4 - 2c\Delta p^2 t^4$. Therefore $c = 5/3$ matches the dominant term $-M_0 \Delta p^2 t^4/36$, corresponding to the order $n = 2$. The approximation of the magnetization given by Eq. (4.15) is in better agreement with the numerical simulations. In particular for the position of the resonances, Eq. (4.15) gives $p_r = \sqrt{\Delta p^2 - c}$, which is closer to numerical values as shown Fig. 4.7 (dashed line). However, this additional term does not balance the analogous contributions associated with higher orders ($n > 2$) for which a slightly different value of c is required. Deviations are however reasonably small (less than 10 %) over the range of inspected coefficients. The above argument can be extended to the case where $\Delta\theta < \pi$, so accounting for the terms proportional to M_0: In practice, an additional term of the type $c_1 M_0$ is introduced in the square roots of Eq. (4.15) where c_1 is a constant.

4.2.2 Low-energy limit

We now consider the low-energy limit $U \simeq (1 - M_0^2)/2$, that is $\Delta p \ll 1$. We notice that this limit is close to the line which marks the forbidden region in the parameter space (M_0, U) (see Fig. 3.7). In what follows, we find an approximation of the coefficients of $M(t)$ proportional to Δp^0. We first observe that the Liouville operator (4.7) either increases or decreases by one order the exponent of p. Thus, the odd powers $\mathcal{H}^k M$ contain a set of elements $b_{n,m}$ with m odd. For the water-bag initial distribution, such terms vanish, so $M(t)$ is an even function. Then, the recursion relation (4.10) is generated by $\mathcal{H}^2$. In the low-energy limit, if the kinetic terms are neglected, we get

$$\mathcal{H}^2 b_{u,0} \approx \frac{u}{2} \left(b_{1,0} b_{u-1,0} - b_{-1,0} b_{u+1,0} \right) . \tag{4.16}$$

An algebraic expression of the magnetization in the low energy limit is obtained by studying the sequence of terms at the lowest order. In this way, we approximate M as

$$M(t) \approx \sum_{n=0}^{\infty} \left(\alpha_n b_{1,0} + \beta_n b_{-1,0} b_{2,0} + \gamma_n b_{-1,0} b_{1,0}^2\right) \frac{t^{2n}}{2n!}. \tag{4.17}$$

Using Eq. (4.16), we deduce that, at a given order $n+1$, the $b_{1,0}$ term comes from the $b_{1,0}$ term at order n, with $\alpha_{n+1} = \alpha_n/2$. From this recursion relation, we deduce the formula

$$\alpha_n = \frac{1}{2^n}. \tag{4.18}$$

The $b_{-1,0}b_{2,0}$ term at the order $n+1$ is generated from both the $b_{1,0}$ and the $b_{-1,0}b_{2,0}$ terms at the lower order n. The recursion relation becomes $\beta_{n+1} = (\beta_n - \alpha_n)/2$, which leads to

$$\beta_n = -\frac{n}{2^n}. \tag{4.19}$$

The third term in $b_{-1,0}b_{1,0}^2$ is not only generated through the reduced operator given by Eq. (4.16), but also from other nonlinearities: The latter terms have been neglected in Eq. (4.16), but appear when considering $\mathcal{H}^4$ (and possibly higher powers of $\mathcal{H}$) in the low-energy limit. We resort to an *ansatz* for γ_{2n}, fitting the coefficients derived algebraically up to γ_{10}:

$$\gamma_n \approx -\frac{1}{9}\left(\frac{9}{2}\right)^n, \tag{4.20}$$

for large n. It follows that the magnetization in the low-energy regime is approximated by

$$\begin{aligned} M(t) \;\approx\; & M_0 \cosh\left(\frac{t}{\sqrt{2}}\right) - M_0 M_2(0) \frac{t}{2\sqrt{2}} \sinh\left(\frac{t}{\sqrt{2}}\right) \\ & - M_0^3 \frac{1}{9} \cosh\left(\sqrt{\frac{9}{2}} t\right). \end{aligned} \tag{4.21}$$

This expression of the magnetization is compared with numerical simulations in Fig. 4.8. We notice the good agreement up to the saturation regime. As expected, for longer times, the approximation gets worse due to higher order nonlinearities which have been neglected.

4.2.3 Out-of-equilibrium phase transition

As previously reported, increasing the energy U at a fixed value of the initial magnetization M_0 leads to a drastic change in phase space which materializes as an out-of-equilibrium phase transition [25] from an inhomogeneous to a homogeneous phase. This phenomenon has been faced in the previous chapter by invoking a principle of entropy maximization (Lynden-Bell theory [9]).

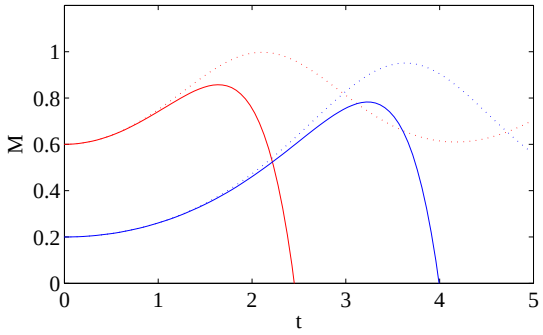

Figure 4.8: The magnetization $M(t)$ is plotted versus time, in the low-energy regime ($U = 0.01$), for $M_0 = 0.2$ (blue curves) and 0.6 (red curves). The solid lines refer to Eq. (4.21), the dotted ones to simulations (the numerical experiment's details are the same as those specified in Fig. 4.1).

Another dynamical explanation of such transition comes from a bifurcation analysis in phase space [71].

We here show that the transition can be also retrieved when tracking the short-time behavior of the magnetization. It means that the system relaxes very quickly in its metastable phase. The idea goes as follows: We monitor the magnetization dynamics via the analytical expression obtained from Eq. (4.10) and store the first local maximum, for each choice of the pair (M_0, U). In case the series diverges, without passing through a local maximum, the intensity is recorded when its derivative crosses a given threshold (as a polynomial, it eventually explodes). We choose $k_0 = 20$ in the algebraic computations. The resulting values of the magnetizations are displayed in Fig. 4.9 adopting a color code which continuously interpolates between the large ($M \approx 1$) and small ($M \approx 0$) magnetization. As clearly shown, the upper portion of the parameter plane corresponds to almost homogeneous configurations while magnetized phases are observed as the energy is reduced for fixed M_0. This scenario qualitatively agrees with direct numerical integrations, as confirmed by inspection of Fig. 4.10. In the N-body simulations, the available parameter space (M_0, U) is partitioned in small cells, each associated with a reference water-bag distribution (that is, a two-level distribution). The QSS magnetization is measured by averaging the numerical time series over a finite time window after relaxation. The average QSS magnetization is then represented using the same color code as above. When comparing Figures 4.9 and 4.10 it should be emphasized that the QSS regime occurs significantly after the violent relaxation process, beyond the first local maximum of the magnetization which is computed here. The results show that the average magnetization as recorded in the QSS corresponds approximately to these local maxima in the non-homogeneous phase. A better quantitative matching can be obtained by considering higher order terms (larger k_0). Even though, improving the accu-

racy of the theoretical analysis is a crucial requirement, already at this level of approximation it emerges a phase transition as clearly shown in Fig. 4.9. The difference between first and second order transitions is not clearly evidenced in the figure. However, in correspondence of the region that we know from Lynden-Bell analysis to be deputed to a first oder transition, a sharper jump between dark red and dark blue colors is appreciated, when compared to the continuos degradation in chromatic tonality as displayed elsewhere. It can be thus hypothesized that the method here outlined is potentially able to detect the order of the transition.

As we already discussed in Chapter 3, a continuous line in parameter space (M_0, U) marking the transition between the magnetized and unmagnetized phases can be computed on the basis of Lynden-Bell procedure shown in Section 3.3. Notice that the Lynden-Bell scenario recalled here formally applies to the water-bag initial condition from which the fermionic principle is derived. Different energy functionals are at variance to be assumed when dealing with more complex initial conditions and there is no a priori guarantee that the maximum entropy strategy would perform equally well. Aiming at extracting a transition line from the viewpoint of the bracket calculation, one could impose a critical threshold M_c to the magnetization: First local maximum values of the magnetization larger than M_c are assumed to yield a magnetized QSS, while for magnetization below the reference value M_c the system evolves toward a homogeneous QSS. The (arbitrary) choice $M_c = 0.4$ leads to a transition line (dashed line in Fig. 4.10) which resembles qualitatively the Lynden-Bell line (solid line). Notice that magnetized patches are numerically seen to extend over the region of homogeneous QSS, so effectively deforming the transition boundary in a non trivial way. Interestingly, such islands are entrapped in the wiggles of the bracket transition profile.

In conclusion, the bracket method returns sensible information on the existence of an out-of-equilibrium transition, so resulting in a powerful tool for those generalized settings where the Lynden-Bell *ansatz* proves inadequate (as for instance, for Gaussian initial conditions) or, at least, cumbersome (e.g. multi-level initial distribution).

4.3 Conclusion

In this chapter we have focused on the HMF short time dynamics, which ultimately governs the QSS emergence. An analytical treatment is proposed which enables one to characterize the time evolution of key collective variables. The idea is to develop an algebraic technique based on the Lie-Poisson structure of the HMF dynamics. In doing so we are able to return an analytical prediction for the global magnetization as a function of time, a macroscopic parameter sensitive to the microscopic particles evolution. Two limiting cases are explicitly considered, respectively the high and low energy settings, and shown to

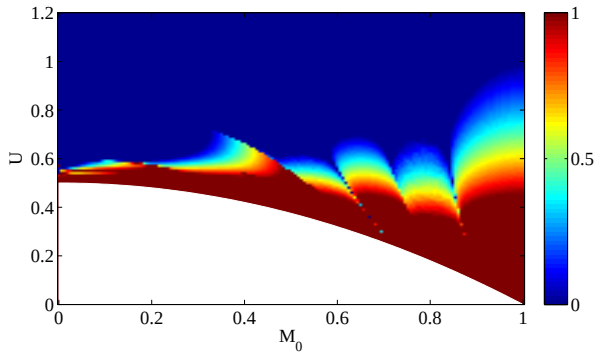

Figure 4.9: Map of the magnetization evaluated at the first local maximum of Eq. (4.10) in the (M_0, U) plan, see text for details. The data refer to the theoretical prediction calculated for $k_0 = 20$. The white region is the forbidden one.

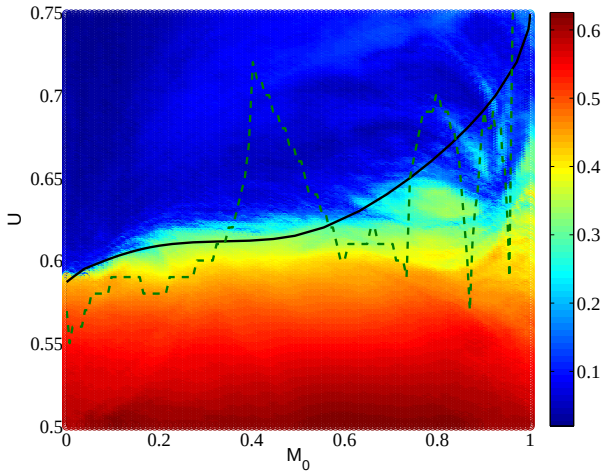

Figure 4.10: Map of the QSS magnetization in the (M_0, U) plan, as recorded via direct N-body simulations ($N = 10000$). The solid line refers to the Lynden-Bell prediction. The dashed line stands for the bracket transition line with threshold magnetization set to $M_c = 0.4$.

yield to tractable expressions for the magnetization amount. In general, and due to the perturbative nature of the calculation, the full analytic expression contains a vast collection of terms which are difficult to handle. The number of terms involved increases rapidly with the order of the approximation making it practically difficult to address the dynamics in the relevant, saturated, QSS regime. However, targeting the analysis to the first local maxima in the magnetization, and accounting for 20 orders in the perturbative expansion, the existence of an out-of-equilibrium phase transition was singled out, separating between homogeneous and non-homogeneous QSS. This transition was already analysed in Section 3.3 [25] and interpreted using an *ad hoc* maximum entropy principle suited for water-bag initial profiles. Although on calculations are carried out for the so-called water-bag initial condition, the technique here adopted is rather flexible and can be readily extended to other, possibly more general classes of initial conditions, so returning fully predictive scenarios. We also notice that the proposed method can be adapted to other contexts where long-range many body interactions are at play. The method is particularly adapted to short-time dynamics (transients, metastable states, violent relaxation, etc...).

Chapter 5

Introducing dilution in the Hamiltonian Mean Field model

In this chapter we will continue elaborating on the effects of dilution, this time examining the case of the HMF model. We shall be in particular interested in elucidating the out-of-equilibrium dynamics, focusing on the Quasi Stationary States. This is at variance with the discussion developed in Chapter 2, where we instead addressed the equilibrium feature for the Ising model.

To this end, we will first present a straightforward calculation for the equilibrium diluted HMF dynamics, the analysis closely resembling that of Chapter 2. Extending the results obtained for the Ising case study, we will here show that, in the thermodynamic limit, the diluted HMF model behaves, at equilibrium, as its fully connected analogue, independently on the degree of dilution.

We will then turn to discussing the results of a dedicated campaign simulations which enabled us to demonstrate the robusteness of QSS versus the dilution effects. We shall in particular quantify the QSS duration versus the number of simulated rotors and shed light onto the role played in this respect by the dilution amount γ. Within this novel scenario we will also generalize the concept of phase transition as described in Chapter 3 and quickly comment on the phase space topology as revealed by a Poincaré sections like analysis.

5.1 On the equilibrium solution of the diluted HMF

Adotping the same strategy as in Chapter 2, we will here introduce the dilution parameter γ which controls the average number of links N_L assigned at each selected node. Assume N to label the total number of particles (sites), then

N_L reads

$$N_L = N^\gamma/\gamma! \ . \tag{5.1}$$

The HMF Hamiltonian, in presence of dilution can be cast in the form

$$H = \frac{1}{2}\sum_{i=1}^{N} p_i^2 + \frac{N}{4N_L}\sum_{\langle i\neq k\rangle}^{N} J_{ik}\Big[1-\cos(\theta_i-\theta_k)\Big]. \tag{5.2}$$

where J_{ik} stands for the coupling strength, that might in principle depend on the selected pairs (i,k). We start by considering the equilibrium properties of such a system and so write the canonical partition function as:

$$Z = \sum_{S_i}\exp\left(-\beta H\right) = \sum_{S_i}\exp\Big[-\beta/2\sum_{i=1}^{N} p_i^2 - \frac{\beta N}{4N_L}\sum_{\langle i\neq k\rangle} J_{ik}\big(1-\cos(\theta_i-\theta_k)\big)\Big] \tag{5.3}$$

where θ_i represents the spin orientation angle. The constants J_{ik} are assumed to be distributed as

$$J_{ik} = \begin{cases} 1 & \text{with probability } p = \frac{2}{\gamma!}N^{\gamma-2} \\ 0 & \text{with probability } 1-p = 1-\frac{2}{\gamma!}N^{\gamma-2}. \end{cases} \tag{5.4}$$

The probability distribution is thus written as

$$P(J_{ik}) = p_1\delta(J_{ik}-1) + (1-p_1)\delta(J_{ik}), \tag{5.5}$$

which is completely equivalent to that employed when dealing with for the Ising model (2.5), with $J=1$. We shall hereafter concentrate on the thermodynamic limit ($N\to\infty$) and prove again that the diluted system always converges to the corresponding fully coupled for $1<\gamma\leq 2$.

To persecute this objective, we compute the averaged logarithm of partition function $\langle \ln Z\rangle_J$, where, as already mentioned, $\langle\cdot\rangle_J$ denotes the average over the disorder. More precisely we shall again make use of the replica trick approximation as defined in (2.6). The HMF replicated partition function reads:

$$\begin{aligned} Z^n &= \Big[\sum_{\{S_i\}} e^{-\beta H(S_i)}\Big]^n = \qquad (5.6)\\ &= \sum_{\{S_i^a\}}\exp\Big[-\frac{\beta}{2}\sum_a\sum_{i=1}^{N}(p_i^a)^2 - \frac{\beta N}{4N_L}\sum_a\sum_{\langle i\neq k\rangle}\big(1-\cos(\theta_i^a-\theta_k^a)\big)\Big] = \\ &= \sum_{\{S_i^a\}}\exp\Big[-\frac{\beta}{2}\sum_{i=1}^{N}\sum_a(p_i^a)^2 - \frac{\beta N}{4N_L}\sum_{\langle i\neq k\rangle}\sum_a\big(1-\cos(\theta_i^a-\theta_k^a)\big)\Big] \end{aligned}$$

where the index a runs over the n replicas.

Averaging over disorder eventually yields to:

$$\begin{aligned}\langle Z^n\rangle_J &= \sum_{\{S_i^a\}} \exp\Big[-\frac{\beta}{2}\sum_a\sum_{i=1}^N (p_i^a)^2\Big]\times \\ &\times \sum_{J_{ij}} P(J_{ij}) \exp\Big[\frac{\beta N}{4N_L}\sum_a\sum_{\langle i\neq k\rangle}\big(1-\cos(\theta_i^a-\theta_k^a)\big)\Big] = \\ &= \sum_{\{S_i^a\}} \exp\Big[-\frac{\beta}{2}\sum_a\sum_{i=1}^N (p_i^a)^2\Big]\times \\ &\times \sum_{J_{ij}} P(J_{ij}) \prod_{i\neq j}\exp\Big[\frac{\beta N}{4N_L}\sum_a\big(1-\cos(\theta_i^a-\theta_k^a)\big)\Big]\end{aligned} \tag{5.7}$$

Recalling Eq. (5.5) one then obtains:

$$\begin{aligned}\langle Z^n\rangle_J &= \sum_{\{S_i^a\}} \exp\Big[-\frac{\beta}{2}\sum_a\sum_{i=1}^N (p_i^a)^2\Big]\times \\ &\times \prod_{i\neq j}\Big[1-\frac{2}{\gamma!}\frac{1}{N^{2-\gamma}}+\frac{2}{\gamma!}\frac{1}{N^{2-\gamma}}\exp\Big[\frac{\beta N\gamma!}{4N^{\gamma-1}}\sum_a\Big(1-\cos(\theta_i^a-\theta_k^a)\Big)\Big]\Big] = \\ &= \sum_{\{S_i^a\}} \exp\Big[-\frac{\beta}{2}\sum_a\sum_{i=1}^N (p_i^a)^2\Big]\times \\ &\times \exp\Big[\sum_{i\neq j}\ln\Big[1-\frac{2}{\gamma!}\frac{1}{N^{2-\gamma}}+\frac{2}{\gamma!}\frac{1}{N^{2-\gamma}}\exp\Big[\frac{\beta N\gamma!}{4N^{\gamma-1}}\sum_a\Big(1-\cos(\theta_i^a-\theta_k^a)\Big)\Big]\Big]\Big].\end{aligned} \tag{5.8}$$

To proceed further we expand the exponential function and the logarithmic function and retain the leading order in N

$$\langle Z^n\rangle_J = \sum_{\{S_i^a\}} \exp\Big[-\frac{\beta}{2}\sum_a\sum_{i=1}^N (p_i^a)^2\Big]\exp\Big[\sum_{i\neq j}\sum_a\frac{-\beta}{2N}(1-\cos(\theta_i^a-\theta_k^a)\Big] = Z_\infty^n. \tag{5.9}$$

So $\langle \ln Z\rangle_J = \ln Z_\infty$ and the corresponding Hamiltonian:

$$H_\infty = \sum_j \frac{p_j^2}{2} + \sum_{j\neq k}\frac{1}{2N}(1-\cos(\theta_i-\theta_k)). \tag{5.10}$$

In conclusion, and as anticipated, for large enough N values and for $1 < \gamma \leq 2$ the diluted system is equivalent to Eq.(3.1). In other words, and irrespectively from the dilution amount, system (5.2) is expected to relax asymptotically to the equilibrium configuration, which is eventually attained by the original, fully coupled analogue.

5.2 On Quasi Stationary States in presence of dilution

We will here focus on investigating the emergence of Quasi Stationary States for a HMF model on a diluted network. We shall be in particular concerned with testing the robustness of QSS versus the dilution amount. Are the QSS still present when the average number of link per node is progressively reduced? And, in that case, how the duration time scales with the dilution parameter γ? These are the questions that we plan to address in the following.

Let us start by clarifying the numerical procedure that will be employed in the forthcoming characterization. The equation of motion of the diluted HMF model can be readily obtained and read:

$$\begin{aligned} \dot{\theta}_i &= \frac{\partial H}{\partial p_i} = p_i \\ \dot{p}_i &= -\frac{\partial H}{\partial \theta_i} = -\frac{1}{2N_L}\big(\sin\theta_i \sum_{j\in N_L} \cos\theta_j - \cos\theta_i \sum_{j\in N_L} \sin\theta_j\big) \end{aligned} \tag{5.11}$$

Our numerical implementation relies on a symplectic 4th-order integrator, the so called McLaghan-Atela algorithm [67]. The timestep here selected is $dt = 0.5$.

As for the Ising case, the disorder is of the *quenched* type: The configuration of assigned links is fixed for every realization, without being further adjusted during the simulations. The quantities of interest are averaged over several configurations of the underlying network of contacts.

To keep contact with the preceding discussion, we will limit our analysis to the water-bag initial condition specified by Eq. (3.17). We recall again that, for this specific case the initial magnetization and the energy read respectively (in the large N limit):

$$\begin{aligned} M_0 &= \frac{\sin(\triangle\theta)}{\triangle\theta} \\ U &= \frac{\triangle p^2}{6} - \frac{M_0^2 - 1}{2}. \end{aligned} \tag{5.12}$$

the initial condition being therefore completely characterized by the above two quantities. We begin our discussion by presenting the results relative to an initially homogeneous distribution ($M_0 = 0$). We focus on two different choices of the energy, $U = 0.58$ and $U = 0.69$, respectively below and above the transition line point $U_c = 7/12$.

Consider first the case $U = 0.69$ which in the fully connected scenario ($\gamma = 2$) is shown to yield to an almost demagnetized QSS. In Figure 5.1 we report on the temporal evolutions of the magnetization as recorded in our numerical simulations, for different values of the dilution, and by varying the system size (three choices of N in each panel, respectively $N = 500$, 1000, 2000).

Several observations can be made, as it follows a straightfoward qualitative inspection of the figures. On the one hand the QSSs do exist even in presence of dilution. The magnetization settles down into an intermediate, characteristic *plateau* which is eventually maintained for long times (notice the logarithmic scale on the x-asis), displaying a sensible dependence on the number N of simulated particles, as we shall be commenting in the following. On the other hand, the value of the magnetization associated to the QSS regime of Fig. 5.1 is shown to decrease when increasing the system size. We hence argue that the QSS is of the homogeneous type, as it is indeed found for the fully connected reference case for the same choice of paramters ($U > U_c$). As a final comment, we also stress that the asymptotic value of the magnetization is independent on the specific choice of the dilution and compatible, within statistical fluctuations due to the finite number of realizations, with the equilibrium value calculated for the fully connected case ($M_{eq} \sim 0.3$, solid lines in the figures). This finding confirms in turn the adequacy of the theoretical argument developed in Section 5.1.

In Fig. 5.2 we re-order the simulation outputs so to appreciate how the dilution γ affects the QSS lifetime. The more the system is connected the longer the QSS survives. We emphasize that, as the dilution takes the lowest value here considered (namely $\gamma = 1.5$), the QSS lifetime gets reduced by two orders of magnitude, with respect to the corresponding fully connected case. While QSS are certainly present when dilution is accounted for, they tend to progressively reduce their duration as γ approaches the limiting value 1, where they formally fade off.

In order to quantify our observation we turn to measuring the QSS lifetime τ_{QSS} via the very same fitting procedure as introduced in Section 3.4. We here recall that the sigmoid profile (3.19) can be numerically superposed to the simulated curves, by properly tuning the free parameters $a(N)$,$b(N)$,$c(N)$ and $d(N)$. In particular, τ_{QSS} is estimated as $10^{b(N)}$. Result of the analysis are displayed in Fig. 5.3, where τ_{QSS} is plotted as a function of N in log-log scale, for different choices of γ (symbols). The data follow a power-law trend, the exponent (slope of the linear profiles) being sensitive to the selected γ.

Starting from this observation, it would be extremly interesting to elaborate on a reasonble *ansatz*, physically motivated, which is capable of reproducing the scaling observed for $\gamma < 2$, while converging to the well-known $N^{1.7}$ solution as the $\gamma \to 2$ limit is performed. We stress again that the 1.7 factor is being suggested to apply when homogeneous QSS are concerned, but our simulations as reported in Section 3.4 seem equally compatible with the more sound 1.5 choice. We introduce again α to label such a controversial exponent, regardless of its specific numerical value. A rather natural proposal would be to replace in the aforementioned relation the global number of degree of freedom N, with the effective quantity $N_{eff} = N^{(\gamma-1)}$ which quantifies the average number of links per node. Under this assumption:

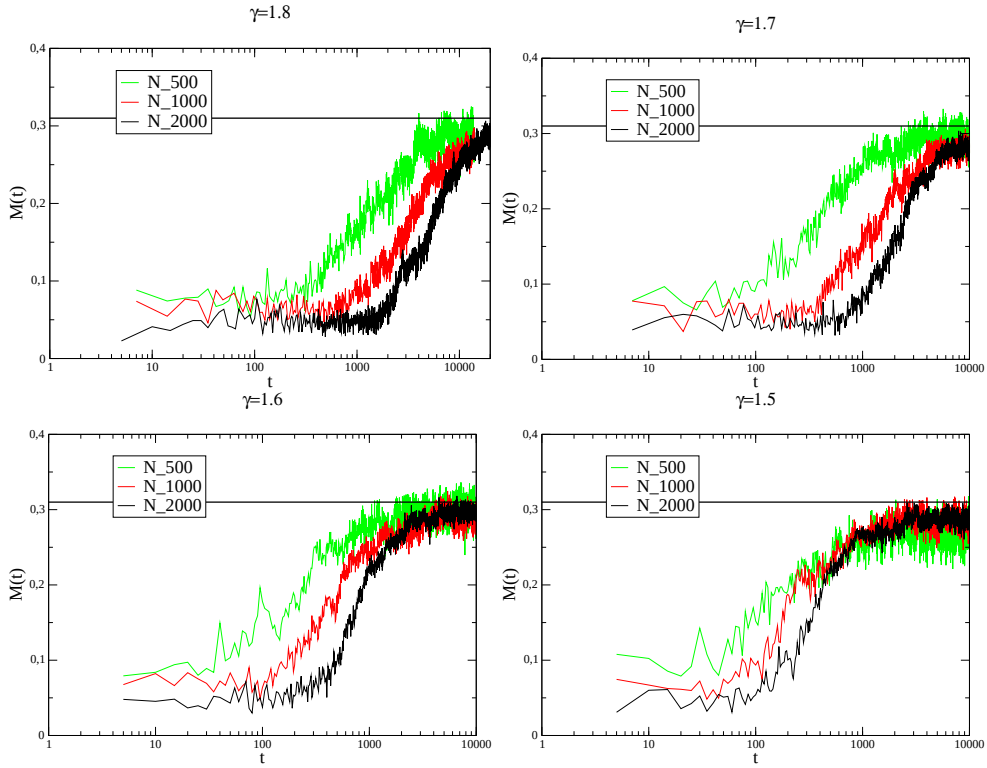

Figure 5.1: Temporal evolution of the magnetization $M(t)$ for different particle numbers N: 500 (green), 1000 (red), 2000 (black). Different panels refer to distinct choices of γ. Moving clockwise from the top/left panel, $\gamma = 1.8, 1.7, 1.6, 1.5$. Solid lines represent the equilibrium value $M \simeq 0.3$. The energy of the system is always set to $U = 0.69$, and $M_0 = 0$

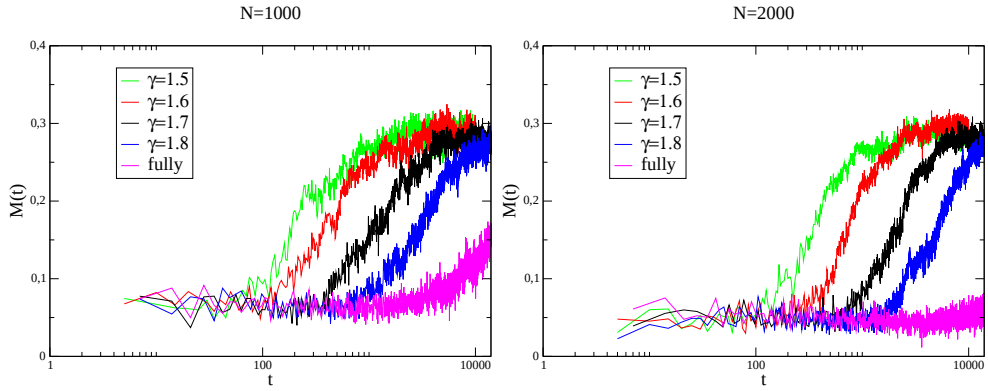

Figure 5.2: Temporal evolution of the magnetization $M(t)$ for different values of γ and for $N = 1000$ (on the left) and $N = 2000$ (on the right). The energy of the system is $U = 0.69$.

$$\tau_{QSS} \propto N_{eff}^{\alpha} = N^{\alpha(\gamma-1)} \tag{5.13}$$

which reduces to the correct functional dependence when γ is set to 2. Also, working at fixed N, *ansatz* (5.13) predicts that the QSS lifetime would shrink as $\gamma \to 1$, in agreement with our numerical experiments. In Fig. 5.3 symbols referring to the simulation are compared to the proposed scaling law (5.13), for both $\alpha = 1.7$ (black solid lines) and $\alpha = 1.5$ (red solid lines). A convincing degree of correspondence can be clearly appreciated, so pointing to the correctness of the proposed scenario. Even more interestingly, our numerical data seem to be better interpolated by the $\alpha = 1.5$ choice, this latter possibly arising in the context of a standard kinetic theory treatment, see Section 3.4.

Before proceeding with our discussion a further comment is mandatory. We emphasize in fact that, up to this point, we are solely dealing with homogeneous QSS, the selected energy amount being so far set above the out-of-equilibrium transition line. Though the analysis is developed with reference to $M_0 = 0$, the conclusions reached hold more generally and admit a natural extension to initially bunched ($M_0 \neq 0$) water-bag, provided $U > U_c$. The dual condition $U < U_c$ is addressed in the remaining part of this section, where $U = 0.58$ for $M_0 = 0$.

Consider the upper panel of Fig. (5.4) and (5.5), where the temporal

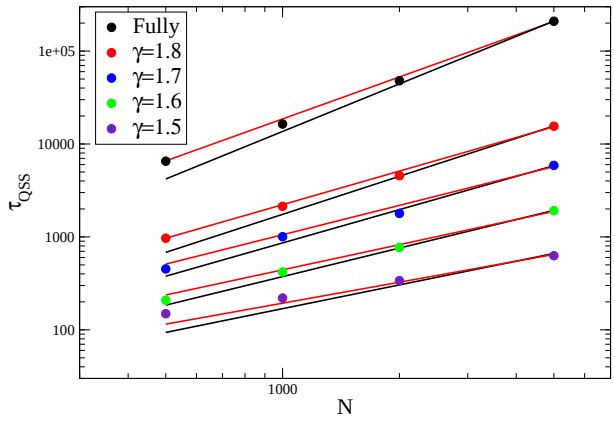

Figure 5.3: τ_{QSS} is plotted versus N. Symbols refer to direct simulation, where the time duration of the QSS is estimated by resorting to the fitting procedure (3.19), as discussed in the text. Averages over several realizations are considered. The solid lines stand for *ansatz* (5.13) where α is alternatively set to 1.7 (black) and 1.5 (red).

evolution of the magnetization is plotted, for $\gamma = 1.7$ and $\gamma = 1.8$ respectively. Visually, the evolution shares many similarities with the corresponding fully coupled scenario: Indeed the system sets down into an intermediate QSS which is now magnetized. Then the system drifts towards the thermodynamic

equilibrium, to which the solid horizontal line refers to. Expanding on the preceding argument and recalling that for magnetized QSS a linear scaling with N is expected to apply, we are inclined to believe:

$$\tau_{QSS} \propto N_{eff} = N^{(\gamma-1)} \tag{5.14}$$

To assess the adequacy of such an *ansatz* we now plot the time series collected in our numerical esperiments, as a function of the rescaled time $t/N^{\gamma-1}$, see lower panel of Fig. (5.4) and (5.5). The curves nicely collapse onto each other, so validating the scenario of Eq. (5.14). Also in this case, such conclusions are shown to apply also for the more general setting where initial bunched water-bag are selected.

In conclusion we have here proven that QSSs do exist in diluted HMF dynamics. Their lifetime diverges with the system size, following however a different scaling depending on the specificity of the selected initial condition. The effect of the dilution translates into a modification of the scaling exponent, which is correctly guessed on the basis of an intuitive *ansatz*.

5.3 Phase transition

In the preceding discussion we have concluded that the high energy (non-magnetized) state and the low-energy (magnetized) state preserve their identity, when the dilution is accommodated for. What can we say about the phase transition separating this two regimes? While it is evident that a transition still occurs, can one elaborate on the specific role of γ? Is it affecting the critical value of the energy at which the transition takes place for a given M_0 amount? And what about the order of the transition? We shall here provide a preliminary answer to these questions for the specific case $M_0 = 0$, which, we recall, yields to a first order out-of-equilibrium phase transition, as evidenced by the Lynden-Bell variational problem [25].

In Fig. 5.6 (left panel) the temporal evolution of the magnetization is reported for $\gamma = 1.7$. Different curves refer to distinct U, scanning the interval from 0.58 to 0.62. The corresponding transition is represented in right panel of Fig. 5.6. The transition seem to occur for an energy value larger than 7/12, i.e. the fully coupled reference value. Additional simulations are however necessary to shed light onto this issue, clarifying the role of finite N corrections, particularly crucial for diluted graphs. It can be moreover argued that the dilution mechanism mutates first order into second order transitions.

As a final point, we also enclose a plot of single-particle stroboscopic trajectories in the magnetized QSS (see Fig 4.5 upper panel). In Fig. 5.7 the

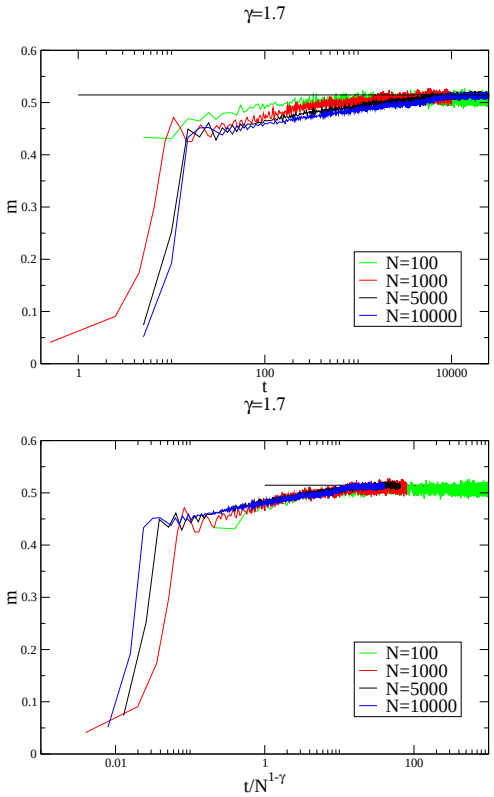

Figure 5.4: In the upper panel the temporal evolution of the magnetization is plotted for $\gamma = 1.7$ and $U = 0.58$. Different colors refer to different system sizes: green is $N = 100(100)$, red is $N = 1000(10)$, black is $5000(8)$, blue is $10000(4)$. The number between brackets corrisponds to the number of samples. In the lower panel the same curves are plotted versus the rescaled time $t/N^{\gamma-1}$. Solid lines represent the equilibrium value $M \simeq 0.5$.

dilution is set to $\gamma = 1.95$ and the number of simulated particles is $N = 5000$. Fig. 5.8 is instead relative to $\gamma = 2$ and is obtained by employing an identical number of simulated particles. It is evident that the tori tickness is more pronounced in the former case when compared to the latter, so favouring mixing and equilibration. This observation agrees hence with the finding that diluted QSS last for shorter times as opposed to their fully coupled homologue.

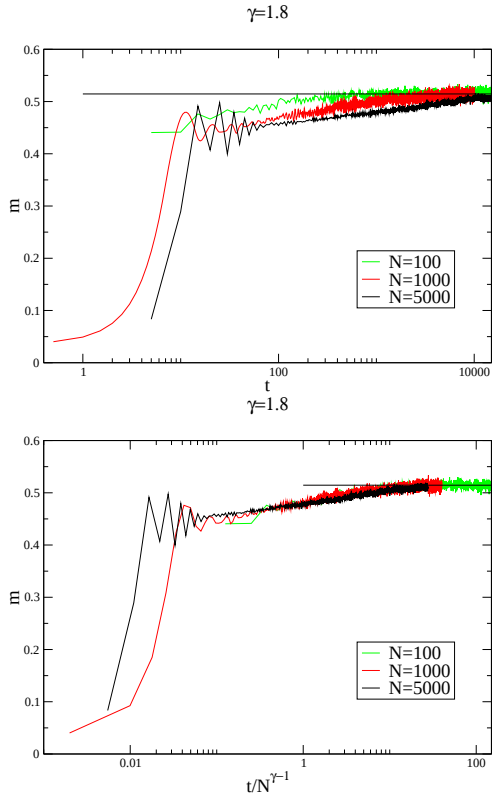

Figure 5.5: The temporal evolution of the magnetization is plotted for $\gamma = 1.8$ and $U = 0.58$. Different colors refer to different system sizes: green is $N = 100(100)$, red is $N = 1000(10)$, black is $5000(8)$. The number between brackets corrisponds to the number of samples. In the lower panel the same curves are plotted versus the rescaled time $t/N^{\gamma-1}$. Solid lines represent the equilibrium value $M \simeq 0.5$.

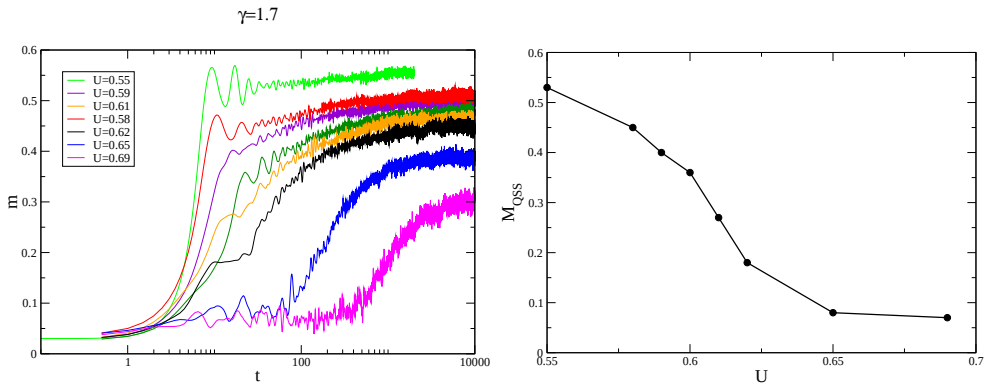

Figure 5.6: In the left panel the temporal evolution of the magnetization is represented for $N = 1000$, $\gamma = 1.7$ and different energy values. Every curve is averaged over 10 realizations of the system. In the right panel the magnetization in the QSSs (M_{QSS}) is displayed versus the energy amount.

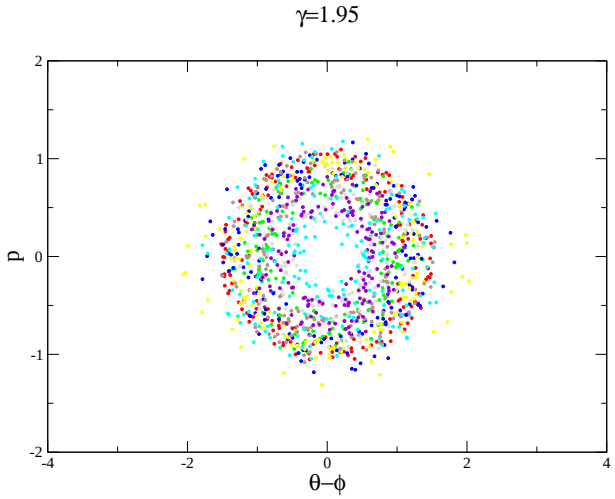

Figure 5.7: Poincaré sections of a few selected particles relative to $N = 5000$ in the QSS regime for water-bag initial conditions : $(M_0, U) = (0.7, 0.5)$. γ is set to 1.95.

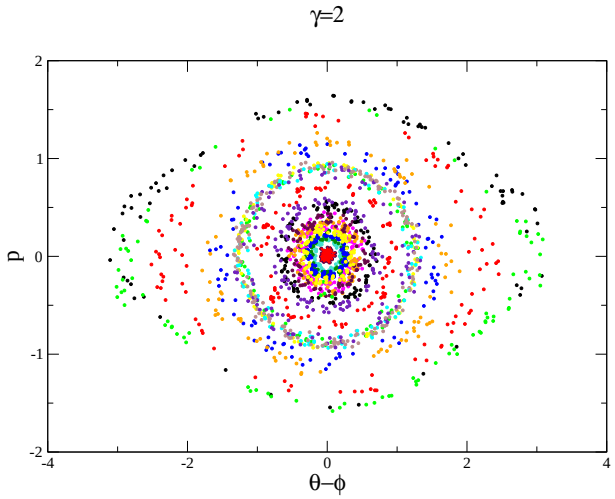

Figure 5.8: Poincaré sections of a few selected particles relative to $N = 5000$ in the QSS regime for water-bag initial conditions : $(M_0, U) = (0.7, 0.5)$. γ is set to 2.

Conclusions

In this thesis work we have focused on long-range interacting systems, being particularly concerned with the special class of mean-field models.

One of the issues that we have here addressed relates to the effect of diluting the networks of contacts between microscopic actors. The Ising model was first analyzed and the associated equilibrium properties discussed versus the dilution amount. In the thermodynamic limit the system is shown to be equivalent to its corresponding, fully connected analogue, i.e. the so called Curie-Weiss model. A prominent role is however played by finite size corrections, which substantially affect the equilibrium solution, the deviations becoming more pronounced as the dilution is enhanced. The problem is here analytically tackled by resorting to a replica based perturbative calculation. In parallel the cavity method is also employed, so adapting to the case under inspection a procedure pionereed by Mézard and Parisi in [43]. To validate our predictions direct numerical simulations are also performed, which unambigously resolve in favour of the cavity approximation when compared to the replica one. In conclusion, and with reference to the equilibrium behaviour of our Ising like model, the imposed dilution drastically alters the dynamics of the system, the corrections being sensible for relatively small populations of interacting spins. This result warns against an undiscriminate, non critical usage of straightforward (mean field type) calculations, a practice often invoked in biological and social modelling contexts. In other words, finite size corrections do play an important role and need to be carefully addressed.

Long range systems diplay also a rather peculiar out-of-equilibrium dynamics, that we have evoked all along this thesis. We have in particular directed our attention on the emergence of Quasi Stationary States (QSSs) and investigated such a fascinating topic with reference to the Hamiltonian Mean Field (HMF) model. Motivated by the necessity to reconcile apparently contradicting empirical observations, we here conjecture that two different scaling for the lifetime of the QSSs versus the simulated number of particles exist, depending

on the initial parameters setting. Our numerics suggest that homogeneous QSSs last for a time diverging as a super-linear fractional power of the system size. Conversely, when magnetized QSS are to be expected, a linear divergence with N is detected. This scenario seems plausible in the light of a simple kinetic theory argument.

To provide a dynamical interpretation on the QSS and eventually shed light onto the associated phase transition, originally understood in the framework of the statistical theory of violent relaxation, we have then developed the so called Bracket Method. This is an analytical scheme, particularly suitable for short time investigations, that exploits the Hamiltonian formalism of the relavant (continuous) Vlasov picture, which ultimately governs the QSS phenomenon. The time evolution of the magnetization is predicted and shown to correlate with the results of direct numerical experiments. Two limiting cases are explicitly addressed, respectively the high and low energy settings, and shown to yield to tractable, closed expressions for the magnetization amount. Altough approximately, due to the inherent difficulties to handle the vast collection of terms that the full analytic expression contains, the aforementioned out-of-equilibrium phase transition is singled out, separating between homogeneous and non-homogeneous QSS. Even if calculations are carried out for the so-called water-bag scenario, the proposed technique is rather flexible and can be readily extended to other, possibly more general classes of initial conditions. We also notice that the proposed method can be adapted to other contexts where long-range many-body interactions are at play.

Finally, and to build an ideal bridge with our earlier investigations, we turned to quantify the effect of an induced dilution in the HMF out-of-equilibrium dynamics. To quote our main conclusion, we assess that QSS are robust versus the dilution effect. Starting from an initial condition of the water-bag type the system rapidly falls towards an intermediate, long lasting regime which bears the distinctive features of the paradigmatic QSS. The more the network of couplings is connected, the longer the QSS survives, at fixed N amount, before the system relaxes to equilibrium. In other words the dilution does quantitatively alter the QSS lifetime. In this respect, we have guessed a physically sound *ansatz* which is able to reproduce with a satisfying degree of accuracy the dependence of the lifetime of diluted QSS versus N. A phase transition is also found in presence of an effective dilution, which seems to induce a smoothing of the transition line.

List of Publications

1. J. Barré, A. Ciani, D. Fanelli, F. Bagnoli and S. Ruffo, *Finite Size Effects for the Ising Model on Random Graphs with Varying Dilution*, Physica A **388**, 3414-3425, 2009, `arXiv:0902.0564`

2. R. Bachelard, C. Chandre, A. Ciani, D. Fanelli and Y. Yamaguchi, *Analytical results on the magnetization of the Hamiltonian Mean Field model*, submitted to Physica A (2009), `arXiv:0903.3641`

Ringraziamenti

Bibliography

[1] P. H. Chavanis. *International Journal of Modern Physics B*, 20:3113, 2006.

[2] T. Padmanabhan. *Physics Reports*, 188:285, 1990.

[3] Y. Elskens and D.F. Escande. *Microscopic Dynamics of Plasmas and Chaos*. IoP Publishing, Bristol, 2003.

[4] J. Miller. *Phys. Rev. Lett.*, 65:2137, 1990.

[5] R. Robert. *Comptes Rendus de l'Académie des Sciences: Série I Maths*, 311:575, 1990.

[6] S. Slama, G. Krenz, S. Bux, C. Zimmermann, and P. W. Courteille. Scattering in a high-q ring cavity. In Campa et al. [27].

[7] Ph. Chomaz and F. Gulminelli. Phase transitions in finite systems. In Dauxois et al. [10].

[8] R. Albert and A. L. Barabàsi. *Rev. Mod. Phys.*, 74:47–97, 2002.

[9] D. Lynden-Bell. *Mon. Not. R. Astron. Soc.*, 136:101, 1967.

[10] T. Dauxois, S. Ruffo, E. Arimondo, and M. Wilkens, editors. *Dynamics and Thermodynamics of Systems with Long Range Interactions*, volume 602. Springer, 2002.

[11] M. Kac *et al. J. Math Phys.*, 4:216, 1963.

[12] A. Campa, T. Dauxois, and S. Ruffo. *Physics Report, in press*, 2009.

[13] M. Blume *et al. Phys. Rev. A*, 4:1071, 1971.

[14] J. Barré, D. Mukamel, and S. Ruffo. *Phys. Rev. Lett.*, 87:030601, 2001.

[15] D. Mukamel, S. Ruffo, and N. Schreiber. *Phys. Rev. Lett.*, 95:240604, 2005.

[16] M. Creutz. *Phys. Rev. Lett.*, 50:1411, 1983.

[17] Y. Y. Yamaguchi *et al. Physica A*, 337:36, 2004.

[18] R. Bonifacio *et al. Riv. Nuovo Cimento*, 13:1, 1969.

[19] R. Bonifacio and L. De Salvo. *Nucl. Instrum. Meth. Phys. Res. A*, 341:360, 1994.

[20] R. Bonifacio *et al. Phys. Rev. A*, 50:1716, 1994.

[21] A. Antoniazzi, D. Fanelli, P.H. Chavanis J. Barré, T. Dauxois, and S. Ruffo. *Phys. Rev. E*, 75:011112, 2007.

[22] A. Antoniazzi, Y. Elskens, D. Fanelli, and S. Ruffo. *Europ. Phys. J. B*, 50:603, 2006.

[23] A. Antoniazzi, D. Fanelli, J. Barré, P.H. Chavanis, T. Dauxois, and S. Ruffo. *Phys. Rev. E*, 75:011112, 2007.

[24] G. De Ninno, A. Antoniazzi, B. Diviacco, D. Fanelli, L. Giannessi, R. Meucci, and M. Trovó. *Phys. Rev. E*, 71:066504, 2005.

[25] A. Antoniazzi, D. Fanelli, S. Ruffo, and Y. Y. Yamaghuci. *Phys. Rev. Lett.*, 99:040601, 2007.

[26] G. Kaniadakis, M. Lissia, and A. Rapisarda, editors. *Proceedings of the International School and Workshop on Non Extensive Thermodynamics and Physica applications*, volume 305, Nos.1-2, 2002.

[27] A. Campa, A. Giansanti, G. Morigi, and F.S. Labini, editors. *Dynamics and Termodynamics of Systems with long range interactions: theory and experiments*, volume 970. AIP Conf. Proc., 2008.

[28] P.J.E. Peebles. *The Large-scale structure of the Universe*. Princeton University Press, Princeton, 1980.

[29] For a detailed review of the free electron lasers under development `http://sbfel3.ucsb.edu/www/vl_fel.html`.

[30] G. L. Eyink and K. R. Sreenivasan. *Rev. Mod. Phys.*, 78:87, 2006.

[31] L. De Sanctis and F. Guerra. *J. Stat. Phys.*, 132:759, 2008.

[32] A. Barra. *J. Stat. Phys.*, 132:787, 2008.

[33] F. Di Patti and D. Fanelli. arXiv:0812.1568, preprint 2008.

[34] E. Agliari, A. Barra, and F. Camboni. arXiv:08044503, preprint 2008.

[35] A. Dembo and A. Montanari. arXiv:08044726, preprint 2008.

[36] A. Bovier and V. Gayrard. *J. Stat. Phys.*, 72:643, 1993.

[37] P. Erdős and A. Renyi. *Publ. Math. Debrecen*, 6:290–297, 1959.

[38] N. Metropolis *et al. J. Chem Phys.*, 21:1087, 1953.

[39] K. Binder. *Z. Physik B*, 43:119, 1981.

[40] S. N. Dorogovtsev, A. V. Goltsev, and J. F. F. Mendes. *Rev. Mod. Phys*, 80:1275, 2008.

[41] S. N. Dorogovtsev, A. V. Goltsev, and J. F. F. Mendes. *Phys. Rev. E*, 66:016104, 2002.

[42] M. Leone, A. Vázquez, A. Vespignani, and R. Zecchina. *Eur. Phys. J. B*, 28:191, 2002.

[43] M. Mézard and G. Parisi. *Eur. Phys. J. B*, 20:217, 2001.

[44] M. Antoni and S. Ruffo. *Phys. Rev. E*, 52:2361, 1995.

[45] A. Campa, A. Giansanti, and D. Moroni. *Phys. Rev. E*, 62:303, 2000.

[46] M. Antoni, S. Ruffo, and A. Torcini. *Europhys. Lett.*, 66:645, 2004.

[47] T. Konishi and K. Kaneko. *J. Phys. A*, 25:6283, 1992.

[48] J. Barré. *Mécanique Statistique et Dynamique Hors Équilibre de Systémes avec Interaction á Longue Portée*. PhD thesis, 2003.

[49] A. Pluchino, V. Latora, and A. Rapisarda. *Phys. Rev. E*, 69:056113, 2004.

[50] M. Antoni and S. Ruffo. *Phys. Rev. E*, 52:2361, 1995.

[51] A. Antoniazzi. *Non-Equilibrium Dynamics of Mean-Field Models: the Emergence of Quasi-Stationary States*. PhD thesis, 2006.

[52] J. Barré, F. Bouchet, T. Dauxois, and S. Ruffo. *J. Stat. Phys.*, 119:677, 2005.

[53] J. Barré, T. Dauxois, G. De Ninno, D. Fanelli, and S. Ruffo. *Phys. Rev. E*, 69:045501, 2004.

[54] A. Pluchino, V. Latora, and A. Rapisarda. *Physica A*, 60:338, 2004.

[55] K. Jain, F. Bouchet, and D. Mukamel. *J. Stat. Mech.*, P11008, 2007.

[56] W. Braun and K. Hepp. *Comm. Math. Phys.*, 56:101, 1977.

[57] D.R. Nicholson. *Introduction to Plasma Physics*. Wiley, 1983.

[58] R. Balescu. *Phys. of Fluids*, 3:52, 1960.

[59] F. Bouchet and T. Dauxois. *Phys. Rev. E*, 72:045103(R), 2005.

[60] A. Antoniazzi, F. Califano, D. Fanelli, and S. Ruffo. *Phys. Rev. Lett.*, 98:150602, 2007.

[61] P. H. Chavanis, J. Sommeria, and R. Robert. *Astrophys. J.*, 471:385, 1996.

[62] P. H. Chavanis. *Physica A*, 359:177, 2006.

[63] F. Staniscia, P. H. Chavanis, G. De Ninno, and D. Fanelli.

[64] L. G. Moyano and C. Anteneodo. *Phys. Rev. E*, 74:021118, 2006.

[65] A. Pluchino and A. Rapisarda. Anomalous diffusion and quasistationarity in the HMF model. volume 965, pages 129–136. AIP Conf. Proc., 2007.

[66] A. Campa, A. Giansanti, and G. Morelli. *Phys. Rev. E*, 76:041117, 2007.

[67] R.I. Mc Lachlan and P. Atela. *Nonlinearity*, 5:541, 1992.

[68] A. Campa, T. Dauxois, D. Fanelli, and S. Ruffo. *Private Communication*, 2009.

[69] R. Abraham and J. E. Marsden. *Foundations of Mechanics*. Addison-Wesley.

[70] M. Tabor and Y. M. Treve, editors. *Poisson brackets for fluids and plasmas*, volume 88. AIP Conf. Proc., 1982.

[71] R. Bachelard, C. Chandre, D. Fanelli, X. Leoncini, and S. Ruffo. *Phys. Rev. Lett.*, 101:260603, 2008.